

A Study of the Decays of Neutral Kaons into $2\pi^0$ and $3\pi^0$ using the CPLEAR Detector at CERN

A dissertation submitted to the
SWISS FEDERAL INSTITUTE OF TECHNOLOGY ZÜRICH
for the degree of
DOCTOR OF NATURAL SCIENCES

presented by
MARCIN WOLTER
M.Sc.
born August 11, 1966
citizen of Poland

accepted on the recommendation of

Prof. Dr. H.-J. Gerber examiner
Prof. Dr. L. Tauscher co-examiner

1996

Contents

Abstract	1
Zusammenfassung	2
1 Introduction	3
2 Symmetries	5
2.1 Discrete Symmetries	5
2.2 Symmetries in Particle Physics	6
3 Phenomenology of the K^0 and \overline{K}^0 System	8
3.1 The Neutral Kaon System	8
3.1.1 Time Evolution of the $K^0 - \overline{K}^0$ System	8
3.1.2 Solution of the Schrödinger Equation	11
3.2 CP Violation in the $K^0 \rightarrow \pi\pi$ Decays	14
3.2.1 CP Parity of the Final States	15
3.2.2 Observable Parameters	15
3.2.3 Decay Rates and Asymmetry	18
3.3 CP Violation in the $K^0 \rightarrow \pi^0\pi^0\pi^0$ Decays	18
3.4 Models of CP Violation	21
3.4.1 Standard Model	21
3.4.2 Superweak Model	23
3.5 Interaction of Neutral Kaons with Matter	24
4 The CPLEAR Detector	26
4.1 Target, Beam Counter and Beam Monitor	28
4.2 Tracking Detectors	28
4.2.1 Proportional Chambers	29
4.2.2 Drift Chambers	29
4.2.3 Streamer Tubes	30
4.2.4 Tracking Performance	31
4.3 Particle Identification Detector	31
4.4 Electromagnetic Calorimeter	33
4.5 Trigger	36

4.6	Distribution of Material in the CPLEAR Detector	39
4.7	Data Processing	39
4.7.1	Data Acquisition	39
4.7.2	Data Reduction and Processing	42
5	Neutral Showers from Secondary Interactions	43
5.1	Analysis of the Fake Showers	43
5.1.1	Description of Fake Showers	44
5.1.2	Difference Between K^+ and K^- Events	49
5.1.3	Fake Shower Suppression	49
5.2	Comparison of Simulated and Real Fake Showers	50
5.3	Conclusions	51
6	Observation of CP Violation in $K^0 \rightarrow \pi^0\pi^0$ Decays	53
6.1	Selection of the $K^0 \rightarrow \pi^0\pi^0$ Events	53
6.1.1	Prefiltering	53
6.1.2	Selection	54
6.2	Reconstruction of the Neutral Kaon Lifetime	57
6.2.1	Vertex Reconstruction	57
6.2.2	Lifetime Resolution	61
6.3	Identification of Dalitz Decays and Photon Conversions	62
6.4	Backgrounds	63
6.4.1	Annihilation Backgrounds	65
6.4.2	Additional π^0 's Produced at the $p\bar{p}$ Annihilation Vertex	69
6.4.3	Fake Photon Background	69
6.4.4	K^0 Decays into Final States other than $\pi^0\pi^0$	72
6.5	Summary of Cuts	76
6.6	Neutral Kaon Lifetime	77
6.7	Determination of the CP Violation Parameter φ_{00}	79
6.7.1	Normalization	81
6.7.2	Lifetime Resolution and Backgrounds	81
6.7.3	Coherent Regeneration	82
6.7.4	Fit to the Measured Asymmetry	82
6.7.5	Systematic Errors	83
6.8	Conclusions	86
7	Search for CP Violation in $K^0 \rightarrow \pi^0\pi^0\pi^0 \rightarrow 6\gamma$ Decays	88
7.1	Event Selection and Reconstruction	88
7.1.1	Preselection	89
7.1.2	Complete Event Reconstruction	90
7.1.3	Reduction of Fake Showers	92
7.1.4	Lifetime and Missing Mass Distributions	96
7.2	Signal and Background Estimation	97

7.2.1	Fit to the Lifetime Distribution	97
7.2.2	Fit to the Missing Mass Distribution	101
7.3	Asymmetry	103
7.3.1	Fit Procedure	105
7.3.2	Results of the Asymmetry Fit	107
7.4	Systematic Errors	107
7.5	Conclusions	108
8	Conclusions	110
A	Dalitz Decays of the Neutral Pions	112
B	Photon Conversion	115
C	Theory of Fits with Constraints	117
D	Reconstruction of the e^+e^- Vertex	119
	Acknowledgments	122
	References	123
	List of Figures	130
	List of Tables	131
	Curriculum Vitae	132

Abstract

The CPLEAR experiment at CERN is designed to study CP violation in the neutral kaon system. The neutral kaons are produced in the $p\bar{p}$ annihilations at rest in the reactions:

$$\begin{aligned} p\bar{p} &\rightarrow K^-\pi^+K^0 \\ &\rightarrow K^+\pi^-\bar{K}^0 \end{aligned}$$

The strangeness of the produced neutral kaon is known from the charge of the accompanying kaon. The CP violation parameters are extracted from the asymmetries between the decay rates of initially pure K^0 and \bar{K}^0 into various final states.

In this work a study of CP violation in the neutral kaon decays into two and three neutral pions is presented. The neutral kaon decay vertex in the analysis of $K^0(\bar{K}^0) \rightarrow \pi^0\pi^0$ decays is reconstructed from the electron and positron originating from Dalitz decays of neutral pions ($\pi^0 \rightarrow e^+e^-\gamma$) or from a conversion, in the material of the detector, of photons from the π^0 decays. Using this method of lifetime reconstruction, the asymmetry is observed as a function of the neutral kaon lifetime. From this asymmetry the phase of the CP violation parameter η_{00} , is measured to be:

$$\varphi_{00} = 62^\circ \pm 11^\circ(stat) \pm 2^\circ(syst)$$

The search for CP violation in the $K^0(\bar{K}^0) \rightarrow \pi^0\pi^0\pi^0$ decays was stimulated by the moderate accuracy of the present existing upper limit of the CP violation parameter η_{000} . The neutral kaon lifetime is reconstructed using six photons from the decay chain $K^0(\bar{K}^0) \rightarrow \pi^0\pi^0\pi^0 \rightarrow 6\gamma$. Using a preliminary data sample of 1/4 of available events $\mathcal{I}m(\eta_{000})$ has been measured to be:

$$\mathcal{I}m(\eta_{000}) = 0.12 \pm 0.20 \text{ (stat)}$$

After processing all the available data, CPLEAR should reach a precision of $\Delta\mathcal{I}m(\eta_{000}) \approx 0.1$ and thus obtain an improved upper limit of $\mathcal{I}m(\eta_{000})$. This result will give a better limit on the direct CP violation in the $K^0(\bar{K}^0) \rightarrow \pi^0\pi^0\pi^0$ decays. It will also reduce the uncertainty of the present and future CPT tests comparing φ_{+-} with the superweak phase φ_{SW} .

Zusammenfassung

Das CPLEAR Experiment am CERN ist dem Studium der CP-Verletzung im System der neutralen Kaonen gewidmet. Die neutralen Kaonen werden dabei von in Ruhe stattfindenden $p\bar{p}$ Annihilationen erzeugt:

$$\begin{aligned} p\bar{p} &\rightarrow K^- \pi^+ K^0 \\ &\rightarrow K^+ \pi^- \bar{K}^0 \end{aligned}$$

Die Seltsamkeit eines erzeugten neutralen Kaons ist aus der Ladung des zweiten in der Annihilation entstandenen Kaons ersichtlich. Die Parameter der CP-Verletzung werden abgeleitet aus Asymmetrien zwischen den Raten der Zerfälle anfänglich reiner K^0 und \bar{K}^0 Zustände in verschiedene Endzustände.

In der vorliegenden Arbeit wird die CP-Verletzung in Zerfällen neutraler Kaonen in zwei und drei Pionen untersucht. Die Rekonstruktion des Zerfallsvertex $K^0(\bar{K}^0) \rightarrow \pi^0 \pi^0$ erfolgt über Elektron-Positron-Paare, die entweder von Dalitz-Zerfällen neutraler Pionen ($\pi^0 \rightarrow e^+ e^- \gamma$) oder von Konversionen der aus den Zerfällen der π^0 stammenden Photonen im Material des Detectors herrühren. Durch Anwendung dieser Methode zur Bestimmung der Zerfallszeiten kann eine Asymmetrie als Funktion der Eigenzeit der neutralen Kaonen beobachtet werden. Der aus dieser Asymmetrie gewonnene Meßwert für die Phase des CP-Verletzungsparameters η_{00} beträgt:

$$\varphi_{00} = 62^\circ \pm 11^\circ(stat) \pm 2^\circ(syst)$$

Das Ziel der Suche nach CP-Verletzung in Zerfällen $K^0(\bar{K}^0) \rightarrow \pi^0 \pi^0 \pi^0$ ist eine Verbesserung der gegenwärtig bescheidenen Genauigkeit der Obergrenze für den CP-Verletzungsparameter η_{000} . Die Zerfallszeit der neutralen Kaonen wird anhand der sechs Photonen in der Zerfallskette $K^0(\bar{K}^0) \rightarrow \pi^0 \pi^0 \pi^0 \rightarrow 6\gamma$ rekonstruiert. Die Analyse eines vorläufigen Datensatzes, der rund ein Viertel aller aufgezeichneten Ereignisse umfaßt, ergibt folgendes Resultat für $\mathcal{I}m(\eta_{000})$:

$$\mathcal{I}m(\eta_{000}) = 0.12 \pm 0.20 (stat)$$

Nach Verarbeitung aller verfügbaren Daten sollte CPLEAR eine Genauigkeit von $\Delta\mathcal{I}m(\eta_{000}) \approx 0.1$ erreichen und somit eine neue verbesserte Obergrenze für $\mathcal{I}m(\eta_{000})$ erhalten. Dieses Resultat wird eine verbesserte Obergrenze für direkte CP-Verletzung im $K^0(\bar{K}^0) \rightarrow \pi^0 \pi^0 \pi^0$ Zerfall ergeben. Ausserdem wird es die Unsicherheit in gegenwärtigen und zukünftigen CPT Tests, welche φ_{+-} mit der superschwachen Phase φ_{SW} vergleichen, reduzieren.

Chapter 1

Introduction

CP violation was discovered in 1964 [1] by observing the CP violating $K_L^0 \rightarrow \pi^+\pi^-$ decays. The branching ratio of these decays is low, $\approx 2 \cdot 10^{-3}$. Up to now the effect of CP violation has been only observed in the neutral kaon system by studying the decays $K^0 \rightarrow \pi^+\pi^-(\pi^0\pi^0)$, $K^0 \rightarrow \pi l \nu$ and $K^0 \rightarrow \pi^+\pi^-\gamma$. The standard model of electro-weak interactions with three fermion families is able to accommodate CP violation through the complex quark mixing expressed in Cabibbo-Kobayashi-Maskawa (CKM) matrix. The standard model parametrizes CP violation without giving an explanation for its origin. The observation of CP violation is also expected in the B -meson system [2].

The CPLEAR experiment at CERN represents a new approach to the measurement of CP violation in the neutral kaon system [3]. It uses pure K^0 and \overline{K}^0 initial states which are produced in $p\overline{p}$ annihilation. The strangeness of the neutral kaon is known from the charge of the accompanied particles produced in the annihilation processes:

$$\begin{aligned} p\overline{p} &\rightarrow K^-\pi^+K^0 \\ &\rightarrow K^+\pi^-\overline{K}^0 \end{aligned} \quad (1.1)$$

Events which originate from one of the above reactions will be called in the following the "golden events". The effect of CP violation is measured by comparing the rates of CP conjugated decays. Any difference seen in the time dependent asymmetry:

$$A(t) = \frac{R(\overline{K}^0_{t=0} \rightarrow \overline{f}) - R(K^0_{t=0} \rightarrow f)}{R(\overline{K}^0_{t=0} \rightarrow \overline{f}) + R(K^0_{t=0} \rightarrow f)} \quad (1.2)$$

is a manifestation of CP violation. By using this method, systematic errors are highly suppressed because of the cancellation of detector acceptances which enter in equation 1.2 in the numerator as well as in the denominator.

In this thesis we describe the study of CP violation by analyzing the decays of neutral kaons into two and three neutral pions. In the study of $K^0 \rightarrow \pi^0\pi^0$ ¹ events, electron-positron pairs originating from Dalitz decays of neutral pions ($\pi^0 \rightarrow e^+e^-\gamma$) or from

¹Unless explicitly stated, we mean by K^0 either K^0 or \overline{K}^0 .

photon conversion ($\gamma \rightarrow e^+e^-$) are used to reconstruct the neutral kaon decay vertex. The remaining three photons are not used in the vertex reconstruction. Using this method of the vertex reconstruction the lifetime dependent asymmetry is observed. The approach presented in this thesis is complementary to another CPLEAR analysis using four photons from the $K^0 \rightarrow \pi^0\pi^0 \rightarrow 4\gamma$ decay chain detected in the electromagnetic calorimeter for the reconstruction of the K^0 decay vertex [4]. The choice of e^+e^- pairs is motivated by the higher precision of the vertex reconstruction using tracks of charged particles.

CP violation has never been observed in $K^0 \rightarrow \pi^0\pi^0\pi^0$ decays. Only an upper limit is given [5] by the bubble chamber experiment performed at ITEP (Moscow). Comparing to this experiment CPLEAR can provide much more reconstructed events, however we have to deal with worse K^0 lifetime resolution and higher backgrounds.

CPLEAR is the first experiment searching for the particle-antiparticle asymmetry in the $K^0 \rightarrow \pi^0\pi^0\pi^0$ channel. Improved upper limit on $\mathcal{I}m(\eta_{ooo})$ would give a better limit on the direct CP violation in this channel, since the direct CP violation effects only the imaginary part of η_{ooo} . Better knowledge of $\mathcal{I}m(\eta_{ooo})$ would also reduce the uncertainty of CPT tests comparing the phase of η_{+-} with the superweak phase φ_{SW} .

The aim of the analysis is to demonstrate that the CPLEAR experiment is able to improve the present upper limit on the CP violation parameter η_{ooo} . In this analysis the neutral kaon lifetime is obtained from a full event reconstruction using six photons from the K^0 decay chain ($K^0 \rightarrow \pi^0\pi^0\pi^0 \rightarrow 6\gamma$). The photons are detected in the electromagnetic calorimeter. The analysis is performed on the test sample of 1/4 of all the collected events. For this analysis the special procedures for background suppression and monitoring are developed. They allow the substantial background reduction and precise monitoring of remaining background contributions.

We also present the analysis of photons originating from secondary interactions of charged particles ("fake photons"). Since in various analysis channels photons are used to reconstruct the neutral kaon decay vertex (for example both analyses described in this thesis), fake photons are a significant background source. The properties of fake photons and methods to suppress them are described.

Chapter 2

Symmetries

The reason for the study of symmetries is that they constitute a very direct connection between properties of the physical law, expressed by a Hamiltonian, and a set of suitably chosen experimental observations. According to Noether's theorem [6] a continuous symmetry group implies a conservation law. For example the space translation invariance implies conservation of linear momentum, the time translation invariance leads to the energy conservation. In quantum physics discrete symmetries play especially important role.

2.1 Discrete Symmetries

We define a symmetry as a group of transformations which leaves all physical observables unchanged. Let the time development of a system be described by the Hamiltonian H . If the wave function ψ is an eigenstate of the Schrödinger equation then $S(\psi)$ is also an eigenstate, when the operator S commutes with the Hamiltonian H :

$$[S, H] \equiv SH - HS = 0 \quad (2.1)$$

An important role in physics is played by the three discrete symmetries, parity P , charge conjugation C and time reversal T .

Parity

The operation of space inversion reflects all spatial coordinates about the origin. It reverses the position and momentum of every particle, changes the sign of the \vec{E} field but not the \vec{B} field. Classical mechanics and electrodynamics are invariant under the P transformation when no dissipating processes are acting. P invariance means that the result of an experiment with a reflected apparatus is the reflected result of the corresponding experiment with the original apparatus.

Charge Conjugation

This transformation turns every particle to its antiparticle, whereby all additive quantum numbers change their sign. C invariance means, that an experiment performed in the antiparticle world would give exactly the same result as the one built in our particle world. It would be impossible to define in an unique way what is an antiparticle and what is a particle.

Time Reversal

The third discrete symmetry is time reversal denoted T . It reverses the direction of time, so it reverses linear and angular momenta and it exchanges the initial state with the final state, and vice versa. Classical mechanics and electrodynamics are invariant under the T transformation.

2.2 Symmetries in Particle Physics

For a long time it was assumed that all elementary processes are invariant separately under C , P and T transformations. The electromagnetic and strong interactions are invariant under these transformations. In 1956 the work of Lee and Yang [7] questioned these invariances and P violation was shown experimentally by Wu [8] in the weak decays of nuclei. They observed the asymmetry in the β decays of polarized Co^{60} nuclei. Consequently P and C violation was observed in the decays of pions and muons [9, 10]. It was shown, that in the leptonic weak interactions the C and the P symmetries are maximally violated.

However, it was still assumed that CP invariance holds, which can be confirmed by the longitudinal polarization of neutrinos [11]. Neutrinos are always left-handed while the antineutrinos are right-handed. The application of P to a left-handed neutrino leads to a right-handed neutrino which is an unphysical state. Similarly the C operation transforms the left-handed neutrino to an unphysical left-handed antineutrino. Only the combination of both transformations, a CP transformation transforms the left-handed neutrino into the right-handed antineutrino, which really exists (fig. 2.1).

In 1955 Gell-Mann and Pais [12] predicted the existence of a long living partner to the known particle K_1^0 ($\tau_{K_1} \approx 10^{-10}$ sec). The K_1^0 particle and its partner are mixtures of K^0 and \bar{K}^0 which are the strangeness eigenstates ($S(K^0) = +1$ and $S(\bar{K}^0) = -1$) produced in the strong interactions. From the assumption of CP conservation in the weak interactions it follows that the mass eigenstates could be chosen as the CP eigenstates. With $\bar{K}^0 = CP(K^0)$ we set the eigenstates:

$$\begin{aligned} K_1 &= \frac{\bar{K}^0 + K^0}{\sqrt{2}} \quad , \quad CP(K_1) = K_1 \\ K_2 &= \frac{\bar{K}^0 - K^0}{\sqrt{2}} \quad , \quad CP(K_2) = -K_2 \end{aligned} \tag{2.2}$$

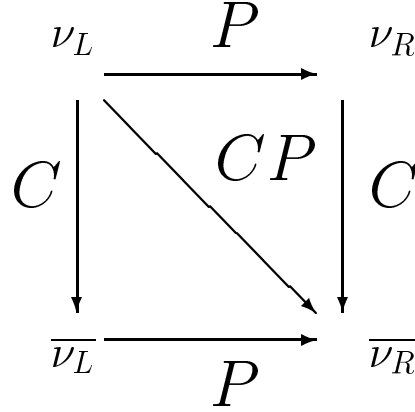


Figure 2.1: C , P and CP transformation applied to a left-handed neutrino.

The K_1 particle can decay into two pions, since the $CP|\pi^+\pi^- \rangle = +1|\pi^+\pi^- \rangle$. By CP conservation such a decay is forbidden for the K_2 which has to decay into other states which can have $CP = -1$ (e.g. three pions). The available phase space is smaller in the decays into three pions which causes the lifetime of K_2 to be longer than the one of K_1 . The existence of the long lived K_2 ($\tau_{K_2} \approx 10^{-8}$ sec) was confirmed experimentally [13, 14].

However, in 1964 it was discovered [1] that the long lived kaon also decays into $\pi^+\pi^-$ final states. The branching ratio of this process is low, $\approx 2 \cdot 10^{-3}$. This was the first evidence, that the combined CP symmetry is slightly violated in the weak interactions, and therefore it is not a good symmetry of nature.

The combined CPT transformation seems to be a symmetry preserved in all interactions. All of the experiments performed up to now confirmed the theorem predicting the CPT invariance. CPT conservation is a property of quantum field theory which follows from locality, causality and Lorentz invariance [15].

Some approaches to quantum gravity suggest that quantum field theory should be modified in a way which induces a violation of CPT [16]. The neutral kaon system may be used to probe the validity of CPT symmetry as well as of the preservation of the coherence of the wave function during its time development. Such tests were performed by the CPLEAR experiment [17] giving upper limits of the CPT violation parameters as well as of quantum mechanics violation parameters whose values are approaching the sensitivity range suggested by certain ideas concerning the quantum gravity.

Chapter 3

Phenomenology of the K^0 and \overline{K}^0 System

3.1 The Neutral Kaon System

In 1946 new particles, which we now call kaons, were discovered [18]. They carry a quantum number called strangeness S , which in the quark model is associated with the third, strange quark. The strangeness $S = -1(+1)$ is given to the $s(\overline{s})$ quark, respectively. The strangeness of the kaons is:

$$\begin{array}{llll} K^0 & K^+ & S = +1 & \overline{s} \text{ quark} \\ \overline{K}^0 & K^- & S = -1 & s \text{ quark} \end{array}$$

Strangeness is conserved in the strong interactions but not in the weak interactions. The K^0 and \overline{K}^0 mesons are strangeness eigenstates and they are chosen as eigenstates of strong and electromagnetic interactions with the masses m_o and \overline{m}_o respectively. Their masses are equal if CPT is conserved. The CP , CPT and T operators transform the neutral kaons as follows:

$$\begin{array}{llll} CP|K^0\rangle & = & |\overline{K}^0\rangle & , \\ CPT|K^0\rangle & = & |\overline{K}^0\rangle & , \\ T|K^0\rangle & = & |K^0\rangle & , \end{array} \quad \begin{array}{llll} CP|\overline{K}^0\rangle & = & |K^0\rangle & \\ CPT|\overline{K}^0\rangle & = & |K^0\rangle & \\ T|\overline{K}^0\rangle & = & |\overline{K}^0\rangle & \end{array} \quad (3.1)$$

The values of the parameters describing the neutral kaon system are summarized in table 3.1 [19].

3.1.1 Time Evolution of the $K^0 - \overline{K}^0$ System

The weak interactions do not conserve strangeness, hence through these interactions the neutral kaons can decay into final states with zero strangeness, for example to states made up of only pions. The non-conservation of strangeness also allows $K^0 \leftrightarrow \overline{K}^0$ transitions, since there is no quantum number forbidding this process. Therefore K^0 and \overline{K}^0 are not mass eigenstates.

τ_S	$(0.8926 \pm 0.0012) \cdot 10^{-10} \text{ s}$
τ_L	$(5.17 \pm 0.04) \cdot 10^{-8} \text{ s}$
m_{K^0}	$(497.672 \pm 0.031) \text{ MeV}$
$\Delta m = m_{K_L} - m_{K_S}$	$(0.5333 \pm 0.0027) \cdot 10^{10} \text{ } \hbar s^{-1}$
$\Gamma(K_S \rightarrow \pi^+ \pi^-)$	$(68.61 \pm 0.28)\%$
$\Gamma(K_S \rightarrow \pi^0 \pi^0)$	$(31.39 \pm 0.28)\%$
$\Gamma(K_S \rightarrow \pi^+ \pi^- \pi^0)$	$< 8.5 \cdot 10^{-5}$
$\Gamma(K_S \rightarrow \pi^0 \pi^0 \pi^0)$	$< 3.7 \cdot 10^{-5}$
$\Gamma(K_L \rightarrow \pi^+ \pi^-)$	$(2.03 \pm 0.04) \cdot 10^{-3}$
$\Gamma(K_L \rightarrow \pi^0 \pi^0)$	$(9.14 \pm 0.34) \cdot 10^{-4}$
$\Gamma(K_L \rightarrow \pi^+ \pi^- \pi^0)$	$(12.38 \pm 0.21)\%$
$\Gamma(K_L \rightarrow \pi^0 \pi^0 \pi^0)$	$(21.6 \pm 0.8)\%$
$\Gamma(K_L \rightarrow \pi \mu \nu)$	$(27.0 \pm 0.4)\%$
$\Gamma(K_L \rightarrow \pi e \nu)$	$(38.7 \pm 0.5)\%$
$\mathcal{R}e(\varepsilon)$	$(0.327 \pm 0.012)\%$
φ_{SW}	$43.59^\circ \pm 0.15^\circ$
$ \eta_{+-} $	$(2.269 \pm 0.023) \cdot 10^{-3}$
φ_{+-}	$44.3^\circ \pm 0.8^\circ$
$ \eta_{00} $	$(2.259 \pm 0.023) \cdot 10^{-3}$
φ_{00}	$43.3^\circ \pm 1.3^\circ$
$\varphi_{00} - \varphi_{+-}$	$-1.0^\circ \pm 1.0^\circ$
$ \eta_{000} ^2$	< 0.1
$\mathcal{I}m(\eta_{+-o})^2$	< 0.12
$\mathcal{R}e(\varepsilon'/\varepsilon)$	$(1.5 \pm 0.8) \cdot 10^{-3}$

Table 3.1: Basic parameters describing the neutral kaon system [19].

The most general wave function describing the time development of the neutral kaon is:

$$|\psi(t)\rangle = a(t)|K^o\rangle + b(t)|\overline{K}^o\rangle + \sum_f c_f(t)|f\rangle \quad (3.2)$$

where $|f\rangle$ denotes the final states, and $a(t)$, $b(t)$ and $c(t)$ are the time dependent functions. The wave function $\psi(t)$ fulfills the Schrödinger equation with a Hamiltonian $H = H_{st} + H_{em} + H_w$. The strong and electromagnetic interactions are much stronger than the weak interaction. We can denote $H = H_o + H_w$ where $H_o = H_{st} + H_{em}$ and treat a weak Hamiltonian as a small correction. We assume that the Hamiltonian H_o conserves CPT and CP .

Second order perturbation theory and the Wigner-Weisskopf method [20, 21] are used to solve the Schrödinger equation and to eliminate all states other than K^o and \overline{K}^o . We obtain an equation describing the time evolution of the system:

$$i\frac{\partial}{\partial t} \begin{pmatrix} a(t) \\ b(t) \end{pmatrix} = \left(M - i\frac{\Gamma}{2} \right) \begin{pmatrix} a(t) \\ b(t) \end{pmatrix} \quad (3.3)$$

where M and Γ are Hermitian 2×2 matrices, M is called the mass matrix and Γ the decay matrix. We should note that the number of kaons decreases with time due to the non-zero Γ matrix. The Hermitian Hamiltonians ensure the conservation of probability, i.e. the decay of the kaon is compensated by the appearance of the decay product. This leads to the following relations of the matrix elements:

$$\begin{aligned} M_{11}, M_{22}, \Gamma_{11}, \Gamma_{22} & \quad \text{all real} \\ M_{21} = M_{12}^* \quad , \quad \Gamma_{21} = \Gamma_{12}^* \end{aligned} \quad (3.4)$$

In the absence of the weak interactions we would obtain trivial solutions for the mass and decay matrices with $\Gamma = 0$ and a diagonal M matrix. If the weak Hamiltonian H_w is included in the calculations the resultant matrix elements are:

$$\begin{aligned} M_{ij} &= m_o \delta_{ij} + \langle i|H_w|j\rangle + \sum_f \mathcal{P} \left(\frac{\langle i|H_w|f\rangle \langle f|H_w|j\rangle}{m_o - E_f} \right) \\ \Gamma_{ij} &= 2\pi \sum_f \langle i|H_w|f\rangle \langle f|H_w|j\rangle \delta(m_o - E_f) \end{aligned} \quad (3.5)$$

where i, j are the indices denoting K^o and \overline{K}^o respectively, and \mathcal{P} stands for the principal part.

The off diagonal M matrix elements are, in the first order of H_w , responsible for the direct transitions $K^o \leftrightarrow \overline{K}^o$, while the second order elements correspond to the transitions through the virtual final states. The decay matrix Γ represents the neutral kaon decays into the real final states.

***CPT* Conservation**

If *CPT* is conserved then H_w commutes with the *CPT* transformation $[H_w, CPT] = 0$ and the diagonal elements of the H matrix fulfill the following relations:

$$\begin{aligned} H_{11} = H_{22} &\implies M_{11} = M_{22} \\ \Gamma_{11} &= \Gamma_{22} \end{aligned} \quad (3.6)$$

***T* Conservation**

If T is a good symmetry of the weak interactions $[H_w, T] = 0$ then it follows:

$$\begin{aligned} \langle \overline{K^0} | H_w | K^0 \rangle &= \langle K^0 | H_w | \overline{K^0} \rangle \\ \implies H_{21} &= H_{12} \\ \implies M_{12} - i\frac{\Gamma_{12}}{2} &= M_{12}^* - i\frac{\Gamma_{12}^*}{2} \end{aligned} \quad (3.7)$$

and M_{12} and Γ_{12} are both real.

***CP* Conservation**

CP conservation, i.e. $[H_w, CP] = 0$, leads to the following relations:

$$\begin{aligned} \langle K^0 | H | K^0 \rangle &= \langle \overline{K^0} | H | \overline{K^0} \rangle \\ \langle K^0 | H | \overline{K^0} \rangle &= \langle \overline{K^0} | H | K^0 \rangle \end{aligned} \quad (3.8)$$

which give the dependance between the matrix elements:

$$\begin{aligned} H_{11} = H_{22} &\implies M_{11} = M_{22} \text{ and } \Gamma_{11} = \Gamma_{22} \\ H_{21} = H_{12} &\implies M_{12} \text{ and } \Gamma_{12} \text{ are real} \end{aligned} \quad (3.9)$$

Summarizing the above discussion of the symmetries in the neutral kaon system we can distinguish the two possibilities:

$$\begin{array}{ll} M_{11} \neq M_{22} \text{ or } \Gamma_{11} \neq \Gamma_{22} & CPT \text{ and } CP \text{ are violated} \\ M_{12} \text{ or } \Gamma_{12} \text{ are complex} & T \text{ and } CP \text{ are violated} \end{array} \quad (3.10)$$

CP is not conserved in the both cases, also the *CP* violation cannot appear without either T or *CPT* violation.

3.1.2 Solution of the Schrödinger Equation

In this section we present a solution of the Schrödinger equation describing the time development of the neutral kaon system. We follow the basic lines presented by T. Nakada [22].

The time evolution of the neutral kaon system described by equation 3.3 is given by the wave function:

$$\begin{aligned} |\psi(t)\rangle &= a(t)|K^o\rangle + b(t)|\overline{K}^o\rangle \\ &= a_S e^{-i\lambda_S t} |K_S\rangle + a_L e^{-i\lambda_L t} |K_L\rangle \end{aligned} \quad (3.11)$$

where λ_S and λ_L are the eigenvalues of the Hamiltonian $H = M - i\Gamma/2$ (eq. 3.3) and $|K_S\rangle$ and $|K_L\rangle$ are the corresponding eigenvectors. They follow the exponential decay rule. The parameters a_S and a_L depend on the initial conditions.

The eigenvalues of the Hamiltonian H are found by solving the equation $\det(H - \lambda_{S(L)}) = 0$. The two solutions are:

$$\lambda_{S(L)} = \frac{H_{11} + H_{22}}{2} \pm \sqrt{\left(\frac{H_{22} - H_{11}}{2}\right)^2 + H_{12}H_{21}} \quad (3.12)$$

The corresponding eigenvectors $|K_S\rangle$ and $|K_L\rangle$ fulfilling the equation $H|K_{S(L)}\rangle = \lambda_{S(L)}|K_{S(L)}\rangle$ are given as:

$$\begin{aligned} |K_{S(L)}\rangle &= C_{S(L)} \left[|K^o\rangle \right. \\ &\quad \left. + \left(\frac{H_{22} - H_{11}}{2H_{12}} \pm \frac{1}{H_{12}} \sqrt{\left(\frac{H_{22} - H_{11}}{2}\right)^2 + H_{12}H_{21}} \right) |\overline{K}^o\rangle \right] \end{aligned} \quad (3.13)$$

where C_S and C_L are arbitrary constants. We can simplify the above formulas by introducing a new set of variables [23]:

$$\begin{aligned} \alpha &= \sqrt{\frac{H_{21}}{H_{12}}} \\ \varepsilon_{CPT} &= \frac{H_{22} - H_{11}}{4\sqrt{H_{12}H_{21}}} \\ r &= 2\varepsilon_{CPT} + \sqrt{1 + 4\varepsilon_{CPT}^2} \end{aligned} \quad (3.14)$$

We should notice that if there is no CPT violation than $\varepsilon_{CPT} = 0$ and $r = 1$ because of the equality $H_{11} = H_{22}$. Now we rewrite equations 3.12 and 3.13 substituting the new variables:

$$\begin{aligned} \lambda_S &= H_{11} + \alpha r H_{12} \\ \lambda_L &= H_{11} - \frac{\alpha}{r} H_{12} \\ |K_S\rangle &= \frac{1}{\sqrt{2}} (|K^o\rangle + \alpha r |\overline{K}^o\rangle) \\ |K_L\rangle &= \frac{1}{\sqrt{2}} \left(|K^o\rangle - \frac{\alpha}{r} |\overline{K}^o\rangle \right) \end{aligned} \quad (3.15)$$

where the factor $1/\sqrt{2}$ was chosen to give a proper normalization in case of CP and CPT conservation when $|\alpha| = r = 1$.

***CPT* and *CP* Conservation**

It is observed, that the short living K_S decays mostly into two pion final states with $CP = +1$, while the long living K_L into the $CP = -1$ final states. So, by neglecting CP violation, K_S has $CP = +1$ and K_L has $CP = -1$. The eigenvectors and eigenvalues of the Hamiltonian become in case of CPT and CP conservation ($\alpha = r = 1$):

$$\begin{aligned}\lambda_S &= H_{11} + H_{12} = m_S - i\frac{\Gamma_S}{2} \\ \lambda_L &= H_{11} - H_{12} = m_L - i\frac{\Gamma_L}{2} \\ |K_S\rangle &= \frac{1}{\sqrt{2}} (|K^0\rangle + |\overline{K}^0\rangle) \\ |K_L\rangle &= \frac{1}{\sqrt{2}} (|K^0\rangle - |\overline{K}^0\rangle)\end{aligned}\tag{3.16}$$

where we have defined:

$$\begin{aligned}m_{S(L)} &= \frac{M_{11} + M_{22}}{2} - (+) |M_{12}| \\ \Gamma_{S(L)} &= \frac{\Gamma_{11} + \Gamma_{22}}{2} + (-) |\Gamma_{12}|\end{aligned}$$

Both $m_{S(L)}$ and $\Gamma_{S(L)}$ are real and positive. The experiments show, that the long living K_L has larger mass than short living K_S . This fact is used to obtain the above formulas.

Small *CPT*, *CP* and *T* Violation

In case of small CPT and CP violation M_{12} and Γ_{12} are complex and we write:

$$\alpha = \sqrt{\frac{H_{21}}{H_{12}}} = (1 - 2\varepsilon_T) e^{-i\varphi_\Gamma}\tag{3.17}$$

where ε_T parametrizes the CP and T violation and $\varphi_\Gamma = \arg(\Gamma_{12})$. It should be noticed, that the phase of ε_T can be deduced from the above equation. It is equal to the phase of $|\Gamma_{12}|/2 + i|M_{12}|$, therefore:

$$\arg(\varepsilon_T) \approx \arctan \frac{2|M_{12}|}{|\Gamma_{12}|} \approx \arctan \frac{2\Delta m}{\Delta\Gamma}\tag{3.18}$$

where

$$\begin{aligned}\Delta m &= m_L - m_S = 2|M_{12}| \\ \Delta\Gamma &= \Gamma_S - \Gamma_L = 2|\Gamma_{12}|\end{aligned}$$

The phase of ε_T does not depend on CP violation. It is simply determined by the K_S and K_L mass and decay width differences. This phase is often referred as the "superweak" phase.

If we assume now, that CPT is conserved in the K^o decays and the only possible CPT violation originates from the $K^o - \overline{K}^o$ mixing, i.e. $\Gamma_{11} = \Gamma_{22}$ but $M_{11} \neq M_{22}$, then (see eq. 3.14):

$$\varepsilon_{CPT} = \frac{M_{22} - M_{11}}{4|M_{12}|^2 + |\Gamma_{12}|^2} (-2|M_{12}| + i|\Gamma_{12}|) \quad (3.19)$$

which gives the phase of ε_{CPT} :

$$\arg(\varepsilon_{CPT}) = \arctan \frac{-|\Gamma_{12}|}{2|M_{12}|} \quad (3.20)$$

i.e. ε_{CPT} is perpendicular to ε_T . We finally express the weak interaction eigenstates using the parameters ε_{CPT} and ε_T :

$$\begin{aligned} |K_S\rangle &= \frac{1}{\sqrt{2}} [(1 - 2\varepsilon_{CPT}) |K^o\rangle + (1 - 2\varepsilon_T) e^{-i\varphi_\Gamma} |\overline{K}^o\rangle] \\ |K_L\rangle &= \frac{1}{\sqrt{2}} [(1 + 2\varepsilon_{CPT}) |K^o\rangle - (1 - 2\varepsilon_T) e^{-i\varphi_\Gamma} |\overline{K}^o\rangle] \end{aligned} \quad (3.21)$$

The above formulas can be also reversed and K^o and \overline{K}^o states written as a combination of K_S and K_L states:

$$\begin{aligned} |K^o\rangle &= \frac{1}{\sqrt{2}} [|K_S\rangle + |K_L\rangle] \\ |\overline{K}^o\rangle &= \frac{1 + 2\varepsilon_T}{\sqrt{2}} e^{i\varphi_\Gamma} [(1 + 2\varepsilon_{CPT}) |K_S\rangle - (1 - 2\varepsilon_{CPT}) |K_L\rangle] \end{aligned} \quad (3.22)$$

The time development of the initially pure K^o or \overline{K}^o state is thus given by:

$$\begin{aligned} |K^o(t)\rangle &= \frac{1}{\sqrt{2}} (|K_S\rangle e^{-i\lambda_S t} + |K_L\rangle e^{-i\lambda_L t}) \\ |\overline{K}^o(t)\rangle &= \frac{1 + 2\varepsilon_T}{\sqrt{2}} e^{-i\varphi_\Gamma} ((1 + 2\varepsilon_{CPT}) |K_S\rangle e^{-i\lambda_S t} \\ &\quad - (1 - 2\varepsilon_{CPT}) |K_L\rangle e^{-i\lambda_L t}) \end{aligned} \quad (3.23)$$

since the eigenstates K_S and K_L follow the exponential decay rule.

3.2 CP Violation in the $K^o \rightarrow \pi\pi$ Decays

The main decay channels of the K_S component are the decays into the $\pi^+\pi^-$ and the $\pi^0\pi^0$ final states. They are the CP eigenstates with $CP = +1$.

3.2.1 CP Parity of the Final States

The wave function of a two pion system can be written as:

$$\psi = \varphi(space)\gamma(isospin) \quad (3.24)$$

Pions are bosons, so the total wave function must be symmetric under particle interchange. The wave function is symmetric when: $L + I = 0, 2, 4, \dots$, where L and I denote the angular momentum and isospin respectively. The C operator acts on the isospin part of the wave function and P on the space part therefore:

$$CP(\psi) = (-1)^{I+L}\psi \quad (3.25)$$

Therefore CP of the two pion system is always $+1$. So in the case of CP conservation the K_L decay into the two pion state would be forbidden. Observation of such a process was the first evidence of CP violation [1].

3.2.2 Observable Parameters

The CP violation parameters which can be measured experimentally are:

$$\eta_{+-} = \frac{\langle \pi^+\pi^- | H_w | K_L \rangle}{\langle \pi^+\pi^- | H_w | K_S \rangle} \quad \eta_{00} = \frac{\langle \pi^0\pi^0 | H_w | K_L \rangle}{\langle \pi^0\pi^0 | H_w | K_S \rangle} \quad (3.26)$$

Two pion final states are common for K^0 and \overline{K}^0 . They must be eigenstates of strong and electromagnetic interactions, so we consider them to be the isospin eigenstates. The amplitude of the K^0 and \overline{K}^0 decays into a final state with an isospin I is given by:

$$A_I = \langle I | H_w | K^0 \rangle = a_I e^{i\delta_I} \quad \overline{A}_I = \langle I | H_w | \overline{K}^0 \rangle = a_I^* e^{i\delta_I} \quad (3.27)$$

where $\langle I |$ denotes the final state with an isospin I and δ_I is a phase shift due to the strong interactions.

The decays of neutral kaons into the $I = 2$ final states are strongly suppressed by the $\Delta I = 1/2$ rule, which states that the physical processes prefer the transitions where the isospin changes by $1/2$. It was measured that [24]:

$$\left| \frac{a_2}{a_0} \right| \approx 0.045 \quad (3.28)$$

Let us define the parameters ε_0 and ε_2 which are a measure of the CP violation in the decays to the isospin eigenstates:

$$\varepsilon_0 = \frac{\langle I=0 | H_w | K_L \rangle}{\langle I=0 | H_w | K_S \rangle} \quad \varepsilon_2 = \frac{\langle I=2 | H_w | K_L \rangle}{\langle I=2 | H_w | K_S \rangle} \quad (3.29)$$

A two pion system can be decomposed as a mixture of the isospin eigenstates $I = 0$ and $I = 2$. Isospin $I = 1$ is not allowed, since the total angular momentum of a pion pair originating from K^0 decay is zero:

$$\begin{aligned} |\pi^+\pi^- \rangle &= \sqrt{\frac{2}{3}}|I=0 \rangle + \sqrt{\frac{1}{3}}|I=2 \rangle \\ |\pi^0\pi^0 \rangle &= -\sqrt{\frac{1}{3}}|I=0 \rangle + \sqrt{\frac{2}{3}}|I=2 \rangle \end{aligned} \quad (3.30)$$

We can now express the parameters η_{+-} and η_{00} by the newly defined variables ε_o and ε_2 :

$$\begin{aligned} \eta_{+-} &= \varepsilon_o + \frac{\varepsilon'}{1 + \frac{\omega}{\sqrt{2}}} \approx \varepsilon_o + \varepsilon' \\ \eta_{00} &= \varepsilon_o - 2\frac{\varepsilon'}{1 - \omega\sqrt{2}} \approx \varepsilon_o - 2\varepsilon' \end{aligned} \quad (3.31)$$

The two additional variables ω and ε' are introduced:

$$\begin{aligned} \omega &= \frac{\langle I=2|H_w|K_S \rangle}{\langle I=0|H_w|K_S \rangle} \\ \varepsilon' &= \frac{\omega}{\sqrt{2}}(\varepsilon_2 - \varepsilon_o) \approx \frac{i}{\sqrt{2}}\text{Im}\left(\frac{a_2}{a_o}\right) e^{i(\delta_2 - \delta_o)} \end{aligned} \quad (3.32)$$

The parameter ω describes the ratio of the amplitudes of the K_s decays into isospin 0 and 2 states. Since the value of $|\omega|$ is small (eq. 3.28), the terms quadratic in ω are neglected.

The parameter ε' describes the difference in the CP violation in the decays into different isospin eigenstates. It is a measure of direct CP violation in the neutral kaon decays. The phase of ε' is determined by the strong $\pi\pi$ phase shift $\arg(\varepsilon') = \frac{\pi}{2} + \delta_2 - \delta_o$. Experimentally it was found [25] that $\delta_2 - \delta_o = -42^\circ \pm 4^\circ$ so the $\arg(\varepsilon') = 48^\circ \pm 4^\circ$. The parameter ε' is nearly collinear with ε_T , the phase of which was found to be about 45° .

We should now find a connection between the parameter ε_o and parameters ε_T and ε_{CPT} . Using the equations 3.21 and 3.27 we can write:

$$\varepsilon_o = \frac{\langle I=0|H_w|K_L \rangle}{\langle I=0|H_w|K_S \rangle} = \frac{(1 + 2\varepsilon_{CPT})e^{i(\varphi_\Gamma - 2\varphi_o)} - (1 - 2\varepsilon_T)}{(1 - 2\varepsilon_{CPT})e^{i(\varphi_\Gamma - 2\varphi_o)} + (1 - 2\varepsilon_T)} \quad (3.33)$$

where $\varphi_o = \arg(a_o)$ and $\varphi_\Gamma = \arg(\Gamma_{12})$. Since CP is violated Γ_{12} is not necessarily real.

The parameter Γ_{12} is given by the solution of the Wigner-Weisskopf equation (eq. 3.5). Let us assume now, that the only possible intermediate final states are the two pion states. These can be the states with isospin $I = 0$ or $I = 2$. Using the neutral kaon decay amplitudes A_I and \overline{A}_I defined in eq. 3.27 we obtain:

$$\Gamma_{12} \sim A_o^*\overline{A}_o + A_2^*\overline{A}_2 = (|a_o|^2 + |a_2|^2) e^{-2i\varphi_o} \quad (3.34)$$

where we assume that $\arg(a_2) \approx \arg(a_0)$ which is deduced from the small value of ε' (see eq. 3.32 and tab. 3.1). In the above equation the constant real terms are omitted. We now see, that if two pion states were the only final states of the neutral kaon decays then $\varphi_\Gamma = -2\varphi_o$. The other decay channels, mostly the semileptonic decays and the decays into three pions, can in principle introduce a small phase shift. Assuming that $\Delta\varphi = 1/2(\varphi_\Gamma + 2\varphi_o)$ is small we obtain:

$$\varepsilon_o \approx \varepsilon_T + \varepsilon_{CPT} + i\Delta\varphi \quad (3.35)$$

In the literature there is a commonly used parameter $\varepsilon = \varepsilon_T + i\Delta\varphi$ which is very close to ε_T . Knowledge of the upper limit of $\Delta\varphi$ is very important for the precise CPT tests where the phase of η_{+-} is compared with the superweak phase (eq. 3.18). The upper limit of $\Delta\varphi$ can be obtained from the precise measurements of the semileptonic decays and the decays into three pions [26].

The dependencies between the CP violation parameters discussed in this section are presented graphically in the Wu-Yang diagram (fig. 3.1)

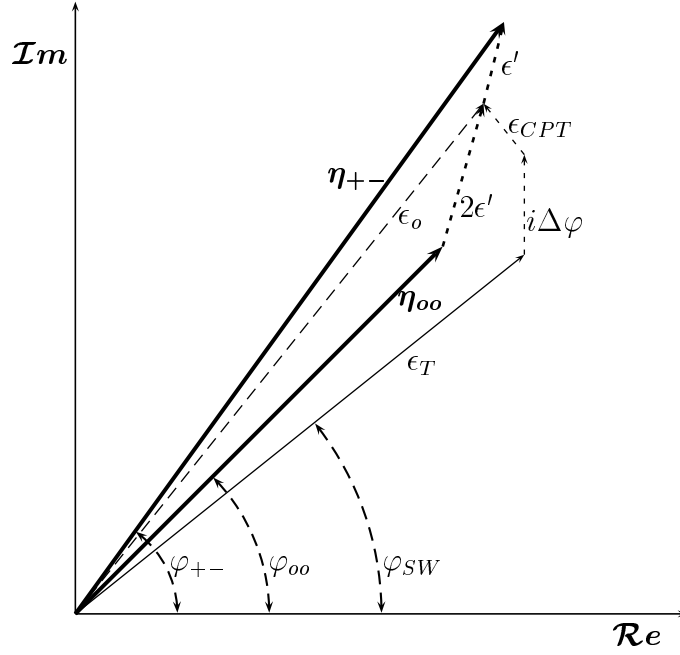


Figure 3.1: Wu-Yang diagram showing the dependencies between the CP violation parameters.

3.2.3 Decay Rates and Asymmetry

Using the equations 3.21, 3.23 and 3.26 and omitting the higher orders of ε_T and ε_{CPT} the decay rates of the initially pure K^o and \overline{K}^o states can be written as:

$$\begin{aligned}
R_{\pi\pi}(t) &= |\langle \pi\pi | H_w | K^o \rangle|^2 \\
&= \frac{|A_S|^2}{2} \left(e^{-\Gamma_S t} + |\eta_{\pi\pi}|^2 e^{-\Gamma_L t} + 2 |\eta_{\pi\pi}| e^{-\frac{\Gamma_S + \Gamma_L}{2} t} \cos(\Delta m t - \varphi_{\pi\pi}) \right) \\
\overline{R}_{\pi\pi}(t) &= |\langle \pi\pi | H_w | \overline{K}^o \rangle|^2 \\
&= (1 + 4\mathcal{R}e(\varepsilon_T + \varepsilon_{CPT})) \frac{|A_S|^2}{2} \\
&\quad \cdot \left(e^{-\Gamma_S t} + |\eta_{\pi\pi}|^2 e^{-\Gamma_L t} - 2 |\eta_{\pi\pi}| e^{-\frac{\Gamma_S + \Gamma_L}{2} t} \cos(\Delta m t - \varphi_{\pi\pi}) \right)
\end{aligned} \tag{3.36}$$

We should note, that decay rates differ from each other (fig. 3.2). This difference arises from the opposite signs at the oscillation term. Since $\Delta m \approx \Gamma_S/2$ it is possible to observe the interference before the K_S component disappears. The effect can be emphasized by presenting the neutral kaon decay rates in the form of the asymmetry (fig. 3.3):

$$\begin{aligned}
A_{\pi\pi}(t) &= \frac{\overline{R}_{\pi\pi}(t) - R_{\pi\pi}(t)}{\overline{R}_{\pi\pi}(t) + R_{\pi\pi}(t)} \\
&= 2\mathcal{R}e(\varepsilon_T + \varepsilon_{CPT}) - \frac{2 |\eta_{\pi\pi}| e^{-\frac{\Gamma_S - \Gamma_L}{2} t} \cos(\Delta m t - \varphi_{\pi\pi})}{1 + |\eta_{\pi\pi}|^2 e^{-\frac{\Gamma_S - \Gamma_L}{2} t}}
\end{aligned} \tag{3.37}$$

3.3 CP Violation in the $K^o \rightarrow \pi^o \pi^o \pi^o$ Decays

A state built out of three neutral pions is a CP eigenstate. Let consider the $3\pi^o$ final state as a system made up of the $\pi^o \pi^o$ pair and an additional π^o . In contrast to the $\pi^+ \pi^-$ pair which can have isospin 0, 1 or 2 while having any arbitrary angular momentum the isospin of the two neutral pions can be only 0 or 2 since the z -component of the π^o 's isospin is zero. The sum of isospin and angular momentum of two neutral pions is always even (sec. 3.2.1), so the angular momentum is even as well. The CP eigenvalue of the $\pi^o \pi^o$ pair is always +1. The three pions originate from a decay of a spinless particle K^o so the total angular momentum of the three pion system is zero. The angular momentum of the third pion relative to the $\pi^o \pi^o$ pair L is equal to the angular momentum of the $\pi^o \pi^o$ pair which is even.

The CP operator acting on the three pion state gives:

$$CP(\pi^o \pi^o \pi^o) = CP(\pi^o) (-1)^L CP(\pi^o \pi^o) \tag{3.38}$$

A pion has an intrinsic CP parity -1 , so finally we obtain $CP(\pi^o \pi^o \pi^o) = -1$. The total isospin of the $\pi^o \pi^o \pi^o$ state is 1 or 3.

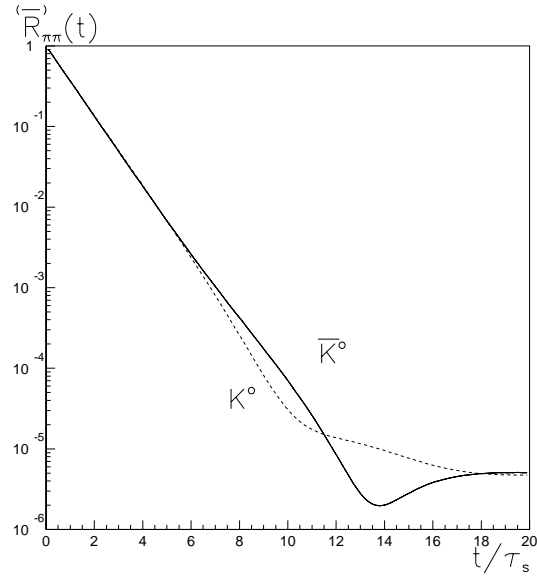


Figure 3.2: Decay rates of the initially pure K^0 ($R_{\pi\pi}(t)$) and \bar{K}^0 ($\bar{R}_{\pi\pi}(t)$) states into two pions.

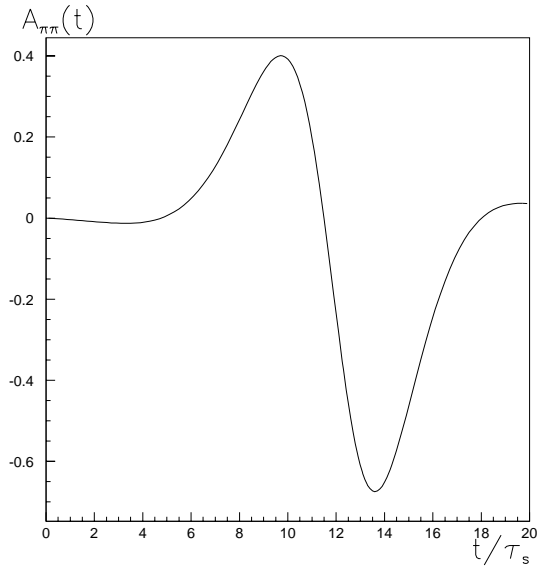


Figure 3.3: Lifetime dependent asymmetry $A_{\pi\pi}(t)$.

The CP violation parameter η_{ooo} is defined in a similar way to the previously introduced parameters η_{+-} and η_{oo} , as a ratio of the CP forbidden to the CP allowed amplitudes:

$$\eta_{ooo} = \frac{\langle 3\pi^o | H_w | K_S \rangle}{\langle 3\pi^o | H_w | K_L \rangle} \quad (3.39)$$

The decay into $I = 3$ final states would require $\Delta I = 5/2$ since the isospin of the neutral kaon is $1/2$, therefore they are strongly suppressed and will be neglected from now on. We repeat the procedure applied in subsection 3.2.2 for the two pion final states. First we define the amplitudes of the neutral kaon decays into isospin eigenstates:

$$\begin{aligned} C &= \langle 3\pi^o, I = 1 | H_w | K^o \rangle = c e^{i\delta_1^{3\pi}} \\ \overline{C} &= \langle 3\pi^o, I = 1 | H_w | \overline{K}^o \rangle = -c^* e^{i\delta_1^{3\pi}} \end{aligned} \quad (3.40)$$

The minus sign at the amplitude \overline{C} comes from $CP = -1$ of the $3\pi^o$ state. Decomposition of K_S and K_L into the strong interaction eigenstates K^o and \overline{K}^o (eq. 3.21) and the use of the phase $\varphi_o = -1/2 \arg(\Gamma_{12})$ (see sec. 3.2.2) gives:

$$\begin{aligned} \eta_{ooo} &= \frac{(1 - 2\varepsilon_{CPT}) e^{2i(\varphi_1^{3\pi} - \varphi_o)} - (1 - 2\varepsilon_T)}{(1 + 2\varepsilon_{CPT}) e^{2i(\varphi_1^{3\pi} - \varphi_o)} + (1 - 2\varepsilon_T)} \\ &\approx \varepsilon_T - \varepsilon_{CPT} + i(\varphi_1^{3\pi} - \varphi_o) \end{aligned} \quad (3.41)$$

where $\varphi_1^{3\pi} = \arg(c)$. The existence of the non-zero $\Delta\varphi_1^{3\pi} = \varphi_1^{3\pi} - \varphi_o$ is a sign of a direct CP violation in the $K^o \rightarrow \pi^o \pi^o \pi^o$ decays. The direct CP violation affects only the imaginary part of η_{ooo} . In the absence of a direct CP violation and CPT violation ($\varepsilon_{CPT} = 0$) we have $\eta_{+-} = \eta_{oo} = \eta_{ooo} = \varepsilon_T$.

The parameter η_{ooo} can be measured using the lifetime dependent asymmetry:

$$A_{ooo}(t) = \frac{\overline{R}_{ooo}(t) - R_{ooo}(t)}{\overline{R}_{ooo}(t) + R_{ooo}(t)} \quad (3.42)$$

The decay rates of the initially pure K^o and \overline{K}^o states into three neutral pions are given as:

$$\begin{aligned} R_{ooo}(t) &= |\langle \pi^o \pi^o \pi^o | H_w | K^o \rangle|^2 \\ &= \frac{|A_L|^2}{2} \left(e^{-\Gamma_L t} + |\eta_{ooo}|^2 e^{-\Gamma_S t} + 2|\eta_{ooo}| e^{-\frac{\Gamma_S + \Gamma_L}{2} t} \cos(\Delta m t + \varphi_{ooo}) \right) \\ \overline{R}_{ooo}(t) &= |\langle \pi^o \pi^o \pi^o | H_w | \overline{K}^o \rangle|^2 \\ &= (1 - 4\mathcal{R}e(\varepsilon_T + \varepsilon_{CPT})) \\ &\quad \frac{|A_L|^2}{2} \left(e^{-\Gamma_L t} + |\eta_{ooo}|^2 e^{-\Gamma_S t} - 2|\eta_{ooo}| e^{-\frac{\Gamma_S + \Gamma_L}{2} t} \cos(\Delta m t + \varphi_{ooo}) \right) \end{aligned} \quad (3.43)$$

Substituting these rates into 3.42 we obtain the asymmetry:

$$A_{ooo}(t) = 2\mathcal{R}e(\varepsilon_T - \varepsilon_{CPT}) - \frac{2|\eta_{ooo}| e^{-\frac{\Gamma_S - \Gamma_L}{2}t} \cos(\Delta mt + \varphi_{ooo})}{1 + |\eta_{ooo}|^2 e^{-\frac{\Gamma_S - \Gamma_L}{2}t}} \quad (3.44)$$

$$= 2\mathcal{R}e(\varepsilon_T - \varepsilon_{CPT}) - \frac{2e^{-\frac{\Gamma_S - \Gamma_L}{2}t} (\mathcal{R}e(\eta_{ooo}) \cos(\Delta mt) - \mathcal{I}m(\eta_{ooo}) \sin(\Delta mt))}{1 + |\eta_{ooo}|^2 e^{-\frac{\Gamma_S - \Gamma_L}{2}t}} \quad (3.45)$$

It differs from the 2π asymmetry by the signs of the phase φ_{ooo} and CPT violation parameter ε_{CPT} . The above decay rates and the asymmetry are presented in figures 3.4 and 3.5. We should notice, that the asymmetry can only be observed at short lifetimes. The value of η_{ooo} has not been measured to date, only the upper limit is given as $|\eta_{ooo}|^2 < 0.1$ [5].

3.4 Models of CP Violation

It is possible to incorporate CP violation into the standard model. However a superweak model introducing a new CP violating interaction can not be ruled out by experimental data.

3.4.1 Standard Model

In the framework of the standard model $K^0 - \overline{K}^0$ mixing and decays of neutral kaons are due to the weak interactions. In the interactions an intermediate boson is exchanged. In the standard model there are three families of quarks and leptons. While there is no mixing among lepton families, the down type quarks (d , s and b , charge $-1/3$) mix to each other. The weak interaction eigenstates are:

$$\begin{pmatrix} d' \\ s' \\ b' \end{pmatrix} = V \begin{pmatrix} d \\ s \\ b \end{pmatrix}, \quad V = \begin{pmatrix} V_{ud} & V_{us} & V_{ub} \\ V_{cd} & V_{cs} & V_{cb} \\ V_{td} & V_{ts} & V_{tb} \end{pmatrix} \quad (3.46)$$

where V is a three by three unitary matrix called Cabibbo-Kobayashi-Maskawa (CKM) matrix [29]. The CP violation in the standard model appears due to the complex elements of the CKM matrix. It was shown by Jarlskog [30] that the level of CP violation is proportional to:

$$J = \mathcal{I}m[V_{ud}V_{cs}^*V_{ub}^*V_{cb}] \quad (3.47)$$

The CP violation in the $K^0 - \overline{K}^0$ oscillations is due to the complex couplings in the box diagrams describing this process (fig. 3.6).

The standard model predicts also a direct CP violation due to the interference between the tree and the penguin diagrams contributing to the neutral kaon decay

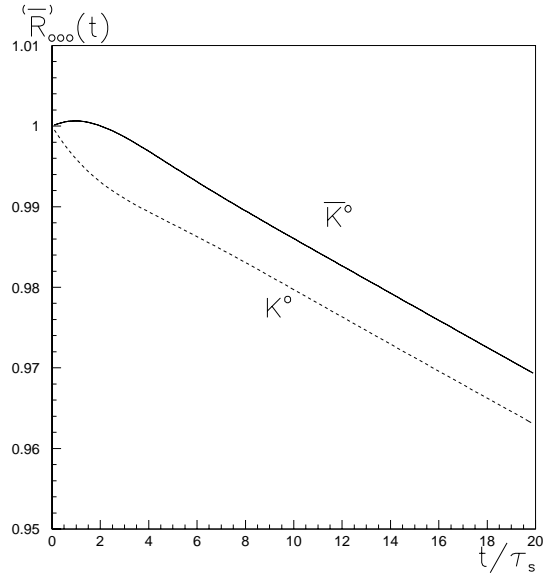


Figure 3.4: Decay rates of the initially pure K^0 and \overline{K}^0 states into three neutral pions.

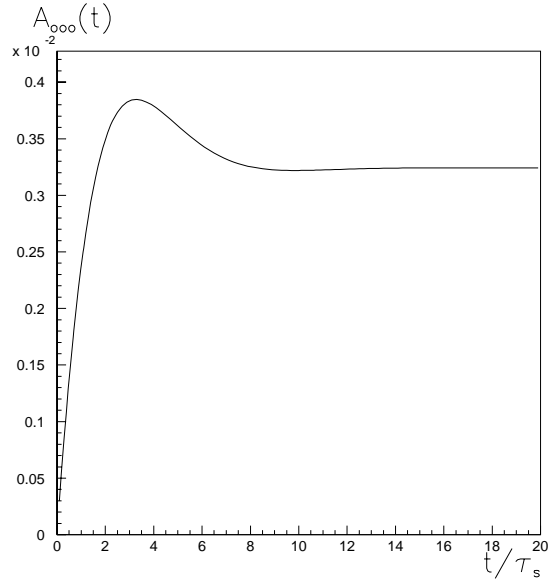
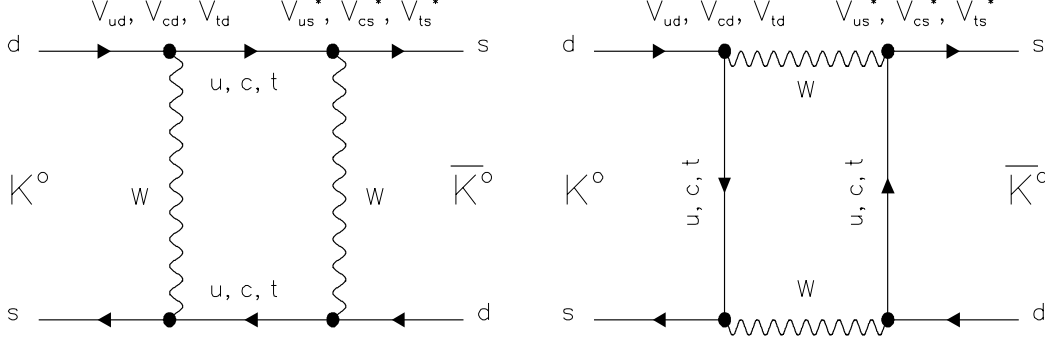
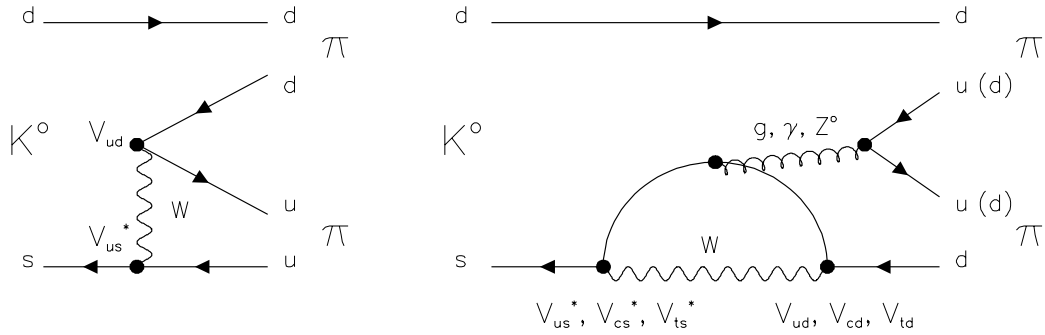


Figure 3.5: Lifetime dependent asymmetry $A_{ooo}(t)$ for the decays $K^0 \rightarrow \pi^0 \pi^0 \pi^0$.

Figure 3.6: Box diagrams describing the $K^0 - \bar{K}^0$ oscillations.

amplitude (fig. 3.7). In the penguin diagram complex couplings appear. If the observed CP violation in the K^0 system is due to complex elements of the CKM matrix then a direct CP violation in the decay amplitude must also exist. Measurement of $\varepsilon' \neq 0$ would be a confirmation of the standard model predictions.

Figure 3.7: Diagrams contributing to the $K^0 \rightarrow 2\pi$ decays.

3.4.2 Superweak Model

In this model the existence of an additional, CP violating force is assumed. It is called a superweak force [31]. The superweak interaction occurs due to the exchange of a heavy boson, which allows a direct $s \rightarrow d$ transition. The $K^0 - \bar{K}^0$ oscillations appear in the first order of the superweak interactions.

The neutral kaon decays are dominated by the standard CP conserving weak interactions. Therefore in the superweak model direct CP violation is much stronger suppressed than in the standard model and $\varepsilon' = 0$.

3.5 Interaction of Neutral Kaons with Matter

While traversing the detector material neutral kaons interact strongly with matter. The K^o s interact differently than \overline{K}^o s, therefore after going through material the proportion of K^o and \overline{K}^o components in the beam changes. This phenomenon is known as a regeneration. It can mimic or mask the effects of CPT and CP violation [27], because the kaons always interact with the matter of the apparatus and never with its CPT conjugate.

A general neutral kaon state can be written as a linear combination of mass or strangeness eigenstates:

$$\psi = a_L K_L + a_S K_S = a K^o + \bar{a} \overline{K}^o \quad (3.48)$$

The two sets of coefficients are related by equations 3.21 and 3.22:

$$\begin{aligned} a &= \frac{a_S + a_L}{\sqrt{2}} \\ \bar{a} &= (1 - 2\varepsilon_T) \frac{a_S - a_L}{\sqrt{2}} \end{aligned} \quad (3.49)$$

The kaon state ψ changes with a proper time t . The change consists of a vacuum and a nuclear part:

$$\frac{d\psi}{dt} = \left(\frac{d\psi}{dt} \right)_{vacuum} + \left(\frac{d\psi}{dt} \right)_{nuclear} \quad (3.50)$$

where the nuclear part describes the interactions of kaons with matter. The vacuum part can be written as (see eq. 3.11):

$$\left(\frac{d\psi}{dt} \right)_{vacuum} = -i\lambda_L a_L K_L - i\lambda_S a_S K_S \quad (3.51)$$

The nuclear part should be presented in the basis of the strong interaction eigenstates:

$$\left(\frac{d\psi}{dt} \right)_{nuclear} = -i\kappa a K^o - i\bar{\kappa} \bar{a} \overline{K}^o \quad (3.52)$$

where the coefficients κ and $\bar{\kappa}$ are related to the forward scattering amplitudes f and \bar{f} :

$$\begin{aligned} \kappa &= -\frac{2\pi N}{m} f \\ \bar{\kappa} &= -\frac{2\pi N}{m} \bar{f} \end{aligned} \quad (3.53)$$

where N is a scattering center density and m denotes the mass of the kaon state.

Combining the above equations we obtain Good's equations describing the change of the K_S and K_L contributions in the kaon beam [28].

$$\begin{aligned} i\frac{da_L}{dt} &= \lambda_L a_L + \frac{\kappa + \bar{\kappa}}{2} a_L + \frac{\kappa - \bar{\kappa}}{2} a_S \\ i\frac{da_S}{dt} &= \lambda_S a_S + \frac{\kappa + \bar{\kappa}}{2} a_S + \frac{\kappa - \bar{\kappa}}{2} a_L \end{aligned} \quad (3.54)$$

The strong interactions mix the K_S and K_L components. The mixing is specified by the regeneration parameter:

$$r = \frac{1}{2} \frac{\Delta\kappa}{\Delta\lambda} = -\frac{\pi N}{m} \frac{\Delta f}{\Delta\lambda} \quad (3.55)$$

where $\Delta\kappa = \kappa - \bar{\kappa}$, $\Delta\lambda = \lambda_L - \lambda_S$ and $\Delta f = f - \bar{f}$. In the lowest order of r the mass eigenstates in matter become:

$$\begin{aligned} K_S &\rightarrow K_S - rK_L \\ K_L &\rightarrow K_L + rK_S \end{aligned} \quad (3.56)$$

In the pure K_S or K_L beams after traversing a material appears an admixture of the other mass eigenstate. The effect is the same as by CPT violation, the regeneration parameter r plays the same role as ε_{CPT} . Therefore regeneration can mimic CPT violation effects.

Chapter 4

The CPLEAR Detector

The CPLEAR detector at CERN was constructed for studies of CP , T and CPT symmetries in the neutral kaon system. The experimental method consists of measuring asymmetries between the decay rates of initially pure K^o and \overline{K}^o states, which are produced in the proton-antiproton annihilation. The branching ratio for the golden annihilation channels ($p\overline{p} \rightarrow K^\mp \pi^\pm K^o(\overline{K}^o)$) is $\approx 0.4\%$. The strangeness of the neutral kaon is known by the charge of the accompanying kaon and is therefore known event by event. The momentum of the produced neutral kaon can be obtained from measurement of the $\pi^\pm K^\mp$ pair kinematics.

The CPLEAR experiment measures CP and T violation in the neutral kaon system by observing the decays:

$$\begin{aligned} K^o(\overline{K}^o) &\rightarrow \pi^+\pi^- \\ &\rightarrow \pi^o\pi^o \\ &\rightarrow \pi^+\pi^-\pi^o \\ &\rightarrow \pi e \nu_e \end{aligned} \tag{4.1}$$

which requires the detection of the charged and the neutral products of K^o decay. The CPLEAR approach to the studies of discrete symmetries dictates the following features of the detector:

- Capability to select desired events from the large number of multi-pion background events. This requires a good kaon identification and a fast, efficient trigger.
- The experimental setup must be able to detect various neutral kaon decay channels and distinguish between them.
- In order to measure the lifetime dependence of the $K^o - \overline{K}^o$ asymmetry the detector should be able to measure the neutral kaon decay eigentime between 0 and 15 lifetimes of K_S . The highest neutral kaon momentum measured in the CPLEAR experiment is around $750 \text{ MeV}/c$, therefore the required radius of the decay volume is $\approx 60 \text{ cm}$.

- Large number of events is necessary for studies of symmetries. This requires both a large geometrical coverage and a high annihilation rate.
- To minimize the neutral kaon regeneration, which modifies the lifetime dependent asymmetry, the amount of matter in the kaon decay volume must be minimized.

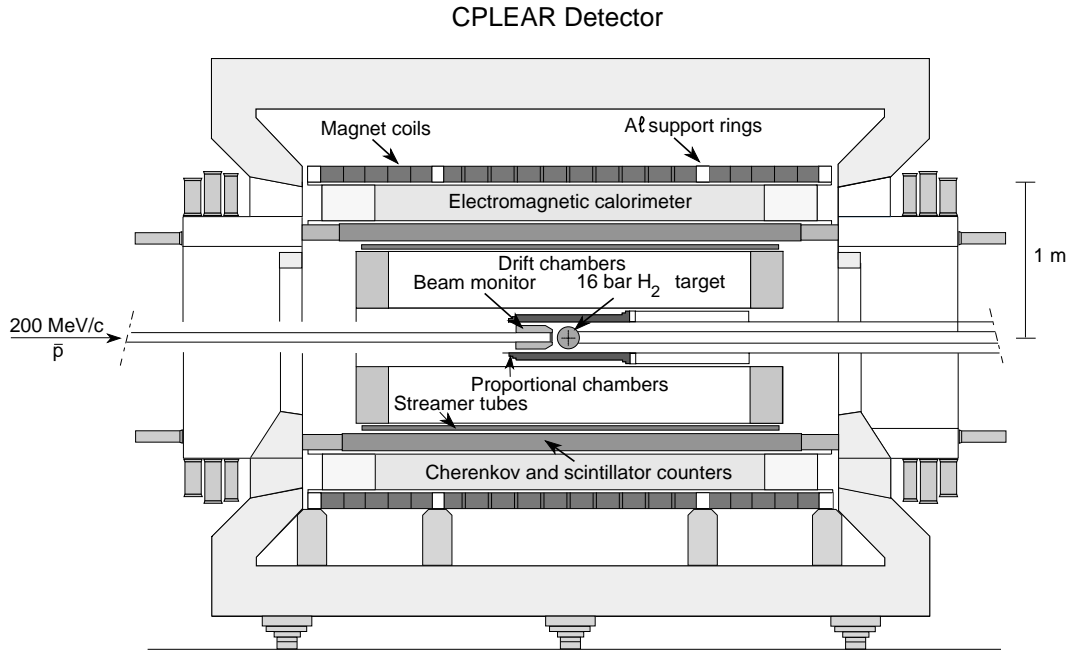


Figure 4.1: General layout of the CPLEAR detector.

In the CPLEAR detector (fig. 4.1) the antiprotons annihilate in a pressurized hydrogen gas target. Since the annihilation reaction takes place at rest the particles are emitted isotropically. The detector has a cylindrical form (3.6 *m* long, 2 *m* diameter). and covers the large fraction of the solid angle. The detector is placed inside a solenoid magnet providing a uniform magnetic field of 0.44 *T*.

The tracking detectors provide the information about the trajectories of charged particles. They allow the reconstruction of the particle momenta and vertices.

A particle identification detector (PID) is placed outside the tracking detectors. It consists of a threshold Čerenkov detector and of two plastic scintillators, which measure the energy loss and the time of flight of charged particles. The PID detector is used to separate kaons from pions and can also provide the separation between electrons and pions.

The photons produced in π^0 decays are detected in the lead-gas sampling electromagnetic calorimeter placed outside the PID detector. The calorimeter allows for a good photon impact point reconstruction with a moderate energy resolution.

The CPLEAR detector has been fully operational since 1992. During the last five years it was running smoothly and collected nearly $2 \cdot 10^8$ decays of neutral kaons, which allow precision studies of CP , T and CPT symmetries.

A detailed description of the CPLEAR detector can be found in [32]. Here we give only a brief overview of the components of the experimental setup.

4.1 Target, Beam Counter and Beam Monitor

The Low Energy Antiproton Ring (LEAR) supplies the high intensity antiproton beam. LEAR slows the antiprotons from the Antiproton Accumulator down to $200 \text{ MeV}/c$ and cools them providing a low momentum spread $\Delta p/p \approx 0.05\%$. It provides a constant intensity of $\approx 1 \text{ MHz}$ for $\approx 60 \text{ min}$, followed by $\approx 15 \text{ min}$ refilling period.

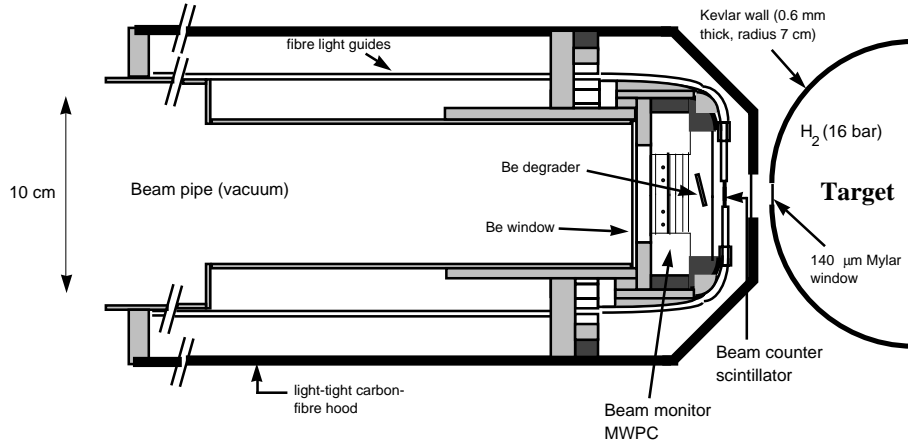


Figure 4.2: The beam pipe, beam monitor and target layouts.

The aim of the beam monitor, placed directly in front of the target (fig. 4.2), is to measure the position and shape of the beam. It is necessary to ensure, that the beam is centered on the target window. The beam monitor contains two orthogonal multiwire proportional chambers, which allow to center the beam with an accuracy of 0.1 mm (mean position of the beam center).

4.2 Tracking Detectors

The tracking detectors are used for the reconstruction of the charged particle tracks, momenta and vertices. They consist of two layers of proportional chambers, six drift chambers and two layers of streamer tubes.

4.2.1 Proportional Chambers

Two layers of cylindrical proportional chambers are the part of the tracking system closest to the annihilation vertex. The cross-section of a proportional chamber is shown in figure 4.3. Both contain 1344 axially placed anode wires and 1143 helical cathode strips. The distance between the anode wires is 1.039 mm , and between the cathodes 2.22 mm . The chambers are filled with a gas mixture containing 79.5% of argon, 20% of isobutane and 0.5% of freon 13B1. They operate at nominal high voltage of 2700 V giving 97% efficiency for a single layer. The measured spatial resolution averaged over the whole chamber is $340\text{ }\mu\text{m}$. The material traversed in one chamber by a particle is equivalent to $1.1 \cdot 10^{-3}$ radiation length (X_o) (see tab. 4.2).

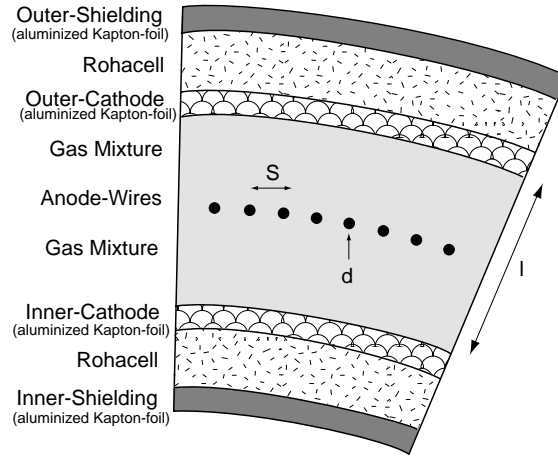


Figure 4.3: Section through part of a proportional chamber.

4.2.2 Drift Chambers

Outside the proportional chambers six cylindrical drift chambers form the main tracking detector. The signal wires of the chambers are parallel to the beam axis. The helicoidal cathode strips allow the measurement of the z -coordinate (along the beam axis) by calculating the centroid of the collected charges (fig. 4.4).

The drift cell size is limited to 5 mm to reduce the read-out time and supply the trigger with the fast tracking information. In order to remove the left-right ambiguity the double signal wires are used. This simplifies the track reconstruction procedure and speeds up the online reconstruction performed by the trigger hardware processors. The distance between the two sense wires having the same potential is kept by small epoxy glue balls placed every 20 cm along the wires.

The drift chambers operating at nominal high voltage of 2450 V are filled by a gas mixture containing 50% of argon and 50% of ethan. The spatial resolution given by the

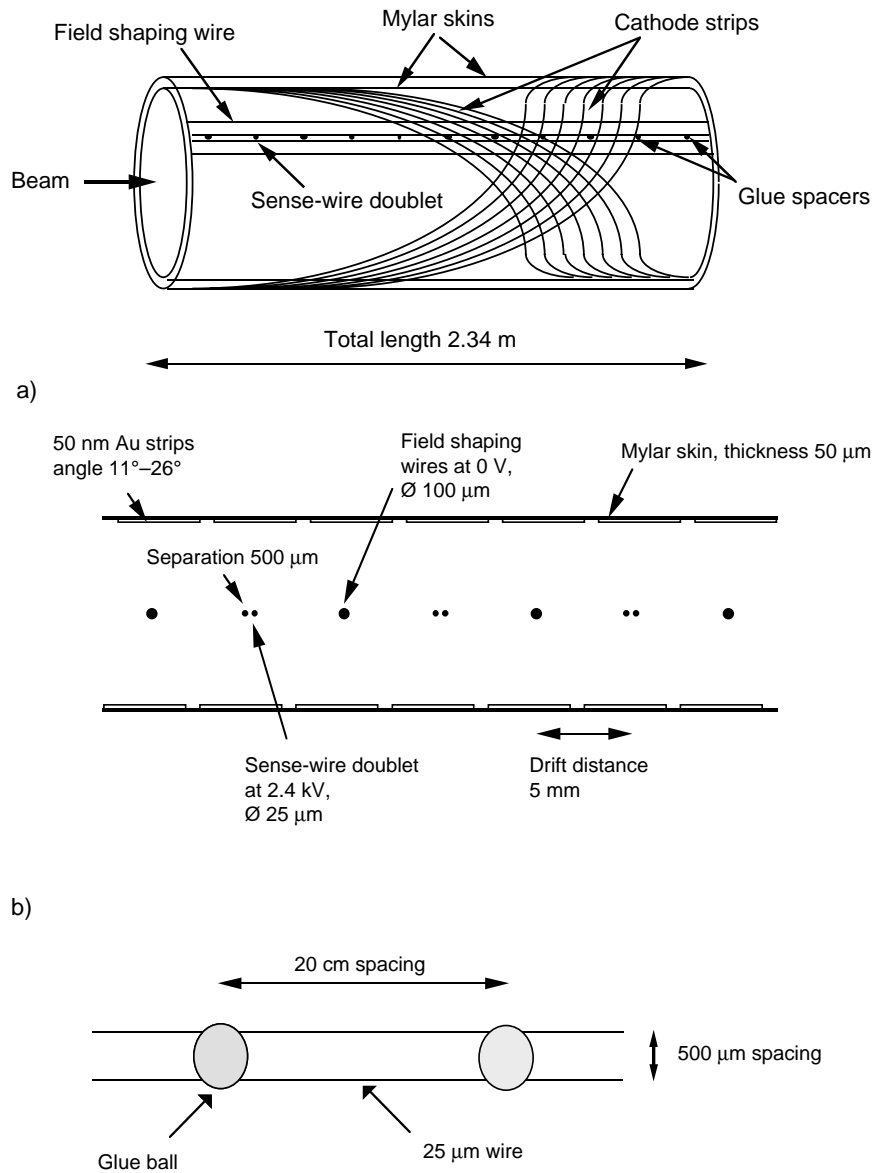


Figure 4.4: Schematic view of a drift chamber and details of the drift chamber geometry: a) drift cell, b) sense-wire doublet.

sense wire is 300 μm . In the direction parallel to the beam axis the achieved resolution is better than 3 mm.

4.2.3 Streamer Tubes

Two layers of streamer tubes form the outermost part of the tracking system. The main task of the streamer tubes is to provide a longitudinal position of tracks to the

trigger system. The trigger uses the streamer tube information in the online calculation of the event kinematics.

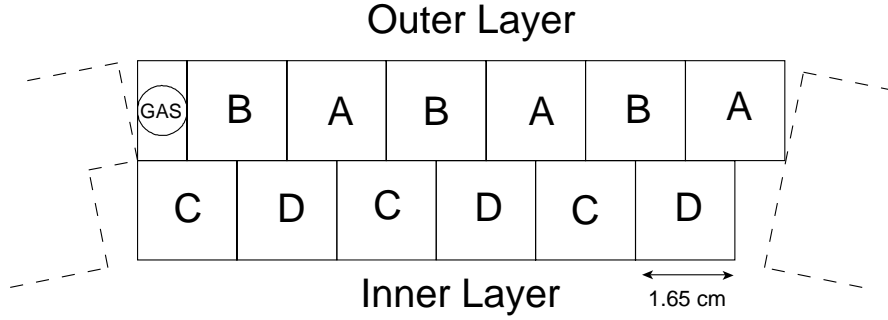


Figure 4.5: Layout of a streamer tube sector.

The detector consists of 384 discrete tubes with cross-section of $1.65 \times 1.65 \text{ cm}^2$ and length of 2.52 m . They are arranged in 32 identical modules to coincide with the sectors of the other detectors. The two layers of overlapping tubes (fig. 4.5) ensure the best hermeticity. The efficiency of a single layer is 98.2% for the operating voltage in the range of $4.2 - 4.5 \text{ kV}$, 1.1% efficiency loss is due to the walls between the tubes.

The streamer tubes filled with a mixture of argon, isobutane and methylal are operated in the limited streamer mode, which allows to get pulses having fast rise times and high amplitude. The axial track position is given by the difference of the propagation time of the pulse along the wire to each end of the tube. The achieved axial resolution is 1.4 cm .

4.2.4 Tracking Performance

The CPLEAR track finding algorithm requires at least three hits in the proportional and drift chambers. The track finding efficiency is better than 99%.

The transverse momentum resolution is shown in figure 4.6 as a function of particle momentum. The resolution is better, when the tracks originate from inside the proportional chambers, which give better spatial resolution than the drift chambers.

4.3 Particle Identification Detector

The separation of charged kaons and pions in the CPLEAR detector is crucial to select the desired events out of the overwhelming background of $p\bar{p}$ annihilations leading to the multi-pionic final states. The particle identification is performed using the 32 threshold Čerenkov counters. Each counter is sandwiched between two plastic scintillators (fig. 4.7). The thickness of the inner scintillator is 3 cm , of the Čerenkov counter 8 cm and of the outer scintillator 1.4 cm .

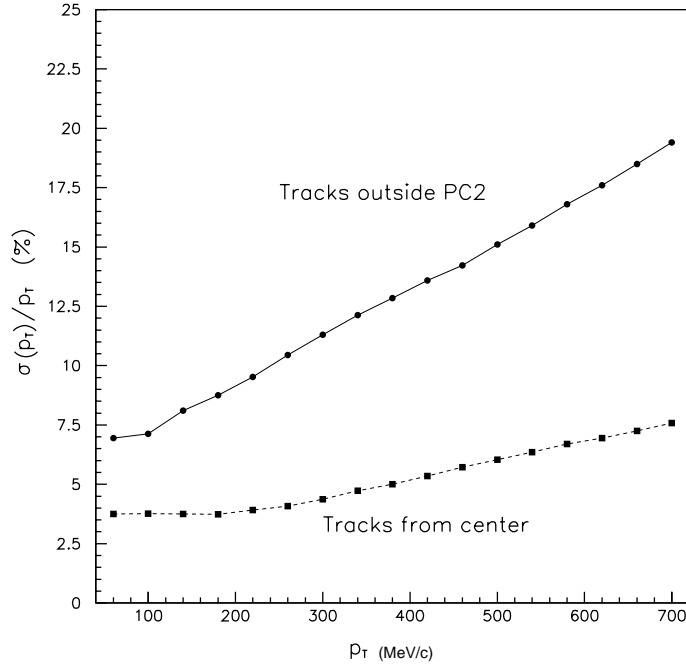


Figure 4.6: Relative resolution of the transverse momentum for charged tracks originating from either inside or outside the proportional chambers (obtained by Monte Carlo simulation).

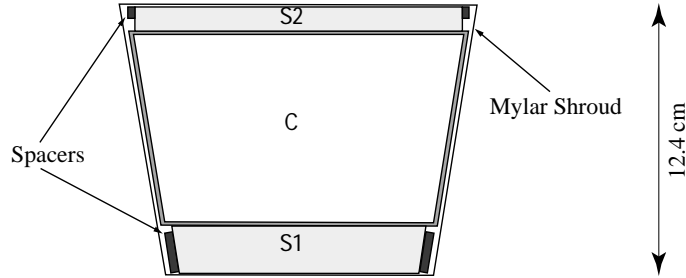


Figure 4.7: Cross-section of one of the particle identification detector segments. C marks the Čerenkov counter, $S1$ and $S2$ the scintillators.

The Čerenkov counter is filled with C_6F_{14} (fluorinert FC72) liquid which has a refractive index of 1.251 at 25° (refractive index corresponds to the threshold at $\beta = 0.80$). It meets the CPLEAR requirements, since the fastest charged kaons produced have a velocity $\beta = 0.84$ which dictates the threshold of the Čerenkov. When taking into account the energy losses in the plastic scintillator and inside the counter the threshold is lowered down to $\beta = 0.81$, which is close to the threshold given by FC72.

The readout is done by photomultiplieres which are placed in pairs at the ends of the counter. The small admixture (22 mg/l) of 2,5-diphenyl Oxazole wavelength

shifter improves the light yield.

The two scintillators ensure that the charged particle traversed the Čerenkov detector. A particle giving a signal in both scintillators but no light in the Čerenkov and having a transverse momentum over $350 \text{ MeV}/c$ is recognized as a charged kaon candidate by the first stage of the trigger. The efficiency of kaon detection is $\approx 75\%$ for the particle momenta above $350 \text{ MeV}/c$ (fig. 4.8). For the same momentum region the probability of pion misidentification as a kaon is $5.7 \cdot 10^{-3}$ (fig. 4.9).

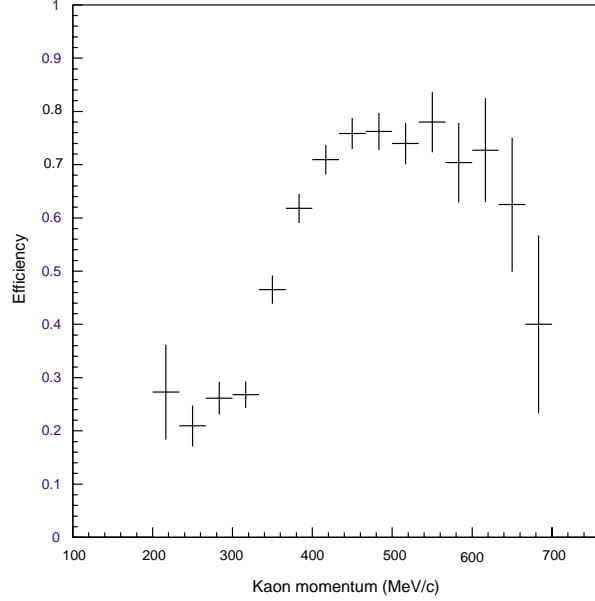


Figure 4.8: Kaon identification efficiency as a function of momentum.

The early trigger decision is later refined using the time of flight information and energy loss in the inner (thicker) scintillator. Figure 4.10 shows the dependance of the deposited energy on the particle momentum for kaons and pions. Good K/π separation is achieved for particles with momenta below $500 \text{ MeV}/c$.

The difference in the time of flight (ToF) between two tracks is measured using the scintillator signals. The timing resolution of the scintillator is $\approx 180 \text{ nsec}$. The measured ToF difference is compared to the theoretical time difference calculated using the particle momenta. Figure 4.11 shows, that the use of ToF difference improves the K/π separation.

4.4 Electromagnetic Calorimeter

The outermost detector is the electromagnetic calorimeter designed to detect photons originating from final states with neutral pions. The calorimeter was designed to have a good photon detection efficiency for low energetic photons ($50 - 500 \text{ MeV}$) and a

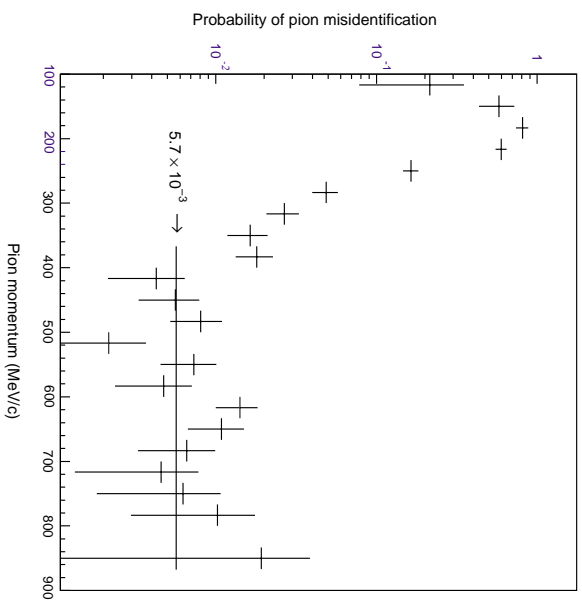


Figure 4.9: Probability of pion misidentification as a kaon presented as a function of pion momentum.

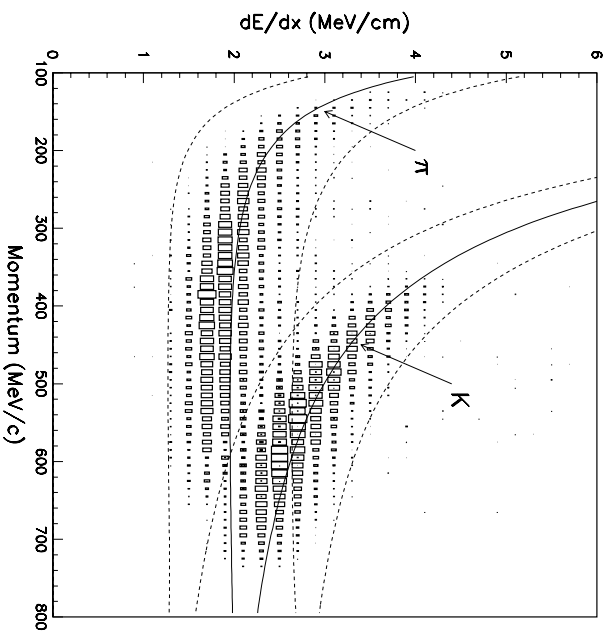


Figure 4.10: Energy loss in the inner scintillator by charged kaons and pions. The solid lines show the expected momentum dependence of the energy loss. The dashed lines form a band containing 92% of events.

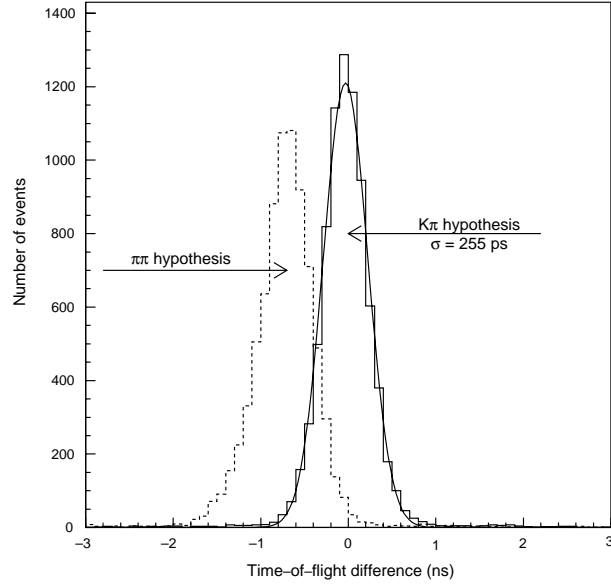


Figure 4.11: Time-of-flight difference between K and π for the whole accepted phase space of $p\bar{p} \rightarrow K^\mp \pi^\pm K^o(\bar{K}^o)$ events. The solid line corresponds to the correct particle assignment, the dashed line to the case where both particles are assumed to be pions.

good spatial resolution. For the reconstruction of the $K^o \rightarrow \pi^o \pi^o \rightarrow 4\gamma$ decay vertex a fairly poor energy resolution can be accepted, since the most important input is the position of the photon conversion points in the calorimeter.

The calorimeter is divided into three azimuthal sectors, each containing 18 layers of converter and sampling chambers. The construction of the calorimeter is shown in figure 4.12. The layer of $4 \times 4.5 \text{ mm}^2$ cross-section tubes is sandwiched between two layers of pick-up strips. The strips are crossing the wires at an angle of $\pm 30^\circ$ allowing the reconstruction of the z -coordinate. The calorimeter is built in form of a barrel without endcaps. It covers 75% of the the solid angle.

The chambers operating near to limited streamer mode are filled with a gas mixture of 55% CO_2 and 45% pentane and operate at 3000 V. The typical pulse from a wire is 20 mV as measured for a 50 Ω load, which allows a read-out without amplification. The strip signals need a preamplification to give a similar pulse height to the wires. Both wires and strips are read-out in digital mode using discriminators. The calorimeter contains in total 17 112 tubes and $\approx 44\,000$ pick-up strips.

A shower finding algorithm finds the clusters of hits separately in the wire projection and in the two strip projections. The searching algorithm requires at least three hits in at least two layers for the wire projection. For the strip projections only two hits are required. The matching of the three projections provides the shower conversion coordinates.

A shower is defined as the one originating from a neutral particle if its conversion

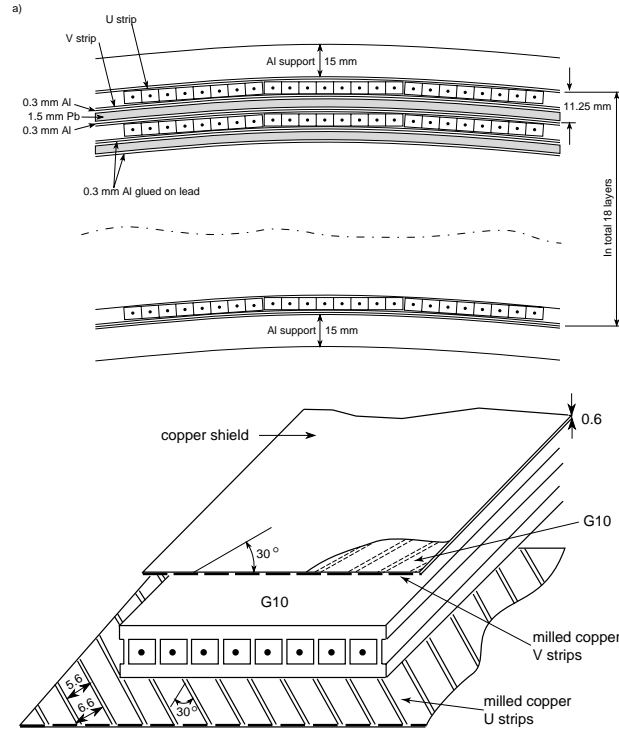


Figure 4.12: a) Transverse cross-section of the calorimeter. b) Geometrical setup of the layer of tubes sandwiched between two layers of pick-up strips.

point is separated from any charged track by at least 25 *cm*.

The energy is measured by counting the track segments. The obtained energy resolution is $\sigma(E)/E \approx 0.13/\sqrt{E(\text{GeV})}$ which depends on photon energy. The spatial resolution achieved is ≈ 5 *mm*.

The photon detection efficiency is shown in figure 4.13 as a function of photon energy. At 200 *MeV* it reaches the plateau of 90%. About half of the inefficiency is due to the calorimeter support structure.

4.5 Trigger

A fast and effective trigger is required due to the small branching ratio ($\approx 4 \cdot 10^{-3}$) for the desired golden events and a high beam intensity of 1 *MHz*. A multilevel hardwired processor system (HWP) is implemented for fast event selection.

The trigger should recognize a primary $K^\pm \pi^\mp$ pair and detect the neutral kaon decay products. The following decisions are taken by the trigger system (fig. 4.14):

1. Selection of events with at least two charged tracks identified by the hits in the inner scintillator (Early Decision Logic). At least one of the tracks must be a kaon candidate and give hits in inner and outer scintillator but no light in the

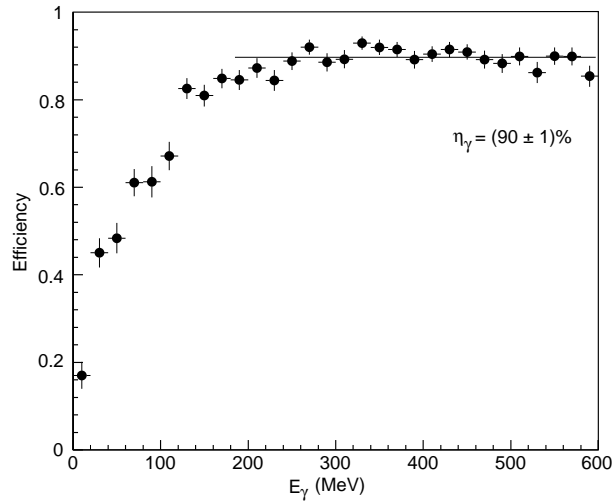


Figure 4.13: Photon detection efficiency in the electromagnetic calorimeter as a function of the photon energy.

Čerenkov counter. Kaon identification is improved by a transverse momentum cut which rejects slow pions.

2. Intermediate Decision Logic uses sectorized information from the tracking chambers and classifies the tracks depending on whether they originate from inside or outside the proportional chambers.
3. HWP1 performs various operations using the information from the tracking devices:
 - Pattern recognition.
 - Computation of track parameters.
 - Calculation of the momenta of tracks originating from inside the proportional chambers. A cut on a minimum value of the sum of K^\pm and π^\mp momenta for all $K^\pm\pi^\mp$ pairs is applied (the cut is equivalent to the $K^\pm\pi^\mp$ missing mass cut).
 - The charge balance is required for the events with an even number of tracks.
4. HWP2 makes use of the energy loss in the inner scintillator and time-of-flight information to improve the charged kaon identification.
5. HWP2.5 finds the number of showers in the electromagnetic calorimeter. For the events with two tracks originating from inside the proportional chambers, which are the candidates for neutral final state decays, the cut on the minimal number of showers is applied. This requirement eliminates events with K_L decays outside the fiducial volume.

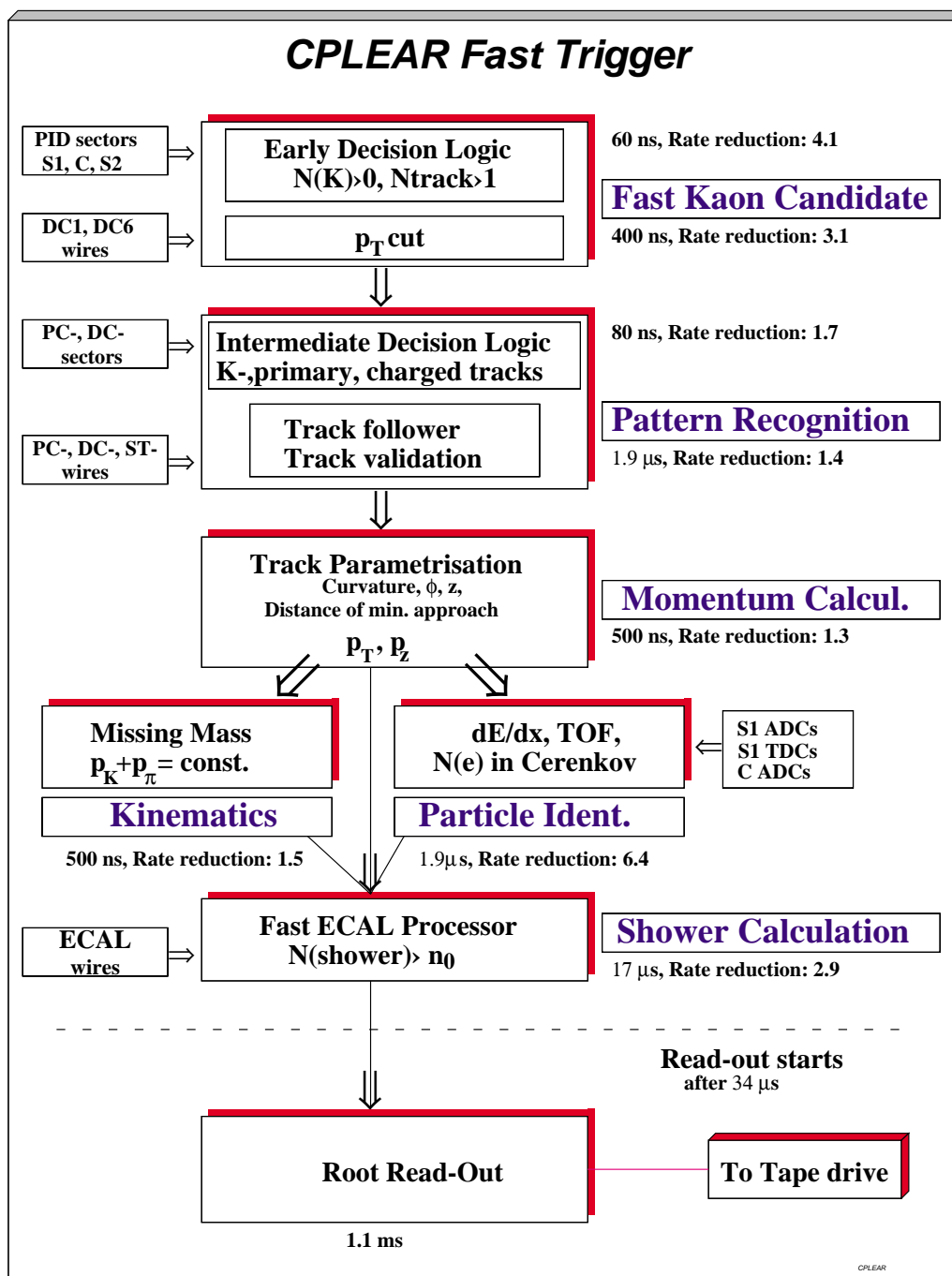


Figure 4.14: Logic and data flow diagram of the trigger system.

The overall trigger rejection factor is $\approx 10^3$. This allows an read-out rate of 450 events per second at 800 kHz beam rate (average beam intensity by data taking).

4.6 Distribution of Material in the CPLEAR Detector

The knowledge of the material distribution allows to estimate neutral kaon regeneration effects. Table 4.1 summarizes properties of materials used to build the detector. The amount of material in the various parts of the detector is presented in tables 4.2 and 4.3.

material	density [g/cm^3]	radiation length	
		[g/cm^2]	[cm]
hydrogen 16 bar	$1.236 \cdot 10^{-3}$	61.28	49500
kevlar	1.39	≈ 40	≈ 29
mylar	1.39	39.95	28.7
rohacell	0.050	40.55	811
gold	19.30	6.0	0.31
tungsten	19.30	6.76	0.35
bronze (copper)	8.96	12.86	1.43
kapton	1.42	≈ 41	≈ 29
araldite	1.1	≈ 38	≈ 35
gas PC	$1.958 \cdot 10^{-3}$	≈ 31	≈ 16000
gas DC	$1.568 \cdot 10^{-3}$	≈ 35	≈ 23000
carbon fibre	1.6	42.70	26.7
Al honeycomb	0.055	24.01	437

Table 4.1: Properties of materials used to construct detectors.

4.7 Data Processing

4.7.1 Data Acquisition

The data acquisition system transfers data from each sub-detector to the tape. It allows also monitoring of the data quality. The front end electronics, which differs from

detector part	material	r_{min} [mm]	r_{max} [mm]	surf. dens. [mg/cm ²]	amount of mat. [$X_o \times 10^{-3}$]
Target	hydrogen	0.0	69.42	8.6	0.14
	kevlar	69.42	70.0	80.0	2.00
PC-1					2.14
	kapton	90.250	90.275	3.5	0.09
	araldite	$\approx 15\mu m$ of glue		1.5	0.04
	rohacell	90.275	92.225	10.0	0.25
	araldite	$\approx 15\mu m$ of glue		1.5	0.04
	kapton	92.225	92.250	3.5	0.09
	gas PC	92.250	98.250	1.2	0.05
	tungsten	0.2 μm (15 μm wires)		0.3	0.05
	kapton	98.250	98.275	3.5	0.09
	araldite	$\approx 15\mu m$ of glue		1.5	0.04
	rohacell	98.275	100.225	10.0	0.25
	araldite	$\approx 15\mu m$ of glue		1.5	0.04
	kapton	100.225	100.250	3.5	0.09
					1.12
PC-2	kapton	122.0	122.025	3.5	0.09
	araldite	$\approx 15\mu m$ of glue		1.5	0.04
	rohacell	122.025	123.975	10.0	0.27
	araldite	$\approx 15\mu m$ of glue		1.5	0.04
	kapton	123.975	124.0	3.5	0.09
	gas PC	124.0	130.0	1.2	0.04
	tungsten	0.2 μm (15 μm wires)		0.3	0.05
	kapton	130.0	130.025	3.5	0.09
	araldite	$\approx 15\mu m$ of glue		1.5	0.04
	rohacell	130.025	131.975	10.0	0.27
	araldite	$\approx 15\mu m$ of glue		1.5	0.04
	kapton	131.975	132.0	3.5	0.09
					1.12

Table 4.2: Material distribution in target and proportional chambers.

detector part	material	r_{min} [mm]	r_{max} [mm]	surf. dens. [mg/cm ²]	amount of mat. [$X_o \times 10^{-3}$]
DC's					
DC-1	mylar	200.000	200.025	13.9	0.09
	rohacell	200.025	211.025	55.0	1.36
	mylar	211.025	211.050	13.9	0.09
	gas DC	210.050	250.000	6.3	0.17
	mylar	250.00	250.05	6.9	0.17
	gold	50nm stripes		0.01	0.016
	bronze+Be	0.8 μm (100 μm wires)		0.07	0.06
	tungsten	0.06 μm (20 μm wires)		0.1	0.02
	gas DC	250.05	260.00	1.6	0.04
	gold	50nm stripes		0.01	0.016
	mylar	260.00	260.05	6.9	0.17
	gas DC	260.05	300.00	6.3	0.17
DC-6					
DC support	mylar	505.05	505.05	6.9	0.17
	gold	50nm stripes		0.01	0.016
	bronze+Be	0.8 μm (100 μm wires)		0.07	0.06
	tungsten	0.06 μm (20 μm wires)		0.1	0.02
	gas DC	505.05	515.00	1.6	0.04
	gold	50nm stripes		0.01	0.016
	mylar	515.00	515.05	6.9	0.17
	gas DC	515.05	545.00	4.7	0.13
					5.6
	carbon fibre	545.0	546.0	160	3.7
	Al honeycomb	546.0	566.0	100	4.6
	carbon fibre	566.0	567.0	160	3.7
					12.0
ST		582	600		39
PID		620	744		543
Calorimeter		770	990		≈ 6000

Table 4.3: Material distribution in drift chambers, streamer tubes, PIDs and calorimeter.

detector to detector, digitizes and stores the data until a readout signal is received. It also passes information necessary to make a decision to the trigger.

The root readout system, separate for every sub-detector, receives data from the front end electronics. It formats data and monitors the data quality. Then the data are transferred to the Event Builder, which accepts data from each root readout. The complete event is built out of the information obtained from all the sub-detectors. If the event is finally accepted by the trigger it is stored on tape. The typical size of the stored event is ≈ 2.5 Kb.

4.7.2 Data Reduction and Processing

The process of data production consists of decoding, pattern recognition and later track and vertex fitting performed by the CPREAD software package [33]. Due to the large amount of data, the production is performed in various institutes participating in the CPLEAR experiment. After the production stage, the filtering process is performed in which tapes containing only candidates for one particular decay mode are written. These tapes are later used by various analysis groups for the study of physical processes.

Chapter 5

Neutral Showers from Secondary Interactions

In the study of the $K^0 \rightarrow \pi^0 \pi^0 \rightarrow 4\gamma$ [4] and the $K^0 \rightarrow \pi^0 \pi^0 \pi^0 \rightarrow 6\gamma$ decays (chapter 7) photons detected as showers in the calorimeter are used to reconstruct the neutral kaon decay vertex. Showers which are sufficiently far away from any charged track will be called neutral showers and are recognized as showers originating from photons. There are similar hit patterns looking like photon showers whose origin are not genuine photons from the K^0 decay chain. They are called fake showers. Fake showers can disturb the lifetime measurement and form a significant background source.

In this chapter we describe the properties of fake showers. We also present a method of suppressing such showers. The fake showers generated by CPGEANT [34], the Monte Carlo simulation program for CPLEAR, are compared with the fake showers found in the data in order to check, how well the simulation program is able to reproduce them.

5.1 Analysis of the Fake Showers

A method of identifying the neutral showers in the calorimeter is described in section 4.4, in which the electromagnetic calorimeter is presented. We require, that the neutral shower is at least 25 cm apart from any charged particle track. In addition to the standard criteria we also require, that two showers shall not share the same wire projection. A strip projection is allowed to be common for two different showers. This definition of a neutral shower is used in both $K^0 \rightarrow \pi^0 \pi^0 \rightarrow 4\gamma$ and $K^0 \rightarrow \pi^0 \pi^0 \pi^0 \rightarrow 6\gamma$ analyses.

In golden events ($p\bar{p} \rightarrow K^\mp \pi^\pm K^0(\bar{K}^0)$) with $K^0 \rightarrow \pi^+ \pi^-$ decays we do not expect any neutral showers in the calorimeter. Also in this channel we expect very little physical background [35], therefore any neutral shower found in a selected sample of such events is considered as a fake shower. A sample of approximately 35000 selected $K^0 \rightarrow \pi^+ \pi^-$ events is used for the study described below as a source of fake showers. We find on average 0.22 neutral showers per golden $K^0 \rightarrow \pi^+ \pi^-$ event.

5.1.1 Description of Fake Showers

Using the selected $K^0 \rightarrow \pi^+\pi^-$ events we now describe the fake showers found in the data sample.

Multiplicity: The frequency of occurrence of the fake showers (multiplicity) in the selected sample is shown in figure 5.1. The observed distribution is in good agreement with the exponential function $P(n) = a \cdot p^n$, where n is the number of detected fake showers and a, p are the fitted parameters. Such an agreement indicates, that the showers are created independently and that there is no significant correlation between them. The parameter p can be interpreted as the probability of generating a single fake shower per event. From the fit we obtain $p \approx 0.17$, which agrees with the observed average number of 0.22 fake showers per event ($\sum_{n=1}^{\infty} np^n = 0.24$).

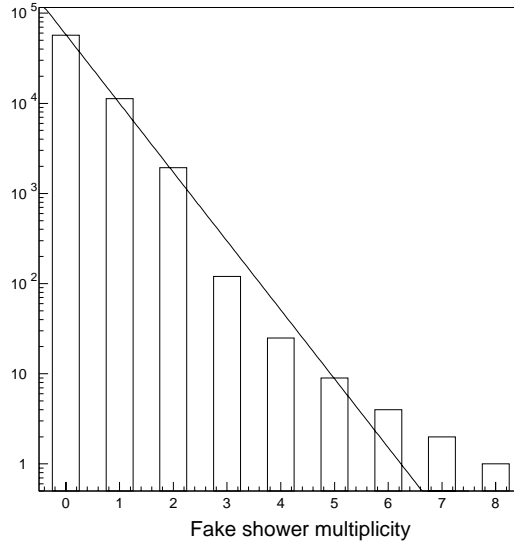


Figure 5.1: Multiplicity of neutral showers in $K^0 \rightarrow \pi^+\pi^-$ data shown together with a fitted exponential function.

Spatial distribution: In this paragraph we investigate the distance between the fake showers and the charged particle tracks. The distance is measured between the shower conversion point and the point, where the track intersects the calorimeter layer in which the conversion takes place.

The squared distance between a charged track and the closest shower is shown in figure 5.2. The neutral showers are grouped around the charged tracks. Such a halo is more distinct around a charged kaon track than around a pion track. The halo around

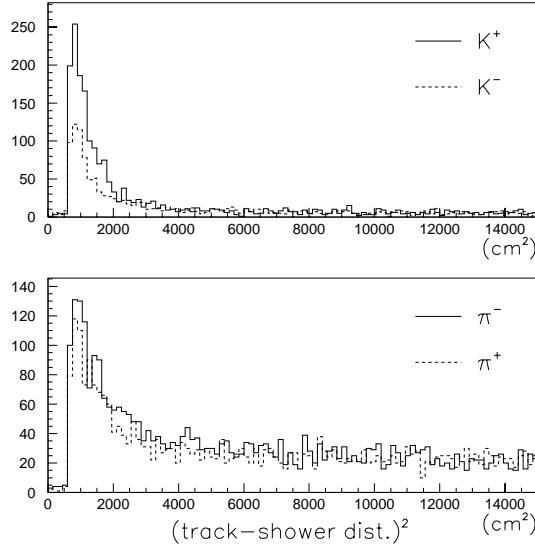


Figure 5.2: Squared distance between the track of the charged particle and the closest neutral shower found in $K^0 \rightarrow \pi^+\pi^-$ data. The cut-off at $(25\text{ cm})^2$ originates from the neutral shower selection criteria.

a K^+ track contains more showers than the halo around a K^- track. There is no pronounced difference between a π^+ and a π^- track.

The halo around a charged kaon track does not change significantly with particle momentum (fig. 5.3), however for pions we observe a significant dependence. Slow pions with momentum below $300\text{ MeV}/c$ do not reach the calorimeter and the halo is not observed (fig. 5.4). For faster pions a distinct halo around the track can be seen.

We can now investigate what fraction of the fake showers is grouped around the tracks of the charged particles. The distribution of the squared distance between a neutral shower and the closest track (fig. 5.5) shows, that approximately half of the fake showers found in the $K^0 \rightarrow \pi^+\pi^-$ data is closer than 50 cm to any track and the rest is randomly distributed all over the calorimeter.

Shower structure: The number of hits, the first conversion layer and the last layer of the fake showers from the $K^0 \rightarrow \pi^+\pi^-$ sample are compared with those of the showers from the $K^0 \rightarrow \pi^0\pi^0 \rightarrow 4\gamma$ decays (fig. 5.6). We clearly see, that the fake showers have on average less hits than the showers originating from the $K^0 \rightarrow \pi^0\pi^0 \rightarrow 4\gamma$ decays. Also, fake showers are less likely to reach the last layer of the calorimeter. The differences are however too small to separate the fake showers from the showers from golden $K^0 \rightarrow \pi^0\pi^0 \rightarrow 4\gamma$ events.

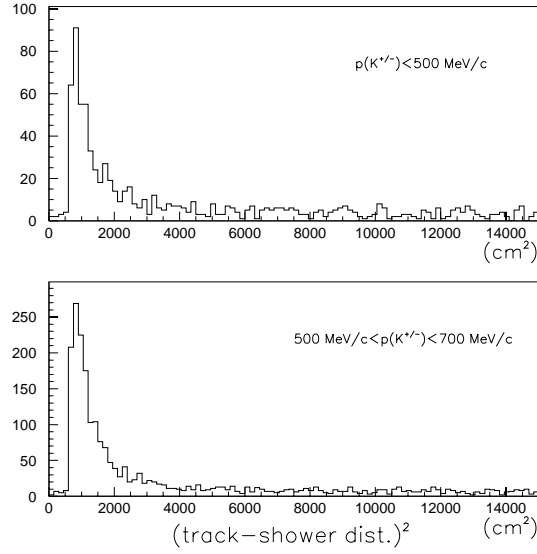


Figure 5.3: Squared distance between the K^\pm track and the closest neutral shower in $K^0 \rightarrow \pi^+\pi^-$ data for two charged kaon momentum intervals.

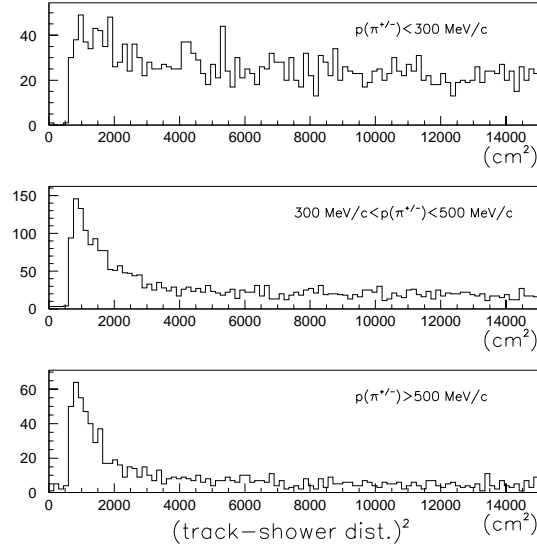


Figure 5.4: Squared distance between a π^\pm track and the closest neutral shower in $K^0 \rightarrow \pi^+\pi^-$ data for three pion momentum intervals.

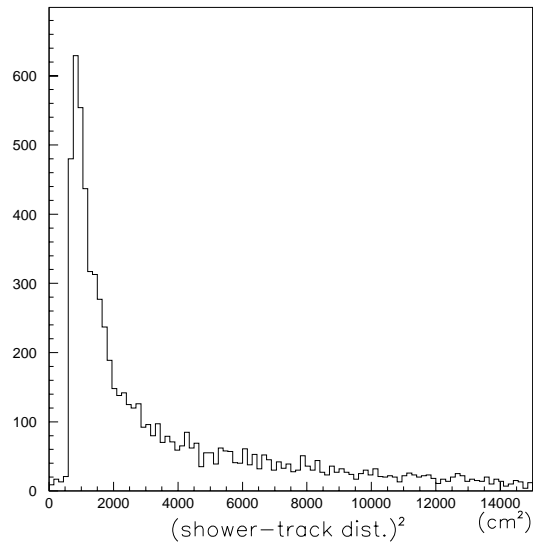


Figure 5.5: Squared distance between a neutral shower and the closest charged track in $K^0 \rightarrow \pi^+\pi^-$ data.

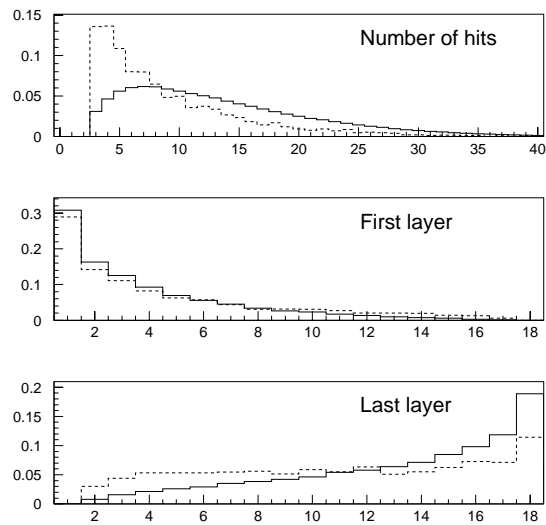


Figure 5.6: Comparison of the number of wire hits, the first and the last layer of showers originating from photons from $K^0 \rightarrow \pi^0\pi^0$ events (solid line) and fake showers found in the $K^0 \rightarrow \pi^+\pi^- \rightarrow 4\gamma$ data sample (dashed line).

Shower direction: We also check, whether the fake showers can be suppressed using the reconstructed shower direction. In general the fake showers should not point to the $p\bar{p}$ annihilation vertex. The shower direction is obtained from the hit distribution in the shower. From this distribution also the error of the shower direction is estimated separately for each event [36, 37].

For the study we use the golden $K^0 \rightarrow \pi^+\pi^-$ events as a source of fake showers and $p\bar{p} \rightarrow K^+K^-\pi^0$, $\pi^0 \rightarrow \gamma\gamma$ events in which no background showers are expected due to the selection criteria applied [38]. In the second channel the neutral showers should point to the $p\bar{p}$ annihilation vertex. In figure 5.7 the difference between the measured and the expected shower direction is shown for both the $p\bar{p} \rightarrow K^+K^-\pi^0$ and the $K^0 \rightarrow \pi^+\pi^-$ events. The difference between the measured and the estimated shower direction is divided by the estimated error. The distribution obtained for the fake showers is broader. However, the shower direction resolution is not sufficient to make a separation between the fake and the signal showers.

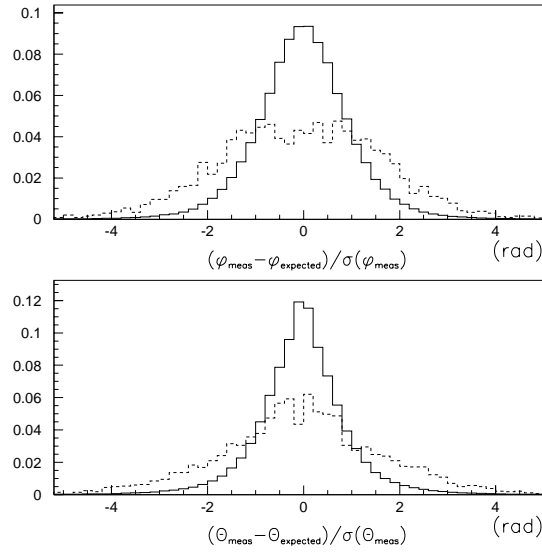


Figure 5.7: The difference of the measured shower direction and the expected direction for $p\bar{p} \rightarrow K^+K^-\pi^0$ events (solid line) and the respective distribution for fake showers from $K^0 \rightarrow \pi^+\pi^-$ events (dashed line). The difference in the shower direction is normalized to the estimated error of the shower angle. The upper plot presents the results for the plane perpendicular to the beam axis (φ is an azimuthal angle), the lower for the direction parallel to the beam (Θ is the longitudinal angle between the shower and the beam directions).

5.1.2 Difference Between K^+ and K^- Events

As shown in figure 5.2 more fake showers are grouped around K^+ than around K^- tracks. It is important how does the total number of fake showers depend on the cut-off around the K^+ and the K^- tracks.

Figure 5.8 shows the average number of fake showers per golden $K^0 \rightarrow \pi^+\pi^-$ event as a function of the cut applied on the distance between the shower conversion point and the charged kaon track. It can be seen, that up to a distance of 50 *cm* the average number of fake showers is different for K^+ and K^- events. For the cut placed on a distance greater than 50 *cm* the number of fake showers is the same for K^+ and K^- events.

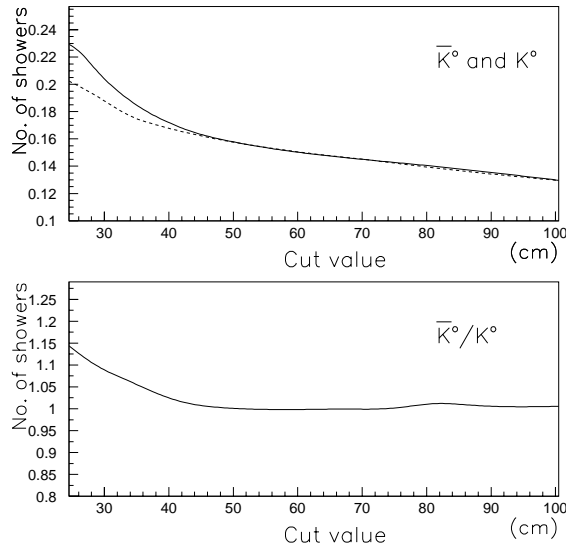


Figure 5.8: Number of neutral showers per event in $K^0 \rightarrow \pi^+\pi^-$ data as a function of the cut-off distance around the charged kaon track. The distributions are presented separately for $p\bar{p} \rightarrow K^+\pi^-\bar{K}^0$ (solid line) and $p\bar{p} \rightarrow K^-\pi^+K^0$ events (dashed line). The lower plot shows the ratio of both distributions.

5.1.3 Fake Shower Suppression

The easiest and most general way of reducing the number of fake showers is to disregard all the showers closer than 50 *cm* to the charged kaon track. They should be treated as charged showers. The cut around the pion track remains unchanged, i.e. 25 *cm*. The greater cut-off distance around the kaon track reduces the number of the fake showers in the $K^0 \rightarrow \pi^+\pi^-$ data from 0.22 neutral showers per event to 0.16.

5.2 Comparison of Simulated and Real Fake Showers

Figure 5.9 shows the comparison of the distance between a track of a charged particle and the closest neutral shower in the $K^0 \rightarrow \pi^+\pi^-$ data and in the simulated events from this channel. The applied cuts are the same as used for selecting the golden $K^0 \rightarrow \pi^+\pi^-$ events. The Monte Carlo simulation slightly overestimates the number of showers grouped around the charged pion track and underestimates the number of showers around the kaon track.

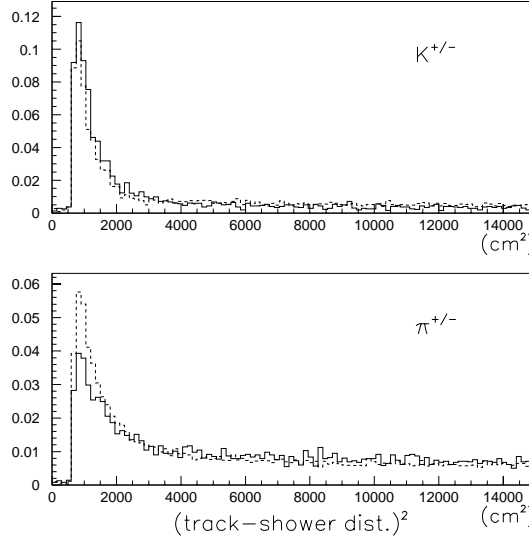


Figure 5.9: Comparison of the squared distance between a charged track and the closest neutral shower for both $K^0 \rightarrow \pi^+\pi^-$ data (solid line) and Monte Carlo simulation (dashed line).

The shower structures for real and simulated showers are also compared (fig. 5.10). The number of hits in a fake shower is well reproduced by the Monte Carlo simulation. There is some discrepancy in the conversion layer and the last layer of a shower.

Table 5.1 shows the comparison of the number of fake showers found in the $K^0 \rightarrow \pi^+\pi^-$ data and in the Monte Carlo simulation while using the 25 cm and the 50 cm cut-off distance around the charged kaon track.

After changing the neutral shower selection criteria according to the new 50 cm cut we obtain a good agreement in the total number of fake showers between the $K^0 \rightarrow \pi^+\pi^-$ Monte Carlo simulation and the data.

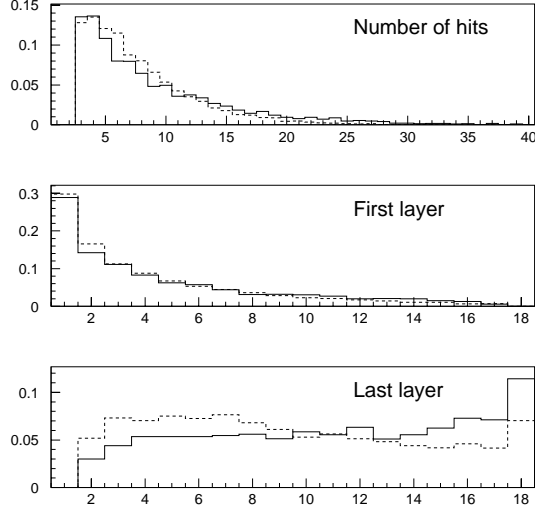


Figure 5.10: Comparison of the number of hits, the first and the last layer of fake showers originating from $K^0 \rightarrow \pi^+\pi^-$ data events (solid line) and Monte Carlo simulation (dashed line).

	No. of fake showers per event	
	$K^0 \rightarrow \pi^+\pi^-$ data	$K^0 \rightarrow \pi^+\pi^-$ MC
25 cm cut	0.215 ± 0.003	0.178 ± 0.002
50 cm cut	0.155 ± 0.002	0.153 ± 0.002

Table 5.1: Number of fake showers per event in golden $K^0 \rightarrow \pi^+\pi^-$ events in real and simulated data as a function of the applied cut.

5.3 Conclusions

The fake showers detected in the calorimeter are correlated with the passage of charged particles through the calorimeter and form a halo around the particle track. They originate from secondary interactions of particles in the massive parts of detector and also from charged kaon decays. The fake showers found far away from any charged track are generated by the photons originating from the above reactions which traverse the whole detector and create a neutral shower on the opposite side of the calorimeter.

This is proven by the analysis using e^+e^- pairs originating from photon conversions (sec. 6.4.3). The use of converted photons provides a better resolution of the photon flight direction than the showers detected in the calorimeter and therefore allows to find, that the fake photons originate from the points, where the charged particles are traversing the massive detector parts.

The extended 50 *cm* cut around a charged kaon track reduces the number of fake showers in the $K^0 \rightarrow \pi^+\pi^-$ data by 27%.

The CPLEAR Monte Carlo simulation reproduces well the total number of the fake showers and the number of hits in these showers. It is an important tool to estimate the level of background originating from the fake showers.

Chapter 6

Observation of CP Violation in $K^0 \rightarrow \pi^0\pi^0$ Decays

The aim of the analysis of neutral kaon decays into two neutral pions is the observation of the lifetime dependent asymmetry between the initially pure K^0 and \overline{K}^0 states (sec. 3.3). The neutral kaon decay vertex is reconstructed using e^+e^- pairs originating from the π^0 Dalitz decays ($\pi^0 \rightarrow e^+e^-\gamma$, see appendix A) or from the photon conversion inside the tracking devices (see appendix B). The tracks of the electron and positron are detected by the tracking chambers and the neutral kaon vertex is found as a crossing point of the reconstructed flight directions of the photon and the neutral kaon (fig. 6.1).

This method of K^0 decay vertex reconstruction is complementary to the standard CPLEAR approach in which four photons detected in the electromagnetic calorimeter are used and allow a full reconstruction of the neutral particle cascade $K^0 \rightarrow \pi^0\pi^0 \rightarrow 4\gamma$ including the reconstruction of the invisible neutral kaon decay vertex [4]. The use of e^+e^- tracks to reconstruct the K^0 decay vertex gives a better resolution than the standard method.

The method of neutral kaon vertex reconstruction using e^+e^- pairs was not foreseen in the design of the CPLEAR experimental setup [3] and therefore no dedicated converter was installed. In addition the detector is designed with as little material as possible in order to minimize neutral kaon regeneration effects and multiple scattering.

6.1 Selection of the $K^0 \rightarrow \pi^0\pi^0$ Events

6.1.1 Prefiltering

From the collected events with four reconstructed particle tracks the candidates for the signal events are selected. The kaon is recognized as a particle giving a signal in both inner and outer scintillator but producing no light in the Čerenkov counter. The kaon candidate must have a momentum greater than $300 \text{ MeV}/c$ in order to reject slow pions which can give also an $S\overline{C}S$ signature. The kaon track must have at least one hit in the proportional chambers to ensure that it originates from the $p\overline{p}$ annihilation.

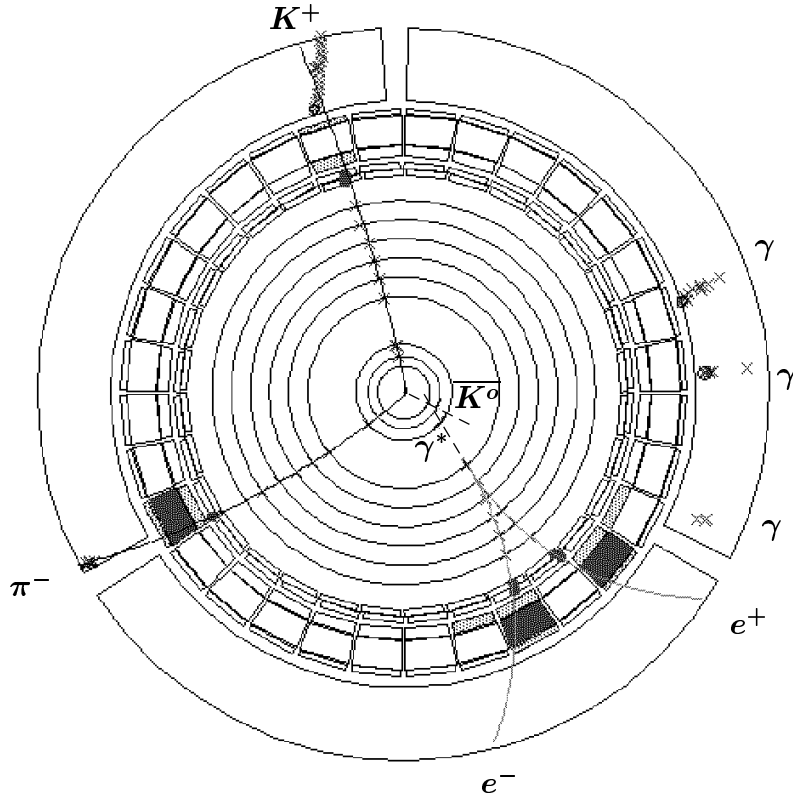


Figure 6.1: A $K^0 \rightarrow \pi^0 \pi^0$ event. The neutral kaon decay vertex is found as the crossing point of the reconstructed flight directions of the photon (γ^*) and the neutral kaon.

The e^+e^- pair originating from photon conversion or π^0 Dalitz decay is recognized by the small opening angle. Therefore, two tracks of oppositely charged particles are required to have an opening angle smaller than 18° . None of them is allowed to be a kaon candidate. These two particles are recognized as e^+e^- candidates from this point onwards.

6.1.2 Selection

In the next step of the event selection additional criteria are applied to improve the data quality.

General Quality Cuts

The selected events must fulfil the following general quality criteria:

- The total charge of the four particles must be zero.
- Any two tracks must not share the $S1$ hit in the same sector. Since the energy loss in this scintillator is used to identify particles, this information would be incorrect

if more than one charged track had passed through the same scintillator.

- The primary vertex formed by the two tracks should be within the antiproton annihilation region inside the target. The primary vertex must be inside a cylinder of radius 2 cm (transverse plane) and ± 6 cm length (parallel to detector axis).

1C-fit to the Primaries

The neutral kaon momentum is reconstructed as the missing momentum of the primary charged kaon and pion. In order to improve the momentum information of the neutral kaon and to select the golden events, a constrained fit is applied (for a general description of the constrained fits see appendix C).

This constrained fit is carried out with the hypothesis, that the primary tracks are a charged kaon and a charged pion and the only missing particle is a neutral kaon. The six measured quantities are the momentum components of the two charged particles. The three unknowns are the momentum components of the neutral kaon. Four constraints are obtained from momentum and energy conservation. This leads to a fit with one constraint.

The fit selects the golden events, while suppressing other channels, especially the channel, where an extra neutral pion is produced at the annihilation vertex ("golden+ π^0 "). Figure 6.2 shows the distribution of the 1C-fit probability for the simulated golden channel, for the simulated golden+ π^0 events and for data events. All the cuts described up to now are applied. Only events with a probability higher than 10% are accepted. This cut removes 90% of golden+ π^0 background events and only 12% of the signal events. The 1C-fit probability spectrum obtained for data shows a high background contribution.

Selection of the e^+e^- Pair

We apply stronger kinematical cuts to select e^+e^- pairs. First we require, that the electron-positron opening angle θ fulfills the criterion $\cos \theta > 0.96$ (fig. 6.3). Then we apply an additional cut on the reconstructed invariant mass of the two particles (fig. 6.4). The events with an invariant mass below 40 MeV/c^2 are accepted. We note that both distributions are similar for the converted photons and for the Dalitz decays.

Neutral Showers

Neutral showers are reconstructed using the procedure described in section 4.4. In order to have a proper energy measurement we require, that two showers must not share the same wire projection. Overlapping clusters in the strip projections are accepted. We require also, that the neutral shower is further than 50 cm from an extrapolation of the charged kaon track to the calorimeter. This criterion reduces the number of fake showers as discussed in section 5.1.3.

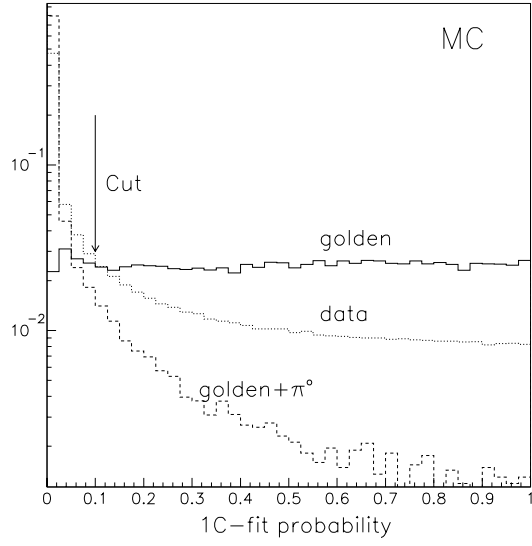


Figure 6.2: Probability distribution of the 1C-fit for simulated golden events, for the events with an additional π^0 produced at the primary vertex and for the data events. The prefiltering and the general quality cuts are applied.

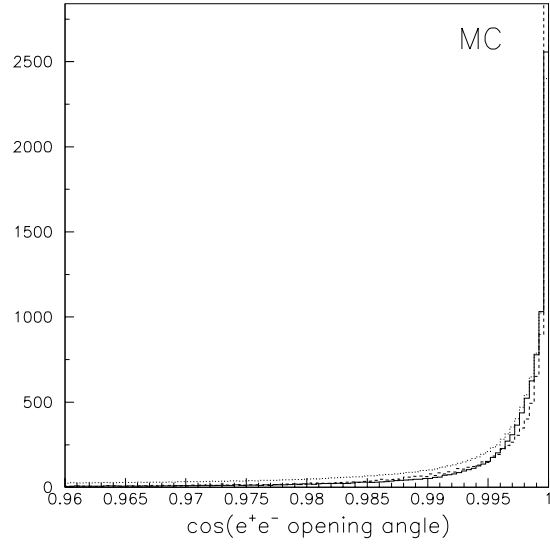


Figure 6.3: Cosine of the reconstructed e^+e^- opening angle for simulated events with a Dalitz decay of a neutral pion (solid line) and a photon conversion (dashed line). The dotted line represents the data after prefiltering and general quality cuts.

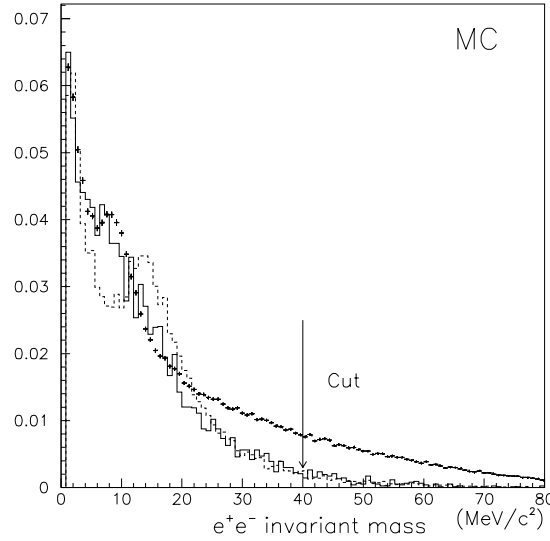


Figure 6.4: e^+e^- invariant mass for the simulated events with a π^0 Dalitz decay (solid line) and photon conversion (dashed line). Crosses represent the data points after all the cuts described up to now.

The multiplicity of the neutral showers found in the data events is shown in fig. 6.5. The exclusive event reconstruction would restrict our analysis to the events with three neutral showers. This would strongly reduce our data sample and make the observation of CP violation almost impossible. Therefore in the further analysis we accept all events with a maximum of three neutral showers. The photons detected in the calorimeter are later used for background suppression (sec. 6.4.4).

6.2 Reconstruction of the Neutral Kaon Lifetime

The neutral kaon lifetime is reconstructed using the tracks of the charged particles at the primary (annihilation) and secondary (e^+e^-) vertex. We introduce a coordinate system with a Z -axis parallel to the beam. The X -axis and the Y -axis define a plane perpendicular to the beam.

6.2.1 Vertex Reconstruction

Annihilation Vertex

The primary vertex formed by the charged kaon and pion tracks is reconstructed using a standard CPLEAR vertex finding algorithm [33]. On the $X - Y$ plane it determines a vertex as a crossing point of two tracks. If the tracks do not intersect the point of

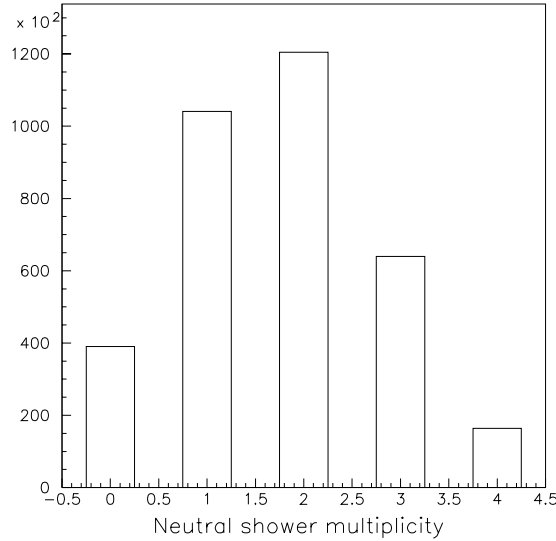


Figure 6.5: Neutral shower multiplicity in the data events. All the cuts described up to now are applied

the closest approach is chosen as vertex. The Z -component of the vertex coordinate is calculated as an average of the Z -components of the two tracks at the point of the closest approach.

The K^0 momentum is found as the missing momentum of the two primary particles K^\pm and π^\mp . The K^0 momentum resolution is improved by applying the $K^\pm \pi^\mp$ missing mass constrained fit (sec. 6.1.2).

e^+e^- Vertex

The electron-positron pair (e^+e^-) originating from a Dalitz decay or from a photon conversion in the detector material has small opening angle. The standard CPLEAR vertex finding algorithm [33] finds a vertex as the crossing point of two tracks or as the point of closest approach. For small opening angles this method is not sufficiently precise and the development of a dedicated algorithm is necessary [39]. Here we give only a short overview of the vertex reconstruction method. A detailed description and the formulas are given in appendix D.

In the $X - Y$ plane the e^+e^- vertex is reconstructed as a point laying on the line connecting the centers of two circles formed by the track projections to the $X - Y$ plane. The distance between the vertex and the center of each circle is proportional to the circle radius (fig. 6.6). The Z component is determined as the average of the Z coordinates of both tracks at the points of the closest approach to the vertex.

This method of vertex reconstruction gives better results in finding the e^+e^- vertex

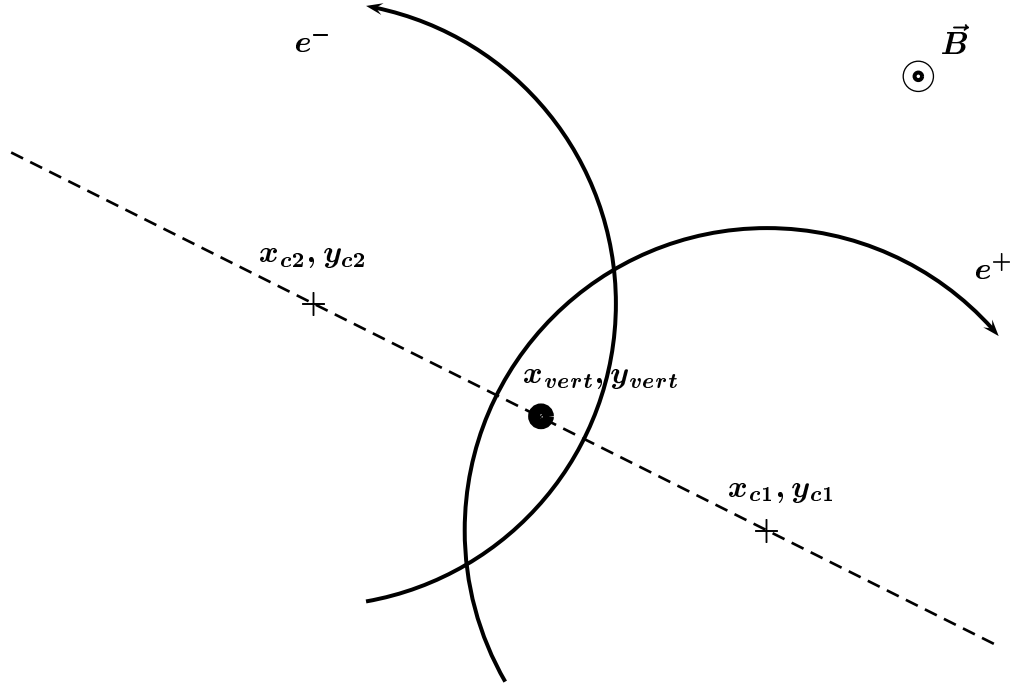


Figure 6.6: Reconstruction of the e^+e^- vertex. It is found as a point laying on the line connecting the centers of two circles formed by the track projections to the $X-Y$ plane. The distance between the vertex and the center of each circle is proportional to the circle radius.

than the standard CPLEAR method as found by the Monte Carlo simulation (fig. 6.7). The resolution in $R = \sqrt{X^2 + Y^2}$ is improved from 2.30 cm to 1.33 cm (RMS) and in contrast to the standard method the shape of the resolution distribution $R_{meas} - R_{true}$ becomes symmetric. Resolution in the azimuthal angle $\varphi = \arctan(Y/X)$ is also improved from 0.17 rad to 0.12 rad (RMS).

K^0 Decay Vertex and Lifetime

The K^0 decay vertex is found on the $X-Y$ plane as the intersection point of the K^0 flight direction and the e^+e^- pair momentum direction (fig. 6.8). The K^0 decay length is given by the distance between the primary vertex and the neutral kaon decay vertex. The neutral kaon lifetime is calculated using the transverse projection of the decay length s and the K^0 transverse momentum p_T obtained from the 1C-fit (sec. 6.1.2).

$$\tau = \frac{m(K^0) \cdot s}{p_T} \quad (6.1)$$

The momentum and vertex resolution in Z -direction is worse than in the transverse plane, therefore the transverse projections of the particle momenta and of the vertices are used in the lifetime reconstruction.

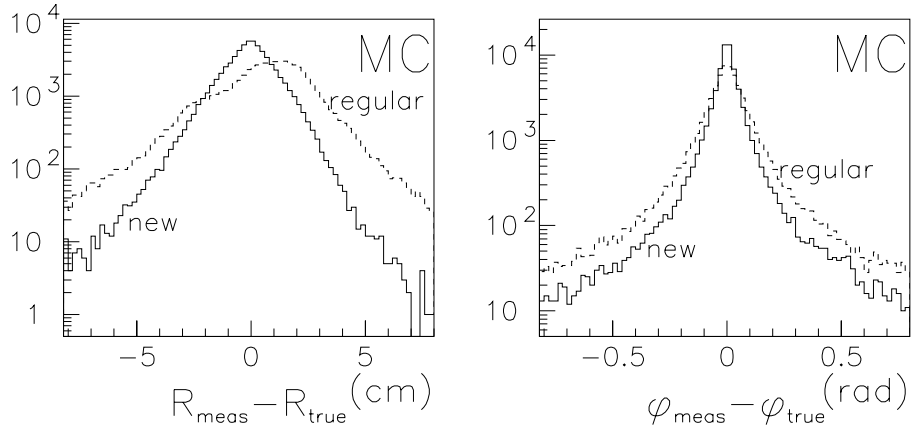


Figure 6.7: The difference between the reconstructed and true e^+e^- vertex in $R = \sqrt{X^2 + Y^2}$ (left plot) and in $\varphi = \arctan(Y/X)$ (right plot) for simulated events. Our vertex reconstruction method ("new") is compared with the standard one ("regular").

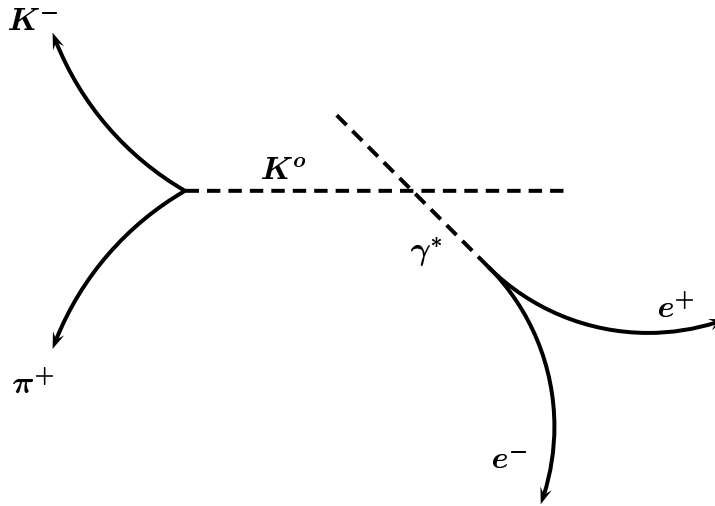


Figure 6.8: K^0 decay vertex reconstruction as an intersection point of K^0 and γ^* flight paths.

6.2.2 Lifetime Resolution

In order to select only events with a good lifetime resolution an estimation of the lifetime uncertainty is performed on an event by event basis. We improve the lifetime resolution by selecting the events with a small estimated uncertainty.

From the standard CPLEAR track fitting procedure the covariance matrix of all the track parameters is obtained (appendix D). By following the standard error propagation [40] we obtain the error of the reconstructed lifetime.

The standard CPLEAR track fitting procedure gives five helix parameters together with a covariance matrix for every track. In the first step of the error propagation the covariance matrix (6×6 matrix) of both the e^+e^- vertex and the converted photon momentum is calculated. Due to the complexity of the formulas needed, the *Mathematica* program [41] was used to calculate the derivatives. This program can handle complicated algebraic computations and is very useful in calculating the Jacobi matrices used in the error propagation.

The covariance matrix of the $p\bar{p}$ annihilation vertex is obtained from the standard CPLEAR vertex reconstruction program. The neutral kaon momentum together with its covariance matrix is obtained from the 1C-fit (sec. 6.1.2). The correlation between the primary vertex position and the K^0 momentum is found to be small and is neglected in the error calculation.

The (3×3) covariance matrix of the neutral kaon decay vertex is calculated. Having both the production and the decay vertices of the neutral kaon we obtain its path length and its lifetime (see formula 6.1). Using error propagation we finally estimate the error of the neutral kaon lifetime.

The accuracy of the error estimation can be checked using simulated events for which we know the true and the reconstructed K^0 lifetime. If the lifetime error σ is estimated correctly the distribution of $(\tau_{measured} - \tau_{true})/\sigma$ should have a Gaussian shape with a RMS width equal to one. Such a distribution is called a "pull-plot". The pull-plot for the estimated K^0 lifetime is presented in fig. 6.9. The RMS width of the distribution is close to one. The deviation from the Gaussian shape comes from the inaccuracy of the input covariance matrices and the accumulation of small errors due to the multiple error propagation and non-linear expressions.

In order to improve the lifetime resolution we require, that the estimated lifetime uncertainty is smaller than $1.5 \tau_S$. The lifetime resolution distribution $(\tau_{measured} - \tau_{true})$ obtained from the simulated data for both π^0 Dalitz decays and photon conversion is presented in figures 6.10 and 6.11. The figures show the effect of the cut on the estimated lifetime error.

The lifetime resolution depends on the K^0 lifetime. It varies from $0.38 \tau_S$ (RMS) ($0.2 \tau_S$ FWHM) for events with a true lifetime below $3 \tau_S$ to $1.21 \tau_S$ (RMS) ($0.7 \tau_S$ FWHM) for the long lifetime events of Dalitz decays. The lifetime resolution becomes worse for long true lifetimes, since for these events the e^+e^- vertex is further away from the detector center than for the events with a short lifetime. The reconstructed tracks are shorter and this results in a worse momentum resolution of the electron and

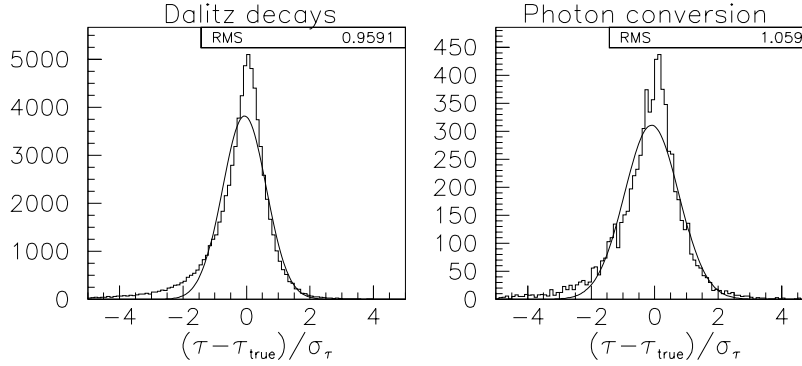


Figure 6.9: The pull-plots showing the quality of the estimated lifetime error for the simulated events with Dalitz decays (left plot) and photon conversion (right plot).

the positron. This explains also why the resolution is slightly worse for the photon conversion, since for these events the e^+e^- vertex is typically further from the detector center than for the π^0 Dalitz decays.

A small asymmetry in the lifetime resolution distribution is observed at long lifetimes. The final results are corrected for this effect.

6.3 Identification of Dalitz Decays and Photon Conversions

The probability of photon conversion is proportional to the amount of detector material in terms of radiation length (X_0). Therefore the photon conversion is a process which allows us to observe the material distribution inside the detector.

Figure 6.12 shows the distribution of the e^+e^- vertices inside the detector. It shows the detector structure and is equivalent to an "X-ray photograph" of the CPLEAR detector.

There is a concentration of electron-positron vertices in the center of detector, which corresponds to Dalitz decays. Further from the center, the various parts of the detector are visible. First we see the target wall, then the walls of the proportional and drift chambers 4.3.

The distance between the reconstructed e^+e^- vertex and the K^0 decay vertex allows to distinguish between Dalitz decays and γ -conversions. Figure 6.13 shows, that in this analysis one can observe the contributions of both processes. A distinct peak at zero corresponds to Dalitz decays, while the rest of the distribution at positive distances shows the presence of photon conversions.

Comparing the distribution obtained from the real data with the one from the

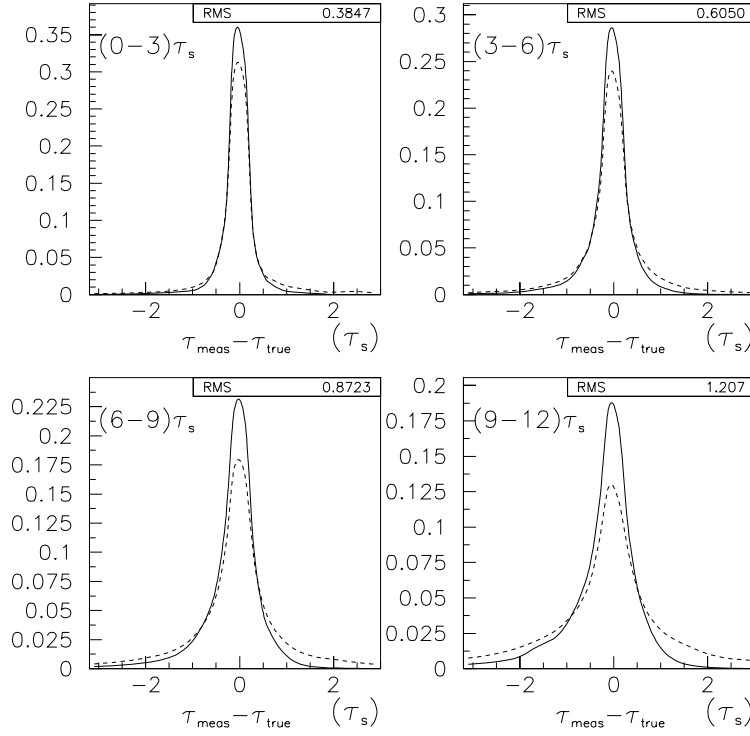


Figure 6.10: Lifetime resolution distribution ($\tau_{measured} - \tau_{true}$) for simulated events with Dalitz decays. The four plots correspond to the lifetime regions $(0 - 3) \tau_S$, $(3 - 6) \tau_S$, $(6 - 9) \tau_S$ and $(9 - 12) \tau_S$. The dashed line shows the distribution before the cut $\sigma(\tau) < 1.5 \tau_S$, the solid line after the cut.

Monte Carlo simulation we find, that in the lifetime region between $3 \tau_S$ and $4 \tau_S$ (lifetime interval shown in fig. 6.13) $\approx 34\%$ of electron-positron pairs originate from Dalitz decays while the remainder originates from γ -conversions.

6.4 Backgrounds

In the analysis of golden events with $K^0 \rightarrow \pi^0 \pi^0$ decays we identify a charged kaon and a pion and also an e^+e^- pair. We do not require the three remaining photons originating from π^0 decays to be detected in the electromagnetic calorimeter. The background identification and rejection is difficult due to the lack of constraints in the inclusive analysis.

In this section we identify various backgrounds and try to suppress them. We give an estimation of the amount of the remaining background. This estimation is used

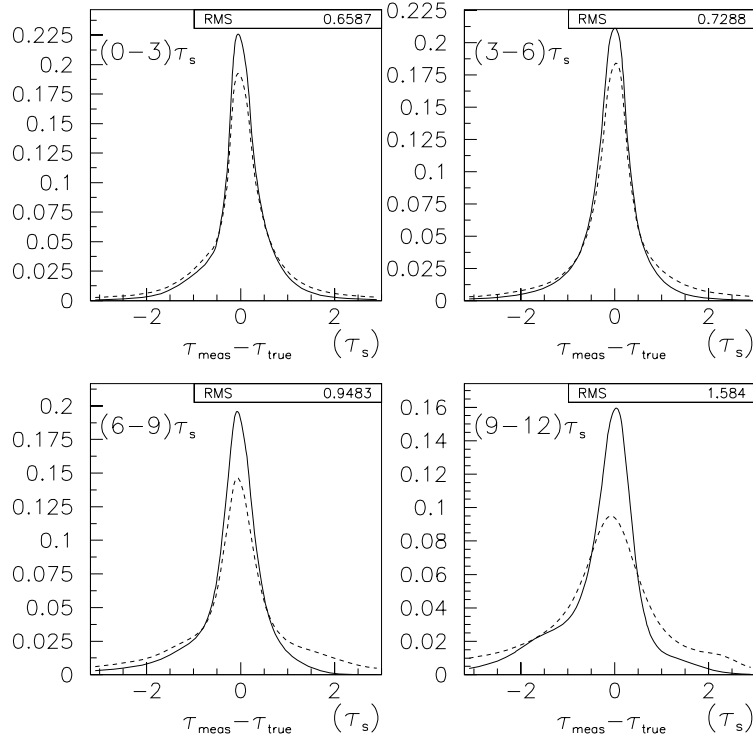


Figure 6.11: Lifetime resolution distribution $(\tau_{measured} - \tau_{true})$ for simulated events with photon conversion. The four plots correspond to the lifetime regions $(0 - 3) \tau_S$, $(3 - 6) \tau_S$, $(6 - 9) \tau_S$ and $(9 - 12) \tau_S$. The dashed line shows the distribution before the cut $\sigma(\tau) < 1.5 \tau_S$, the solid line after the cut.

later in the final analysis of the CP violation parameters. The background sources considered are:

- pionic and kaonic annihilation backgrounds ($p\bar{p} \rightarrow \pi^+ \pi^- n \pi^0$ and $p\bar{p} \rightarrow K^+ K^- n \pi^0$, $n > 0$)
- golden events with an additional π^0 produced at the $p\bar{p}$ annihilation vertex (golden+ π^0)
- fake photons converting into $e^+ e^-$ pairs in the tracking detectors.
- golden events with neutral kaon decays into final states other than $\pi^0 \pi^0$ (golden backgrounds)

The reconstructed lifetime distribution of the neutral kaons is shown in figure 6.14. We can recognize an exponential lifetime distribution of $K_S \rightarrow \pi^0 \pi^0$ decays. Back-

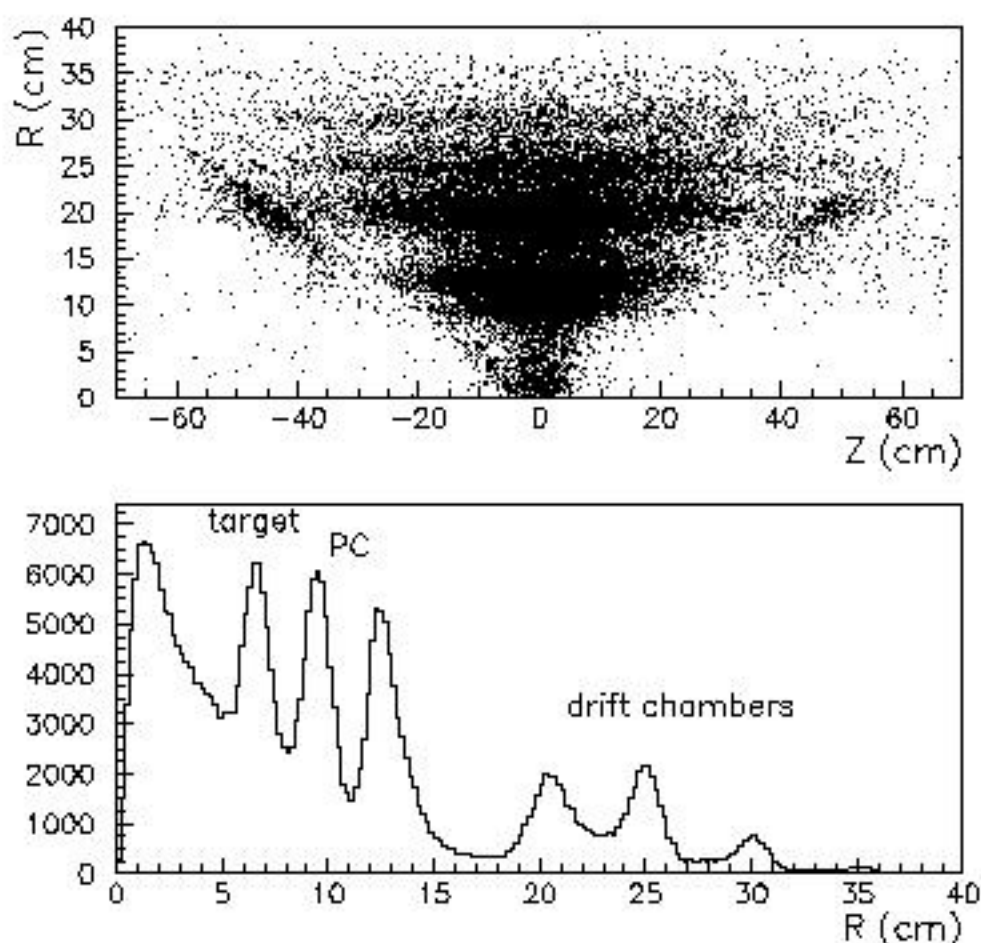


Figure 6.12: Scatter plot of the e^+e^- vertices in the $R-Z$ plane and its projection on R . We see at radius of 7 cm a signal originating from target wall. The target is followed by two walls of proportional chambers. Four first walls of the drift chambers also can be seen.

ground can be observed at long and also at negative lifetimes. A spike at $t = 0$ originates from the pionic and kaonic annihilation backgrounds.

6.4.1 Annihilation Backgrounds

In the processes $p\bar{p} \rightarrow \pi^+\pi^- \nu\pi^0$ and $p\bar{p} \rightarrow K^+K^- \nu\pi^0$ one of the primary charged particles can be misidentified. The branching ratio for the pionic background is a few hundred times higher than for the desired golden events. Therefore even a small

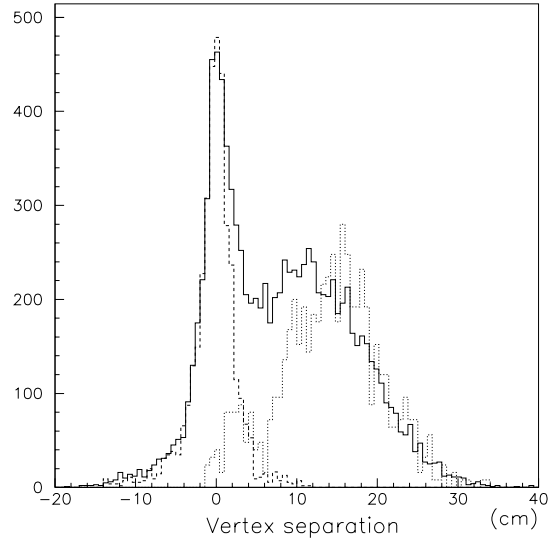


Figure 6.13: Distance between the reconstructed K^0 decay vertex and the e^+e^- vertex for the events with a reconstructed lifetime between 3 and 4 τ_S (solid line). The dashed line corresponds to simulated Dalitz decays and the dotted line to photon conversions.

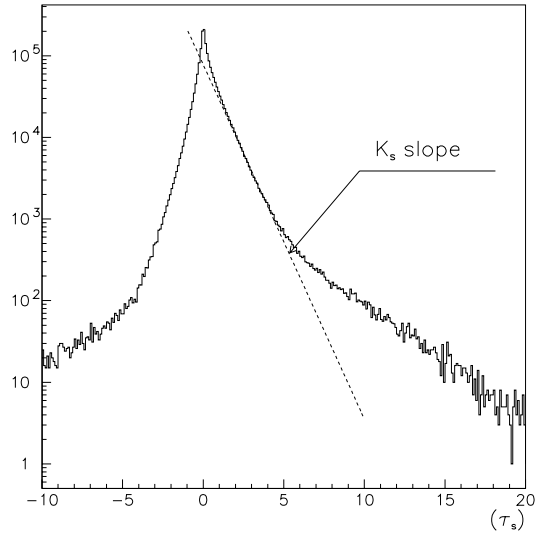


Figure 6.14: Lifetime distribution of the selected events (all the cuts described up to now are applied). An exponential lifetime distribution of $K_S \rightarrow \pi^0\pi^0$ decays can be recognized. A spike at $t = 0$ originates from the pionic and kaonic annihilation backgrounds.

probability for the particle misidentification results in the significant annihilation background.

In order to improve the primary particle selection we use as a complementary criterion the energy deposited by a particle in the inner scintillator $S1$. In order to suppress the pionic background ($p\bar{p} \rightarrow \pi^+\pi^-\pi^0$) the energy deposited by a kaon candidate is required to be greater than 2.2 MeV/cm (see fig. 4.10). The kaonic background ($p\bar{p} \rightarrow K^+K^-\pi^0$) is reduced by using the cut on the energy deposited in the inner scintillator $S1$ by the charged pion candidate. The energy loss must be lower by more than two standard deviations than the energy loss expected for the charged kaon having the same momentum.

Pionic Background

The estimation of the amount of pionic background is performed by analyzing the energy deposited by the kaon candidate in the inner scintillator. The contamination of pions is found by a fit of the dE/dx spectrum of charged kaon candidates [42]. The reference spectra for a charged kaon and a charged pion are obtained from golden events selected with the $K^0 \rightarrow \pi^+\pi^-$ decay mode where the signal is expected to be very clean [35]. Figure 6.15 shows an example of such a fit for a charged kaon momentum range between 680 and 720 MeV/c .

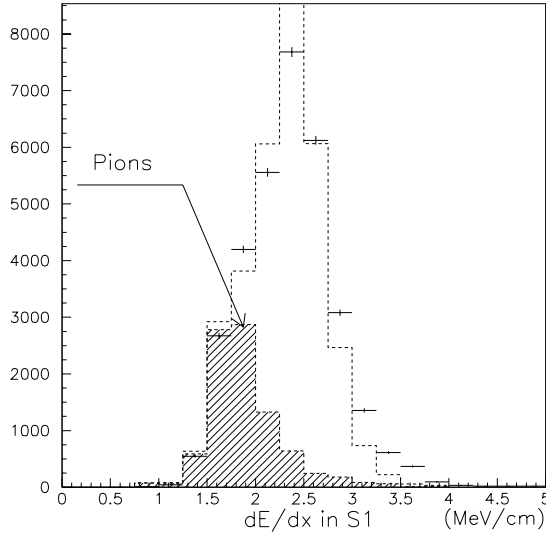


Figure 6.15: Example of a fit (dashed line) to the measured dE/dx spectrum (crosses) of the kaon candidates with momentum between 680 and 720 MeV/c . The contribution coming from pions is shown separately.

The fit is performed in each bin of neutral kaon lifetime ($1 \tau_S$ bins) and of charged

kaon momentum (40 MeV/c bins). By adding the fit results from all the momentum bins we obtain a lifetime dependence of the pionic background (fig. 6.16). As it is expected the background events have typically a short reconstructed lifetime. The background contamination estimated by the fit is approximately 4.0% of all the collected events.

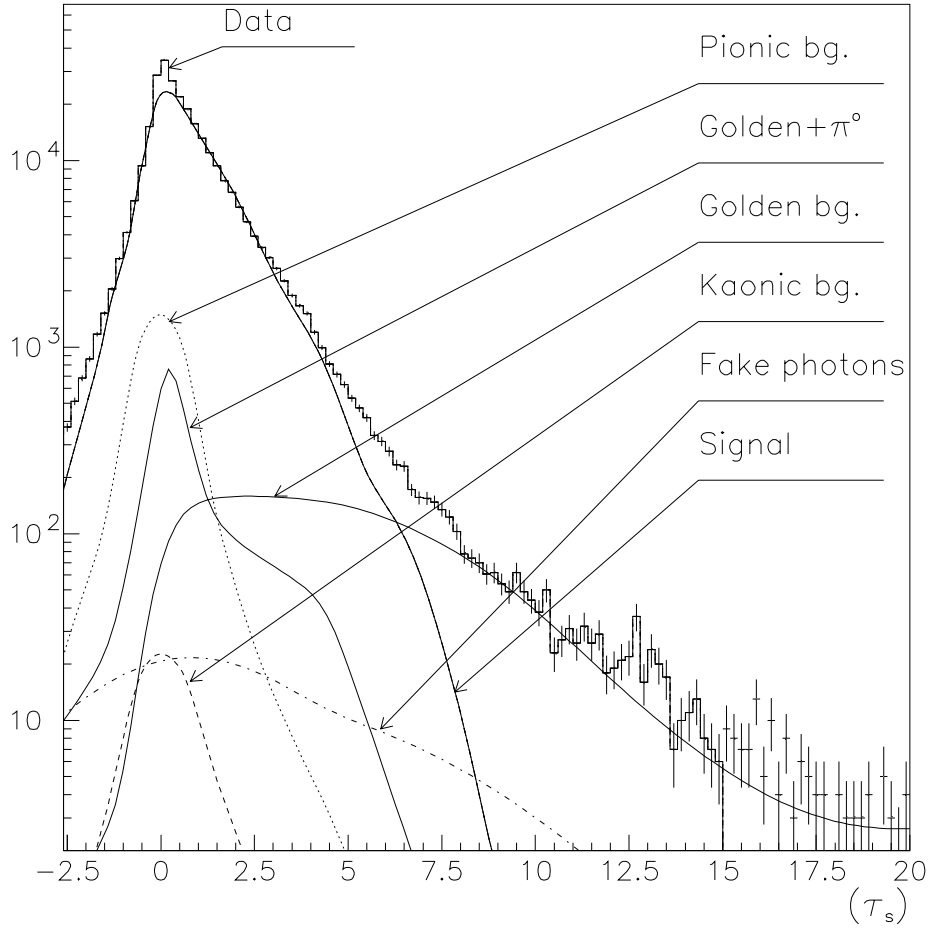


Figure 6.16: Reconstructed neutral kaon lifetime distribution with signal and background contaminations. The final analysis cuts are applied.

The method of fitting the dE/dx spectra can be applied separately to the events identified as \overline{K}^0 and K^0 events. The ratio of the backgrounds found in \overline{K}^0 and K^0 events is $\alpha_{\pi\pi} \approx 1.1$.

Kaonic Background

The method of fitting the dE/dx spectra is also used to investigate the kaonic annihilation background. From the fit we obtain the kaon contamination among the charged pion candidates. Figure 6.16 shows, that the kaonic background is much weaker than the pionic, $\approx 0.1\%$ of all events.

6.4.2 Additional π^0 s Produced at the $p\bar{p}$ Annihilation Vertex

This background contains the events, where besides a K^\pm , π^\mp and K^0 an additional π^0 is produced at the annihilation vertex. The presence of this particle causes an incorrect neutral kaon momentum reconstruction. In addition the π^0 produced at the annihilation vertex can undergo a Dalitz decay or the photon from π^0 decay can convert giving an e^+e^- pair.

The missing mass of the primary charged particles $K^\pm\pi^\mp$ is higher than for the golden events when an additional π^0 is produced. This feature is used by the 1C-fit (sec. 6.1.2). The Monte Carlo simulation shows that the golden+ π^0 background events are distributed mostly at short lifetimes (fig. 6.16).

After releasing the cut on the 1C-fit probability, which affects the $K^\pm\pi^\mp$ missing mass distribution, we can see the background contamination from golden+ π^0 events (fig. 6.17). The lifetime cut $t > 1\tau_S$ is applied in order to reduce the pionic annihilation background. For the fit of this spectrum we use the reference distributions obtained from the Monte Carlo simulation for golden and golden+ π^0 events. As result of the fit we obtain, that before the 1C-fit probability cut around 17% of all the events with a lifetime larger than $1\tau_S$ are the events with an additional π^0 . Since the 1C-fit probability cut rejects 90% of golden+ π^0 and only 12% of golden events (sec. 6.1.2) this background is reduced to 2.0% of all reconstructed events with a measured neutral kaon lifetime over $1\tau_S$. Using the simulated lifetime distributions golden+ π^0 background we find that the golden+ π^0 background contamination of all lifetimes is $\approx 1.8\%$ of all the collected events.

6.4.3 Fake Photon Background

In the study of $K^0 \rightarrow \pi^0\pi^0$ decays with the use of converted photons or π^0 Dalitz decays, fake photons converting into an e^+e^- pair are a significant background source. In this analysis the neutral kaon decay vertex (X_K, Y_K) is reconstructed on the plane perpendicular to the beam ($X - Y$ plane) (sec. 6.2.1). For the vertex point we find the Z -coordinates of the reconstructed neutral kaon Z_K and photon flight paths Z_γ . The difference $Z_K - Z_\gamma$ shows, whether the reconstructed photon originates from the K^0 decay. The difference should be small for the signal events. Figure 6.18 shows the distribution of $Z_K - Z_\gamma$ for the data events. In this plot we can see the peak at zero corresponding to the signal events and a broader distribution underneath. It corresponds to fake photons not originating from K^0 decay.

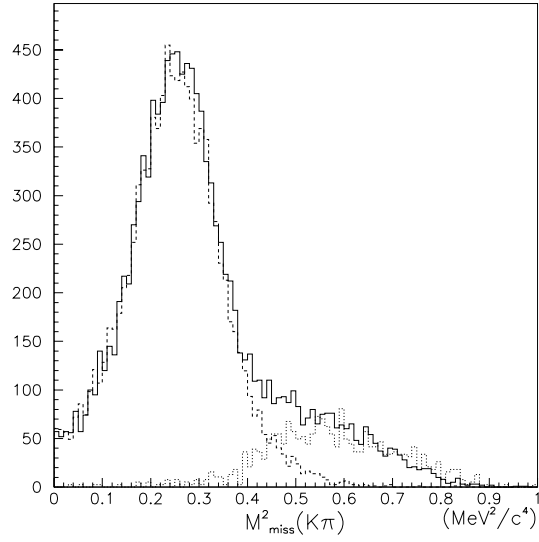


Figure 6.17: The measured distribution of the squared $K^\pm \pi^\mp$ missing mass for the events with a reconstructed K^0 lifetime greater than $1 \tau_S$. The distribution is compared with the respective distribution for the simulated golden (dashed line) and for the simulated golden+ π^0 events (dotted line). The 10% 1C-fit probability cut is not applied because it affects the missing mass spectrum.

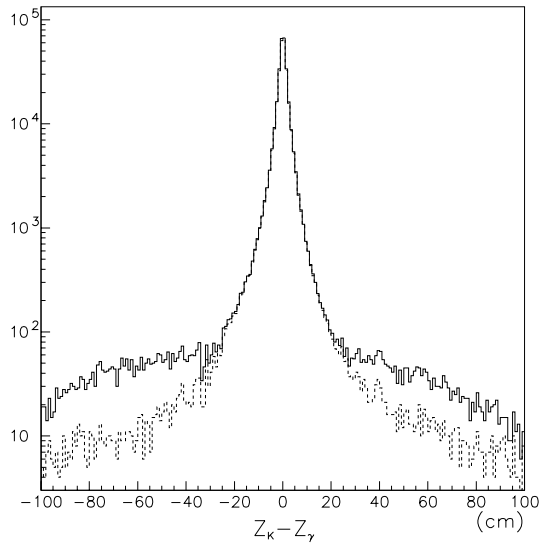


Figure 6.18: $Z_K - Z_\gamma$ distribution before the cut reducing the fake showers (solid line) and after applying the cut (dashed line).

For the further study of fake photons converting into e^+e^- pairs we can select a sample of fake photons by asking for $|Z_K - Z_\gamma| > 20 \text{ cm}$. In order to check whether the fake photons originate from secondary interactions of charged particles in the calorimeter we measure how close the photon approaches the track of the charged particle. In figure 6.19 the distance between the selected fake photons and the particle tracks is shown. The distance is measured at the radius corresponding to the first calorimeter layer ($r = 77 \text{ cm}$). We see, that for most of the selected fake photons the distance is smaller than for the photons originating from K^0 decays ($|Z_K - Z_\gamma| < 20 \text{ cm}$). We conclude, that the fake photons originate from strong interactions of charged particles in the massive parts of the detector, namely the PIDs, the calorimeter and the magnet. Also the decays of charged kaons can be a source of fake photons.

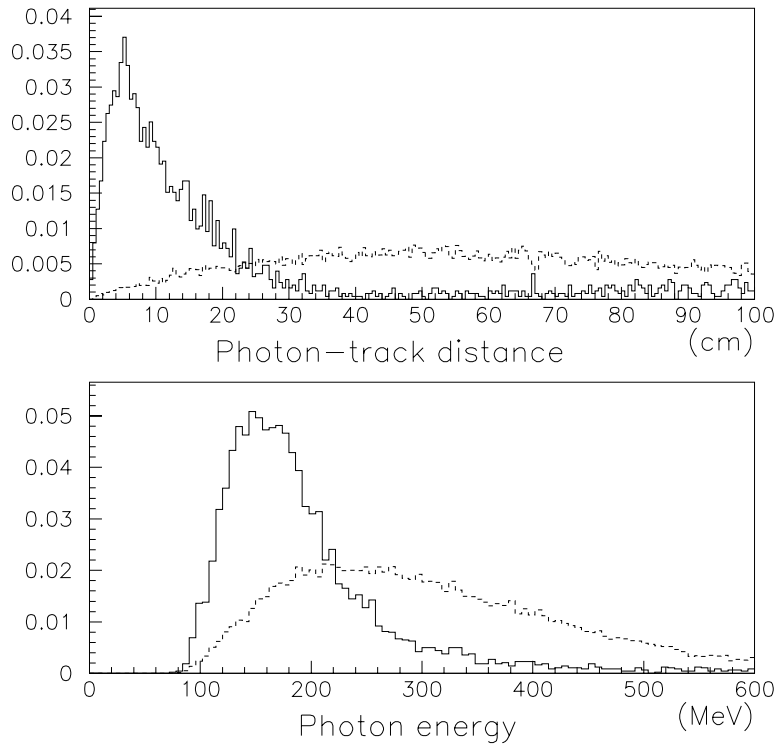


Figure 6.19: In the upper plot the distance between a fake photon ($|Z_K - Z_\gamma| > 20 \text{ cm}$) and a charged particle (solid line) at 77 cm radius is compared with the respective distribution obtained for a photon originating from K^0 decay ($|Z_K - Z_\gamma| < 20 \text{ cm}$, dashed line). In the lower plot the fake photon energy distribution (solid line) is compared with the signal photon energy spectrum (dashed line).

In the same figure 6.19 the energy distribution of the fake photons is compared with the energy distribution of the photons originating from the K^0 decays. The energy of

the fake photons is typically lower. Therefore the fake photons converting into e^+e^- pairs can be suppressed by a combined cut using the photon energy and the distance between the photon flight path and the closest charged track. We reject the photons with both $E_\gamma < 300 \text{ MeV}$ and $d_{\gamma\text{-track}} < 30 \text{ cm}$.

The effect of this cut can be observed on the $Z_K - Z_\gamma$ distribution (fig. 6.18). After the cut $\approx 80\%$ of the events with large $|Z_K - Z_\gamma|$ are rejected. From the same distribution we estimate the amount of the fake photon background. After applying the cut, there are ≤ 1000 remaining events with fake photons ($\leq 0.4\%$ of all events).

In order to observe a lifetime distribution of events with the fake photons we select a sample of the background events by applying the strong cuts selecting the events with fake photons. We require the converted photon energy to be below 300 MeV and the distance to the charged track to be smaller than 15 cm . In addition we ask for $|Z_K - Z_\gamma| > 40 \text{ cm}$. The obtained lifetime distribution is shown in figure 6.16.

Using the same sample of selected events with fake photons we measure the ratio α_{fake} of events with a reconstructed \bar{K}^0 to the events with a reconstructed K^0 and we obtain $\alpha_{fake} \approx 1.4$. As we will see later, this value differs from the normalization of the signal events and therefore the presence of the fake photons can mimic CP violation effects.

6.4.4 K^0 Decays into Final States other than $\pi^0 \pi^0$

The other type of background sources are golden events with a neutral kaon decaying into other final states than two neutral pions. The decays considered are $K^0 \rightarrow \pi^+ \pi^-$, $K^0 \rightarrow \pi^+ \pi^- \pi^0$, $K^0 \rightarrow \pi^0 \pi^0 \pi^0$ and the semileptonic decays $K^0 \rightarrow \pi l \nu$. The other decay modes of a neutral kaon have small branching ratios and can be neglected.

$$K^0 \rightarrow \pi^+ \pi^-$$

The kinematics of this decay puts a limit on the opening angle between the charged pions originating from the neutral kaon decay. For the neutral kaons momenta below $750 \text{ MeV}/c$ the $\pi^+ \pi^-$ opening angle is greater than $\approx 65^\circ$. Therefore $K^0 \rightarrow \pi^+ \pi^-$ events should be rejected by the selection criterion used in this analysis $\cos \Theta > 0.96$. However, when the primary pion is misidentified as a secondary one, the opening angle between the pion and the oppositely charged secondary pion can be arbitrary small (fig. 6.20).

This type of background can be observed in the invariant mass distribution of the primary pion and the oppositely charged secondary particle. Figure 6.21 presents a distribution of the invariant mass obtained in this way for events where at least one of the tracks of the secondary particles has hits in the first layer of proportional chambers. A distinct peak around $500 \text{ MeV}/c$ corresponds to the neutral kaon mass. This peak disappears for the events with no hits in $PC1$.

The $K^0 \rightarrow \pi^+ \pi^-$ background is highly suppressed by the requirement that the secondary particle tracks have no hits in the first layer of the proportional chambers

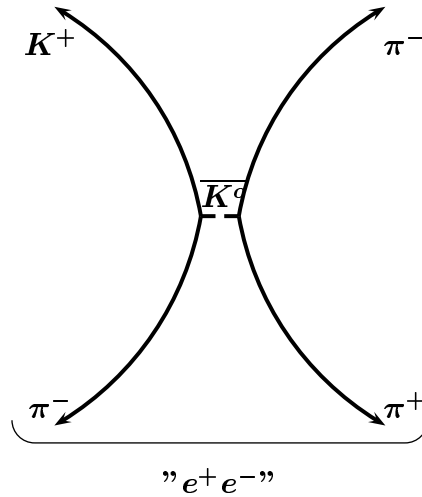


Figure 6.20: $K^0 \rightarrow \pi^+ \pi^-$ background. When the primary pion is misidentified as a secondary one, the opening angle between the pion and the oppositely charged secondary pion can be arbitrary small.

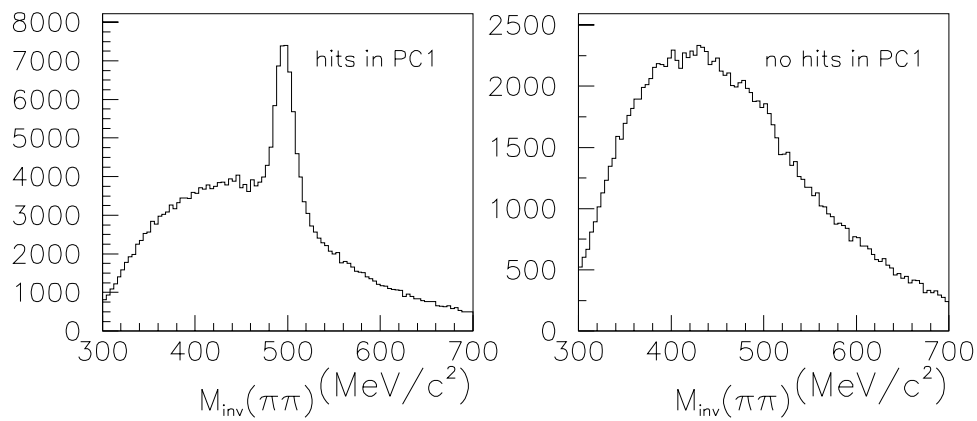


Figure 6.21: $\pi^+\pi^-$ invariant mass of "secondary particles". A peak at the K^0 mass is a sign of the golden $K^0 \rightarrow \pi^+\pi^-$ background which is visible for the events with at least one secondary track having hits in PC1 (left plot). The right plot corresponds to the events, where e^+e^- candidates have no hits in the PC1.

($PC1$). This ensures a good separation between the primary and secondary particles. However, this cut strongly suppresses events with π^0 Dalitz decays with a lifetime below $3 \tau_S$ (fig 6.25).

$$K^0 \rightarrow \pi^0 \pi^0 \pi^0$$

After the neutral kaon decay into three neutral pions, one of the pions can undergo a Dalitz decay or one of the produced photons can convert into an e^+e^- pair. Such a process can be easily misidentified as a $K^0 \rightarrow \pi^0 \pi^0$ decay, because in most of the cases some of the additional photons remain undetected in the calorimeter.

Photons originating from the decay $K^0 \rightarrow \pi^0 \pi^0 \rightarrow 4\gamma$ have on average higher energy than the photons from the $K^0 \rightarrow \pi^0 \pi^0 \pi^0 \rightarrow 6\gamma$ decay. In figure 6.22 the energies of the converted photon in the K^0 rest frame are shown for both simulated channels and for data. The selection cut accepts photons with an energy higher than 120 MeV.

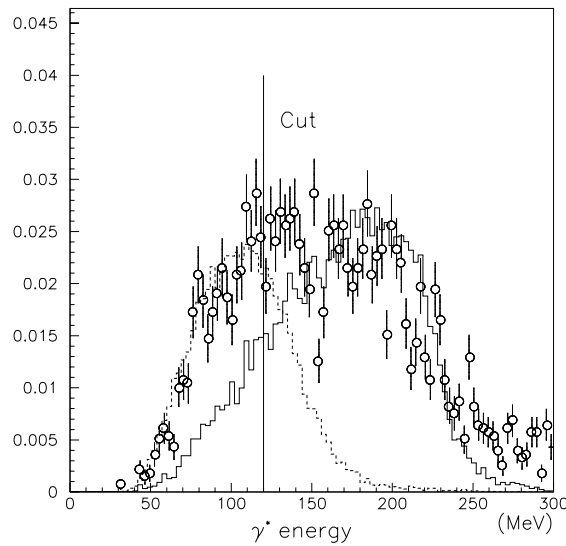


Figure 6.22: Energy distribution of the reconstructed photons in the K^0 rest frame for the simulated K^0 decays into two (solid line) and three (dashed line) neutral pions. Circles represent the data point (events with lifetime $> 5 \tau_S$ are used).

For the events where besides the electron-positron pair three additional photons are detected in the calorimeter it is possible to apply a constrained fit to the $p\bar{p} \rightarrow K^\mp \pi^\pm K^0(\bar{K}^0)$, $K^0 \rightarrow \pi^0 \pi^0 \rightarrow 4\gamma$ hypothesis (for a general introduction to constrained fits see appendix C). The energies and impact points of the neutral showers are used to improve the separation of signal and background. The constraints are momentum and energy conservation, the K^0 mass and two neutral pion masses (compare with the fit described in section 7.1.2). In addition, the neutral kaon decay length is fixed to

the one found from the K^0 decay vertex reconstruction (7C-fit). The probability of this fit is a measure whether a given event fulfills the $K^0 \rightarrow \pi^0\pi^0$ hypothesis. The distribution of the fit probability is shown in figure 6.23 for the simulated $K^0 \rightarrow \pi^0\pi^0$ and $K^0 \rightarrow \pi^0\pi^0\pi^0$ decays and also for data events.

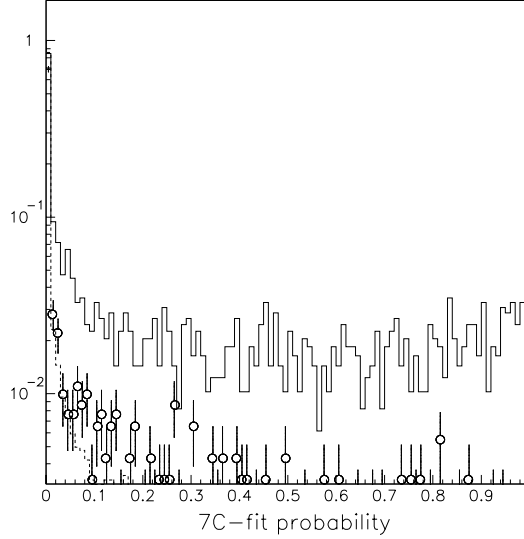


Figure 6.23: The 7C-fit probability distribution for the simulated $K^0 \rightarrow \pi^0\pi^0$ events (solid line) and $K^0 \rightarrow \pi^0\pi^0\pi^0$ (dashed line). Circles represent the data point (events with lifetime $> 5 \tau_S$ are used).

The selection criteria chosen to suppress the $K^0 \rightarrow \pi^0\pi^0\pi^0$ background are the following:

- for events with less than three neutral showers the converted photon energy in the K^0 rest frame must be higher than 120 MeV
- for events with three neutral showers the probability of the 7C-fit must be greater than 1% or the converted photon energy must be greater than 140 MeV.

According to the Monte Carlo simulation the cut described above removes 74% of the $K^0 \rightarrow \pi^0\pi^0\pi^0$ events. At the same time only 16% of signal events are rejected.

$K^0 \rightarrow \pi e \nu$ and $K^0 \rightarrow \pi \mu \nu$

The semileptonic decays of neutral kaons are also a source of background. A charged pion can be misidentified as an electron or positron. The shape of the lifetime distribution of the simulated semileptonic background is shown in figure 6.24 together with other simulated background channels.

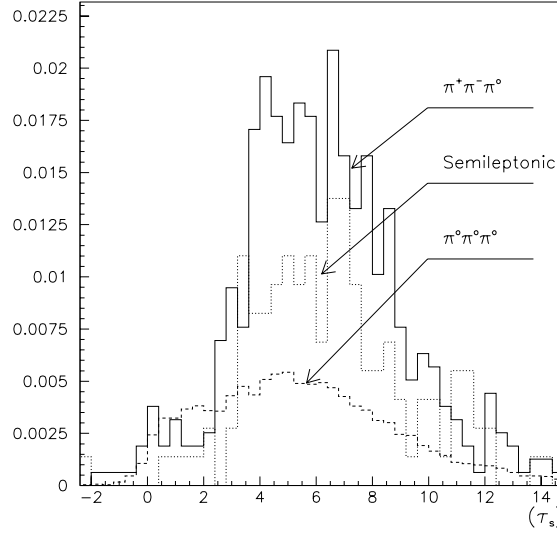


Figure 6.24: Lifetime distributions obtained from the Monte Carlo simulation for the golden background channels.

$$K^0 \rightarrow \pi^+ \pi^- \pi^0$$

In this decay channel of a neutral kaon, the opening angle between the charged pions has a flat distribution. So some fraction of these events passes the criteria used to select an e^+e^- pair.

All golden backgrounds have similar lifetime distributions. Since these backgrounds become important at longer lifetimes the amount of background is estimated to be $(2.41 \pm 0.06)\%$ (integrated over all lifetimes) from the fit of the measured lifetime distribution (sec. 6.6).

6.5 Summary of Cuts

The applied cuts are summarized in table 6.1. In the second column the number of events accepted after applying the cut (and all the previous cuts) is shown. We show the number of events in the lifetime interval $[1 - 15] \tau_S$, because only these events are used to determine the CP violation parameters (see sec. 6.7.4). Next columns present the rejection of simulated signal events. The cut requiring no hits in the first layer of proportional chambers suppresses also the signal events with π^0 Dalitz decays. The effect of this cut can be observed in the lifetime acceptance distribution (fig. 6.25), where most of these events with lifetime $< 3 \tau_S$ are rejected. The events with longer lifetime are not so strongly affected by this cut.

Cuts applied	Number of accepted events in the lifetime region $[1, 15] \tau_S$		
	Data $\times 1000$	Monte Carlo	
		π^0 Dalitz decay	γ conversion
Prefiltering & general quality cuts	1366	1000	1000
$Prob(1C\text{-fit}) > 10\%$	664	881	876
$M_{inv}(e^+e^-) < 40 \text{ MeV}/c^2$	565	857	857
$N_{shower} \leq 3$	546	844	841
$\sigma(\tau) < 1.5 \tau_S$	281	661	598
dE/dx cuts	218	562	505
suppression of fake γ 's	202	526	471
no hits in PC1 for e^+e^-	104	92	357
$K^0 \rightarrow 3\pi^0$ suppression	88	60	303

Table 6.1: Summary of cuts applied in the $K^0 \rightarrow \pi^0\pi^0$ analysis. Number of simulated events after prefiltering and general quality cuts is normalized to 1000.

6.6 Neutral Kaon Lifetime

The reconstructed neutral kaon lifetime distribution is shown in figure 6.16. The events are selected using all the selection criteria described in the previous sections.

The lifetime of the short living neutral kaon component K_S and the amount of golden background are obtained from the fit of the measured lifetime distribution. The theoretical K_S^0 decay rate is corrected using the lifetime dependent detection efficiency obtained from the Monte Carlo simulation separately for the Dalitz decays and for the γ conversion (fig. 6.25). The combined efficiency is found using the ratio of the events with Dalitz decays and γ conversion obtained in section 6.3 ($\approx 34\%$ of events with Dalitz decays in the 3 to 4 τ_S lifetime interval).

The resulting rates are convoluted numerically with the lifetime resolution given by the Monte Carlo simulation (sec. 6.2.2) using the formula

$$R_{obs}(\tau) = N \int_0^{t_{max}} \epsilon(t) R_{theor}(t) \Gamma(\tau - t) dt + bck g(\tau) \quad (6.2)$$

where $R_{obs}(\tau)$ denotes the observed decay rate of neutral kaons, $R_{theor}(t)$ the theoretical

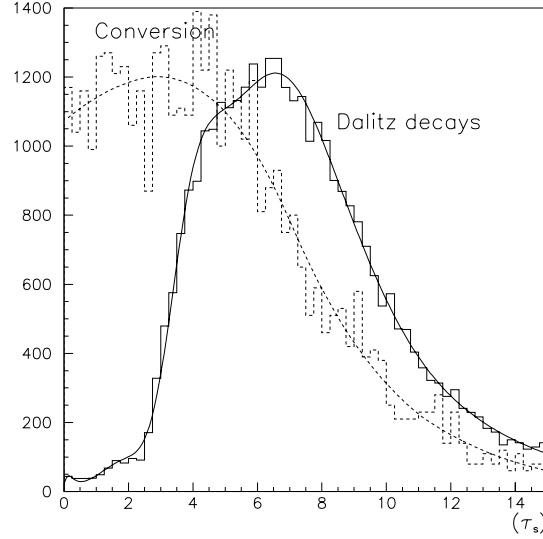


Figure 6.25: Lifetime dependent acceptance for Dalitz decays (solid line) and photon conversion (dashed line) obtained from Monte Carlo simulation. The vertical scale is in arbitrary units.

decay rate, $\epsilon(t)$ the efficiency and $\Gamma(\tau - t)$ stays for the lifetime resolution. Finally the golden background contamination with a lifetime shape taken from Monte Carlo simulation is added. The relative ratio of the golden backgrounds is calculated using the branching ratios and the detection efficiency taken from the Monte Carlo simulation. The resulting distribution is fitted to the measured lifetime distribution.

The fitted parameters are the K_S^0 lifetime, the amount of the golden background and an overall normalization. The fitted curve is shown in figure 6.26. The fit starts from $1 \tau_S$ to avoid a big contamination of the annihilation backgrounds.

The K_S^0 lifetime obtained is $0.998 \pm 0.005 \tau_S$ and the golden background contamination is $(2.41 \pm 0.06)\%$ (integrated over all lifetimes). The amount of golden background obtained from the fit is used later in the asymmetry fit.

The contaminations of individual backgrounds are summarized in table 6.2. At long lifetimes the golden backgrounds with non- $\pi^0 \pi^0$ kaon decays are dominant. At shorter lifetimes the annihilation backgrounds become important.

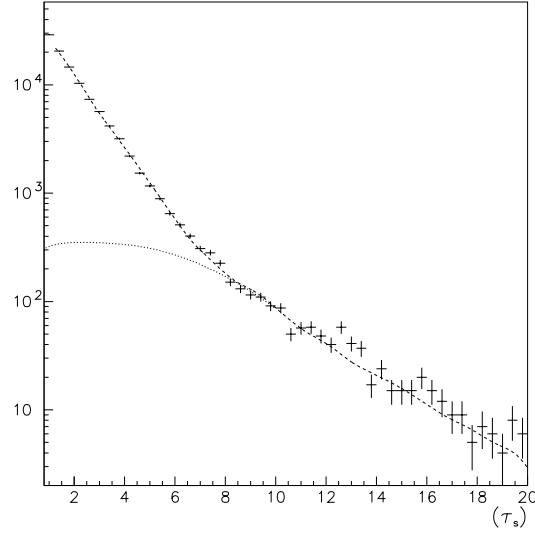


Figure 6.26: Fit to the reconstructed neutral kaon lifetime distribution giving a K_S^o lifetime of $0.998 \pm 0.005 \tau_S$ and an amount of background of $(2.41 \pm 0.06)\%$ over all lifetimes. The golden background contamination is marked using a dotted curve.

Channel	All lifetimes	$[1 - 15] \tau_S$
$p\bar{p} \rightarrow \pi^+ \pi^- n \pi^o$	4.0%	0.2%
$p\bar{p} \rightarrow K^+ K^- n \pi^o$	0.1%	0.01%
fake γ 's	$< 0.4\%$	$< 0.6\%$
$p\bar{p} \rightarrow \pi^o + K^\mp \pi^\pm K^o(\bar{K}^o)$	1.8%	2.0%
K^o decays other than $K^o \rightarrow \pi^o \pi^o$	2.4%	3.3%

Table 6.2: Background contaminations.

6.7 Determination of the CP Violation Parameter φ_{oo}

The measured lifetime dependent asymmetry (see sec. 3.2.3) is calculated from the measured decay rates $R_{meas}(t)$ and $\bar{R}_{meas}(t)$ (fig. 6.27) according to:

$$A_{oo}^{meas}(\tau) = \frac{\bar{R}_{meas}(\tau) - R_{meas}(\tau)}{\bar{R}_{meas}(\tau) + R_{meas}(\tau)} \quad (6.3)$$

The measured asymmetry is shown in figure 6.28. We can observe a clear lifetime dependence which is a sign of CP violation. Before describing the asymmetry fit we discuss some other effects influencing the asymmetry.

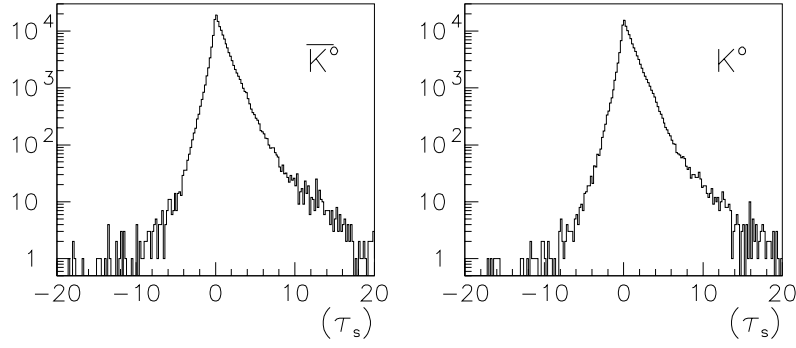


Figure 6.27: Reconstructed \overline{K}^0 and K^0 decay rates. Different lifetime shapes are a sign of the CP violation. The difference is emphasized by presenting it in the form of the lifetime dependent asymmetry (fig. 6.28).

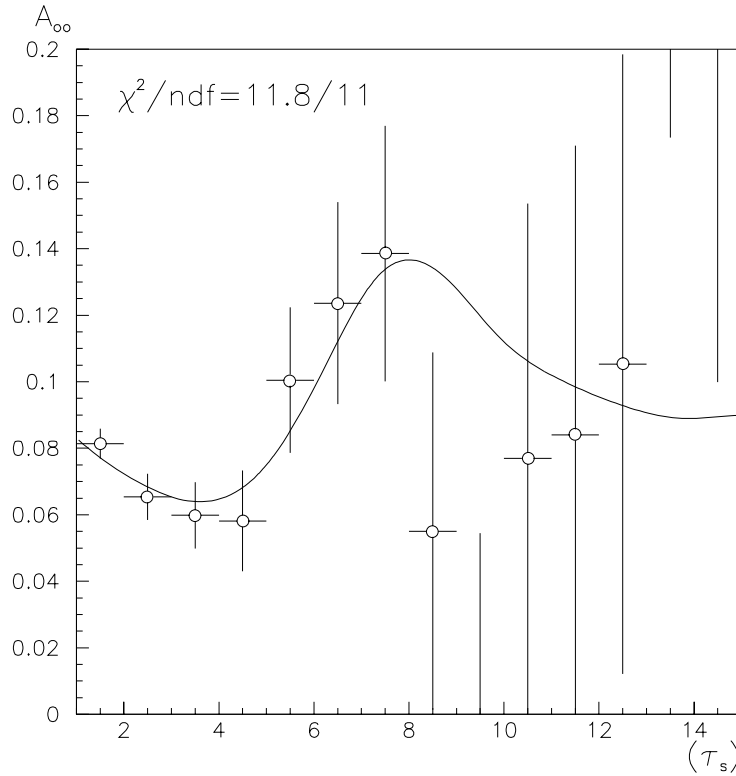


Figure 6.28: The measured decay asymmetry $A_{oo}(\tau)$. The solid line is calculated from the results of the fit (sec. 6.7.4).

6.7.1 Normalization

Compared to the theoretical asymmetry (fig. 3.3) the observed asymmetry has a visible offset. It originates from the different detection efficiencies of identifying \overline{K}^0 and K^0 in the experiment. A ratio α of these efficiencies deviates from unity since the charged particles used to determine the neutral kaon strangeness interact differently in the detector material, depending on their charge and momentum [35]. Therefore, the normalization α can depend on the event kinematics. However figure 6.29 shows, that within the statistical fluctuations the normalization does not depend on the neutral kaon momentum. The normalization also does not depend on the angle between the K^0 flight direction and the beam axis (dip angle).

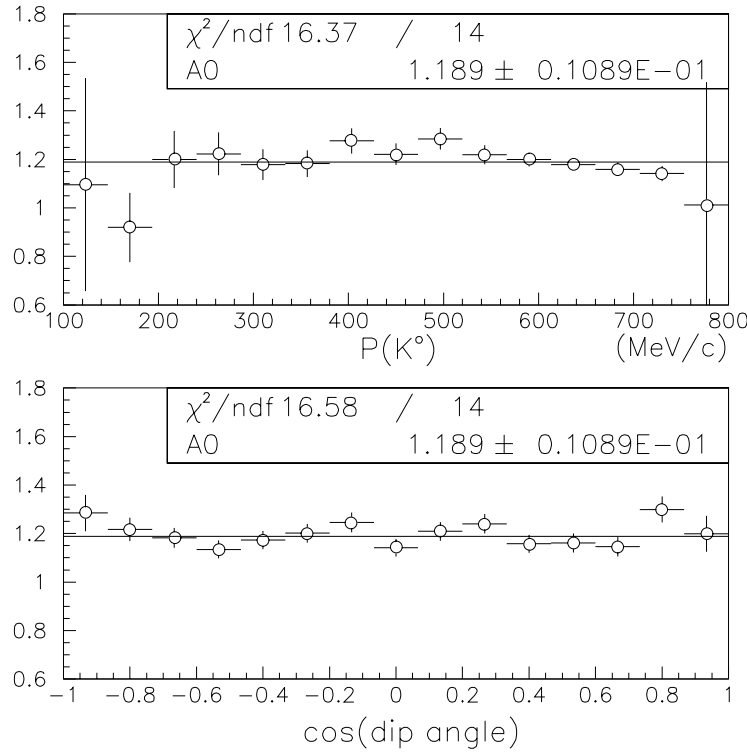


Figure 6.29: Normalization α as a function of the K^0 momentum (upper plot) and the dip angle (lower plot). The normalization is flat within the statistical fluctuations.

6.7.2 Lifetime Resolution and Backgrounds

The amplitude of the observed asymmetry depends on the lifetime resolution and on the background level. Figure 6.30 shows the asymmetry obtained by a perfect

lifetime resolution and no background, compared with the asymmetry expected by the measured lifetime resolution and no background (see sec. 6.2.2). We see, that the resolution effect on the asymmetry amplitude is small. The amplitude reduction due to the presence of backgrounds is much more significant.

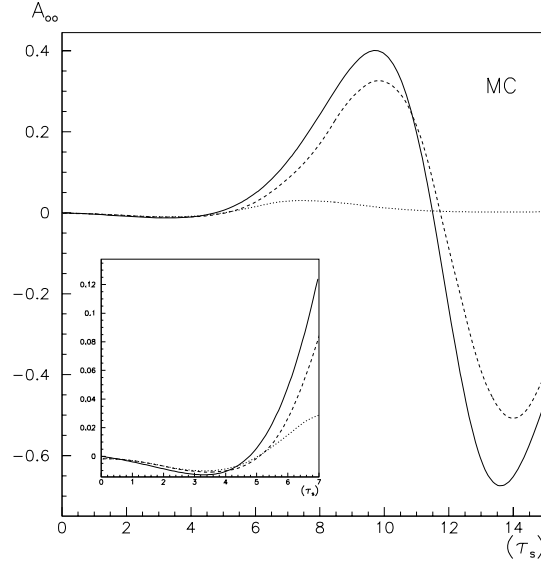


Figure 6.30: Asymmetry $A_{oo}(\tau)$ expected with an ideal lifetime resolution (solid line) and with the resolution achieved in this analysis (dashed line). The dotted line shows the asymmetry after adding the backgrounds. The small plot shows the asymmetry for the lifetime interval $[0 - 7] \tau_S$.

6.7.3 Coherent Regeneration

The neutral kaons interact strongly while passing through the detector material. The interactions change the proportion of \overline{K}^0 and K^0 in the neutral kaon wave function, as described in section 3.5. Knowing the regeneration amplitudes and the material distribution inside the detector we can correct for this effect [43]. The regeneration corrections result in a $+2.5^\circ$ shift of the measured phase of η_{oo} .

6.7.4 Fit to the Measured Asymmetry

The CP violation parameters φ_{oo} and $|\eta_{oo}|$ are obtained from the fit to the observed lifetime dependent asymmetry. The measured rates used in the fit are calculated ac-

cording to equation 6.2, namely:

$$\begin{aligned} R_{obs}(\tau) &= N \int_0^{t_{max}} \epsilon(t) R_{\pi\pi}(t) \Gamma(\tau - t) dt + bckg(\tau) \\ \overline{R}_{obs}(\tau) &= \alpha N \int_0^{t_{max}} \epsilon(t) \overline{R}_{\pi\pi}(t) \Gamma(\tau - t) dt + \overline{bckg}(\tau) \end{aligned} \quad (6.4)$$

The theoretical decay rates of the initially pure \overline{K}^o and K^o states (eq. 3.36) are corrected using the lifetime dependent efficiency (sec. 6.6) and the lifetime resolution obtained from the Monte Carlo simulation (sec. 6.2.2). To the obtained rates the backgrounds estimated in section 6.4 are added. The asymmetry function obtained from the above rates $A_{oo}^{obs}(\tau) = (\overline{R}_{obs}(\tau) - R_{obs}(\tau)) / (\overline{R}_{obs}(\tau) + R_{obs}(\tau))$ is fitted to the observed asymmetry using the least-squares fit method.

The normalization α_G for the golden backgrounds is assumed to be the same as for the signal events, i.e. $\alpha_G = \alpha$. The fit starts at $1 \tau_S$ in order to reduce the influence of the annihilation backgrounds.

In the fit to the asymmetry the fitted parameters are the modulus of η_{oo} and its phase φ_{oo} . The $K_L - K_S$ mass difference Δm is fixed at $0.5307 \cdot 10^{10} \hbar/s$, which is the present world average including the recent CPLEAR measurements [45]. The normalization α is also left as a free parameter.

The value of φ_{oo} extracted from the χ^2 fit to the asymmetry is:

$$\varphi_{oo} = 62^\circ \pm 11^\circ \text{ (stat)} \quad (6.5)$$

The magnitude of η_{oo} is measured to be $|\eta_{oo}| = (3.9 \pm 1.3) \cdot 10^{-3}$ and the normalization is $\alpha = 1.19 \pm 0.01$.

The value of $|\eta_{oo}|$ agrees within the errors with the present world average $|\eta_{oo}| = (2.259 \pm 0.023) \cdot 10^{-3}$ and φ_{oo} is 1.7 standard deviations apart from the world average $\varphi_{oo} = 43.3^\circ \pm 1.3^\circ$ [19]. Fixing the value of $|\eta_{oo}|$ to the world average value gives a 1° shift of the measured φ_{oo} value, i.e. $\varphi_{oo} = 63^\circ$.

Figure 6.31 shows the reduced asymmetry which emphasizes the CP violation effect at short lifetimes. It is obtained by the transformation

$$A_{oo}^{red}(\tau) = \left(A_{oo}(\tau) - \frac{\alpha - 1}{2} - 2\mathcal{R}e(\varepsilon_T + \varepsilon_{CPT}) \right) \cdot e^{-\frac{\Gamma_S + \Gamma_L}{2} \tau} \quad (6.6)$$

6.7.5 Systematic Errors

In this section, the systematic errors of φ_{oo} are analysed. The following sources of systematic errors are investigated:

- lifetime resolution
- background level and normalization

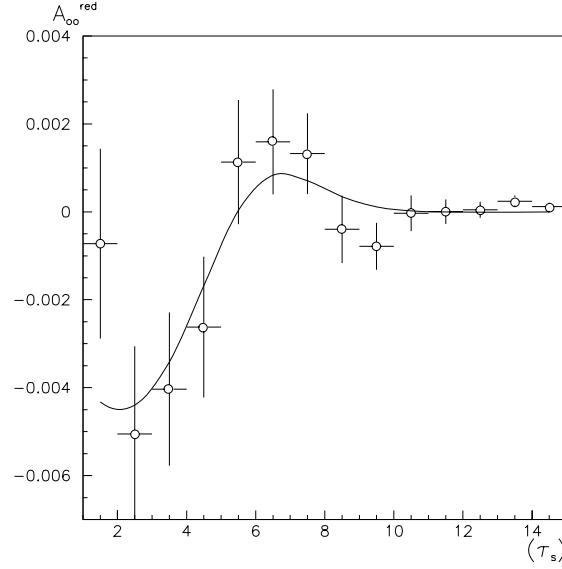


Figure 6.31: The reduced K^0 and \bar{K}^0 decay asymmetry emphasizes the CP violation effect at short lifetimes.

- lifetime dependent efficiency
- regeneration
- $K_L - K_S$ mass difference

Lifetime Resolution. The lifetime resolution used for the asymmetry fit is obtained from the Monte Carlo simulation. We check how well the Monte Carlo reproduces the lifetime resolution using two methods:

1. In the first method $p\bar{p} \rightarrow K^+ K^- n\pi^0$ ($n > 0$) events with Dalitz decays or a photon conversion are selected using the energy deposited by the charged particles in the inner scintillator $S1$. We require also the e^+e^- invariant mass to be lower than $15 \text{ MeV}/c^2$ to select a clean sample of e^+e^- pairs. In this channel we have no significant background. The reconstructed lifetime distributions for the selected data events and for the Monte Carlo simulation are presented in figure 6.32. By fitting the function built from two gaussians to both distributions we find, that the Monte Carlo lifetime distribution is by $\approx 7\%$ broader and also slightly asymmetric with respect to the data.
2. The Monte Carlo precision in reconstructing the neutral kaon lifetime depends on the accuracy of the vertex reconstruction. In figure 6.13 we find the distribution of the distance between the reconstructed conversion vertex and the K^0 decay

vertex. While fitting the function built from two gaussians to the distributions obtained from the data and simulated events with Dalitz decays we find that data events give a distribution which is $\approx 5\%$ broader.

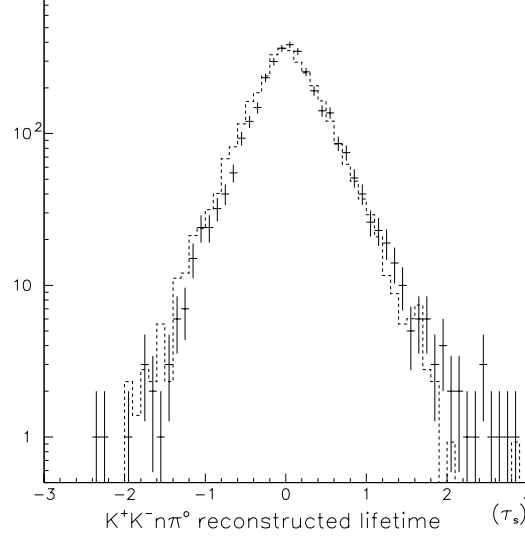


Figure 6.32: The lifetime distribution for the selected $p\bar{p} \rightarrow K^+K^-n\pi^0$, $n \geq 1$ events (crosses) compared with the Monte Carlo simulation (dashed line). The deviation of the two distributions is a measure how well the Monte Carlo simulation reproduces the data.

From these two checks we conclude that the lifetime resolution is reproduced with an accuracy better than $\pm 10\%$. Such a variation of the lifetime resolution leads to a systematic error $\Delta\varphi_{00} = 1^\circ$.

Golden Backgrounds. The background contribution used in the asymmetry fit is obtained from the fit to the reconstructed neutral kaon lifetime spectrum. The variation of the background contribution by three standard deviations results in a systematic error $\Delta\varphi_{00} = 0.1^\circ$.

Golden+ π^0 Background. The variation of the golden+ π^0 contamination by 20% leads to an error of $\Delta\varphi_{00} = 0.02^\circ$.

Annihilation Background. The pionic and kaonic annihilation backgrounds are observed at short lifetimes and have the normalization $\alpha_{\pi\pi}$ and α_{KK} different from the one of the signal events. The normalization of the dominant pionic background measured using the method of fitting the dE/dx spectra separately for the events

with a reconstructed K^0 and \overline{K}^0 is found to be around $\alpha_{\pi^+\pi^-} = 1.1$. It can vary between 1.05 and 1.15. Such a variation of the normalization leads to a systematic error of $\Delta\varphi_{00} = 1^\circ$. A similar systematic error originates from an inaccuracy of the measurement of the background contribution.

Fake Photons. The normalization of the background α_{fake} where fake photons are misidentified as signal photons, is measured to be ≈ 1.4 . The amount of fake photon background is obtained from the distribution of the distance between the kaon and photon flight paths (fig. 6.18). This is in fact only an upper limit, since after applying all the cuts the broad component in this distribution corresponding to the background cannot be clearly distinguished from the distribution given by the good events.

The results of the asymmetry fit are corrected for contribution of the fake photon background at the half of the estimated upper limit. Changing the amount of background from this contribution up to the upper limit we obtain a $\Delta\varphi_{00} = 0.5^\circ$.

Acceptance. The acceptance changes with the neutral kaon lifetime. The lifetime dependence of the acceptance used in the asymmetry fit is taken from the Monte Carlo simulation. The fitted value of φ_{00} is not very sensitive to variation of the acceptance function. Even the replacement of the Monte Carlo acceptance by the flat acceptance gives a $\Delta\varphi_{00} = 0.1^\circ$. This error is small due to the acceptance cancellation in the asymmetry function.

Coherent Regeneration. The regeneration scattering amplitudes are known only with a precision of $\approx 10\%$ of their modulus and $\approx 10^\circ$ of the phases [43]. By varying the amplitudes within this range we obtain $\Delta\varphi_{00} = 0.4^\circ$.

$K_L - K_S$ Mass Difference. The $K_L - K_S$ mass difference Δm is used as a parameter in the asymmetry fit. Its value is taken from the world average improved by the CPLEAR measurements (sec. 6.7.4). The 1σ variation of Δm leads to $\Delta\varphi_{00} = 1^\circ$.

Table 6.3 summarizes the systematic errors discussed above. The total systematic error is calculated by adding the individual systematic errors in quadrature.

6.8 Conclusions

The analysis presented here uses a different approach to the K^0 lifetime reconstruction than the standard method where four photons detected in the calorimeter are used. By using converted photons and Dalitz decays the neutral kaon decay vertex can be reconstructed and CP violation effects are observed. The final result of the

Source	Variation	$\Delta\varphi_{oo}$ [$^\circ$]
Lifetime resolution	$\pm 10\%$	1
Golden background contribution	$\pm 3\sigma$	0.1
Golden+ π^0 background contribution	$\pm 20\%$	0.02
Pionic background normalization	$\pm 5\%$	1
Pionic background contribution	see text	1
Fake photons	see text	0.5
Acceptance	see text	0.1
Regeneration	$\pm 10\%$, $\pm 10^\circ$	0.4
Δm	$\pm 1\sigma$	1
Total		2.3

Table 6.3: Systematic errors.

measurement is:

$$\varphi_{oo} = 62^\circ \pm 11^\circ(stat) \pm 2^\circ(syst) \quad (6.7)$$

Including all the data collected in 1995 we should have in total around 500 000 events, which should reduce the final statistical error to $\Delta\varphi_{oo}(stat) = 8^\circ$. The systematic errors are much smaller than the statistical errors, which shows the potential of the method achieved mostly due to the good K^0 lifetime resolution.

The lifetime resolution obtained ($0.38 \tau_S$ RMS, $0.2 \tau_S$ FWHM) is better than the resolution achieved in the analysis using four photons detected in the calorimeter ($1.0 \tau_S$ RMS, $0.7 \tau_S$ FWHM [4, 37]). Unfortunately the lower number of reconstructed events and higher background contamination does not allow to reach the statistical precision of $\Delta\varphi_{oo} = 7.1^\circ$ obtained in that analysis.

Other analyses can also benefit from the techniques developed for this study. In 1996 the CPLEAR experiment is performing the measurement of the K_S^0 regeneration using a 2.5 cm thick carbon regenerator placed inside the PC1 proportional chambers. This measurement is very important, since the main systematic error in the analysis of the CP violation of the $K^0 \rightarrow \pi^+\pi^-$ decays comes from the uncertainties in the present knowledge of the K_S^0 regeneration amplitudes. The exact position of the regenerator, which is important for the final measurement, can be measured using the photon conversion in the regenerator material [46].

Furthermore, in the analysis of $K^0 \rightarrow \pi e \nu$ decays the pion/electron separation is based on the Particle Identification Detector (PID) response [47]. The selection using a Neural Network technique has been optimized using electron data from converted photons.

Chapter 7

Search for CP Violation in $K^0 \rightarrow \pi^0 \pi^0 \pi^0 \rightarrow 6\gamma$ Decays

CP violation has never been observed in $K^0 \rightarrow \pi^0 \pi^0 \pi^0$ channel. The best limit on CP violation in this decay channel comes from a bubble chamber experiment performed at ITEP (Moscow) [5]. The experiment identified 632 \bar{K}^0 decays into three neutral pions and measured the CP violation parameter to be $\eta_{ooo} = (-0.08 \pm 0.18) + i(-0.05 \pm 0.27)$. Their result is within one standard deviation compatible with $\eta_{ooo} = 0$. In order to provide the best upper limit for $\mathcal{I}m(\eta_{ooo})$ the authors constrained $\mathcal{R}e(\eta_{ooo})$ to $\mathcal{R}e(\varepsilon)$. Then they obtained $\mathcal{I}m(\eta_{ooo}) = -0.02 \pm 0.18$. The direct CP violation would effect only $\mathcal{I}m(\eta_{ooo})$ (see sec. 3.3), therefore the measurement of $\mathcal{I}m(\eta_{ooo})$ puts a limit on the eventual direct CP violation in $K^0 \rightarrow \pi^0 \pi^0 \pi^0$ decays. It also improves the precision of the CPT tests comparing the phase of η_{+-} with the superweak phase φ_{SW} where the present knowledge of $\mathcal{I}m(\eta_{ooo})$ introduces a large uncertainty (see sec. 3.2.2).

The CPLEAR electromagnetic calorimeter is capable of detecting the low energetic photons from the $K^0 \rightarrow \pi^0 \pi^0 \pi^0 \rightarrow 6\gamma$ decay chain. The analysis presented in this chapter is based on a small data sample containing approximately 1/4 of all the collected events. This analysis is a feasibility study of the capability of the CPLEAR experiment to reconstruct $K^0 \rightarrow \pi^0 \pi^0 \pi^0$ decays and to improve the present upper limit on η_{ooo} . This analysis was performed in close collaboration with Dr. B. Pagels.

7.1 Event Selection and Reconstruction

In the reconstruction of golden events ($p\bar{p} \rightarrow K\pi K^0$) with $K^0 \rightarrow \pi^0 \pi^0 \pi^0 \rightarrow 6\gamma$ decays we require that all the produced particles are detected in the experimental setup. The tracks of the primary kaon and pion are detected in the tracking devices. The six photons are observed in the electromagnetic calorimeter as neutral showers (fig. 7.1).

In this section we present the preselection of events, the method of event reconstruction which yields the neutral kaon lifetime and aims to suppress background events. Before we discuss each point in detail, we list the possible background channels:

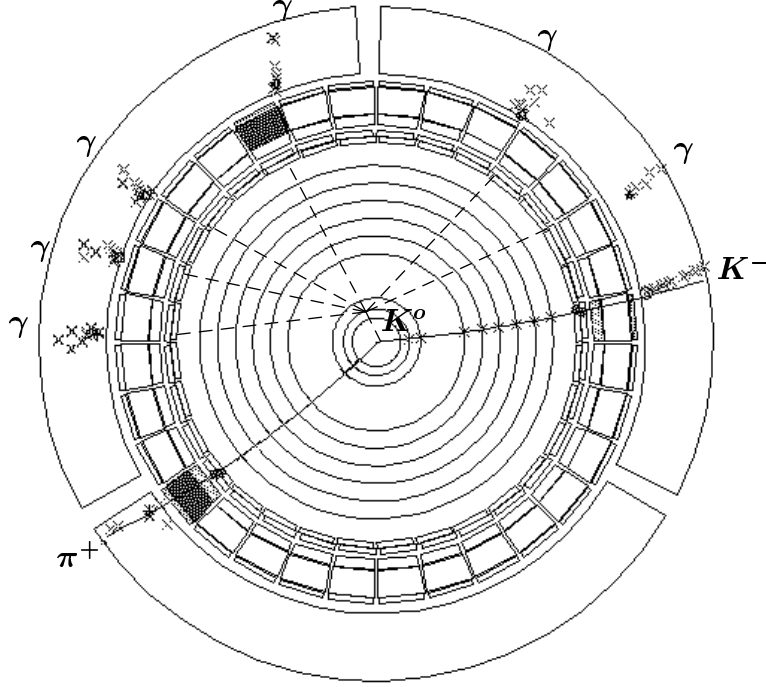


Figure 7.1: A $K^0 \rightarrow \pi^0 \pi^0 \pi^0 \rightarrow 6\gamma$ event. The neutral kaon decays into $3\pi^0$ which give six photons detected as neutral showers in the calorimeter.

- $p\bar{p} \rightarrow \pi^0 + K^\mp \pi^\pm K^0(\bar{K}^0)$ where beside K , π and K^0 an additional neutral pion is produced at the annihilation vertex (golden+ π^0 background). The neutral kaon can decay into two or three neutral pions.
- $p\bar{p} \rightarrow K^\mp \pi^\pm K^0(\bar{K}^0)$ where the neutral kaon decays into $2\pi^0$. In addition, two fake photons (giving the total photon multiplicity 6) are produced by secondary interactions (see chapter 5).
- $p\bar{p} \rightarrow \pi^+ \pi^- n\pi^0$, $n > 0$ with photons originating from neutral pion decays and where the charged pion is misidentified as a charged kaon (pionic background).

All the above background channels are characterized by two tracks and in general by a high multiplicity of photons detected in the calorimeter.

7.1.1 Preselection

Primary Particles

The charged kaon and pion are identified in a similar way as in the $K^0 \rightarrow \pi^0 \pi^0$ analysis (section 6.1). A charged particle with a momentum between $400 \text{ MeV}/c$ and

800 MeV/c coming from the center of the detector and giving signals in both the inner and outer scintillator of a sector but no light in the Čerenkov counter is recognized as a charged kaon candidate. The second particle is assumed to be a charged pion if its momentum is greater than 100 MeV/c and smaller than 750 MeV/c . In order to reduce the pionic background ($p\bar{p} \rightarrow \pi^+ \pi^- n \pi^0$) we require that:

1. The kaon candidate should deposit at least 2.0 MeV/cm energy in the scintillator and the deposited energy must be by at least by two standard deviations higher than the one expected for the pion carrying the same momentum.
2. The measured time of flight difference $\Delta ToF(K\pi)_{meas}$ of the two charged particles agrees with the hypothesis, that these particles are a kaon and a pion. We require $\Delta ToF = |\Delta ToF(K\pi)_{meas} - \Delta ToF(K\pi)_{expected}| < 0.7 \text{ ns}$, where $\Delta ToF(K\pi)_{expected}$ is calculated from the particle momenta and the path length from the detector center to the scintillator S1 (see section 4.3).

Photons

Exactly six neutral showers are required in the electromagnetic calorimeter. The method of selecting neutral showers is described in section 4.4. In order to measure the γ energy we require that two neutral showers do not overlap in the wire projection.

In some regions of the calorimeter one finds more neutral showers which are assumed to be photons than in the others regions. In figure 7.2 a (φ, Z) map of the photon conversion points in the calorimeter is shown (Z is the axis parallel to the beam, φ is the azimuthal angle). We can see spikes at the edges of the calorimeter, i.e. at large negative and positive Z values. The spikes are related to a gas flow problem observed during the calorimeter operation. We reject events with neutral showers located in these regions.

7.1.2 Complete Event Reconstruction

The neutral kaon decay time is reconstructed by means of a kinematical and geometrical constrained fit to the $p\bar{p} \rightarrow K^\mp \pi^\pm K^0(\bar{K}^0)$, $K^0 \rightarrow \pi^0 \pi^0 \pi^0 \rightarrow 6\gamma$ hypothesis (for a general introduction to constrained fits see appendix C).

The measured quantities used in the fit are the momenta of the primary tracks, the annihilation vertex, the photon impact points in the calorimeter (only φ and Z components can vary during the fit, the r component is fixed at the measured radius) and the photon energies. The only unknown is the neutral kaon decay-time [48]. The

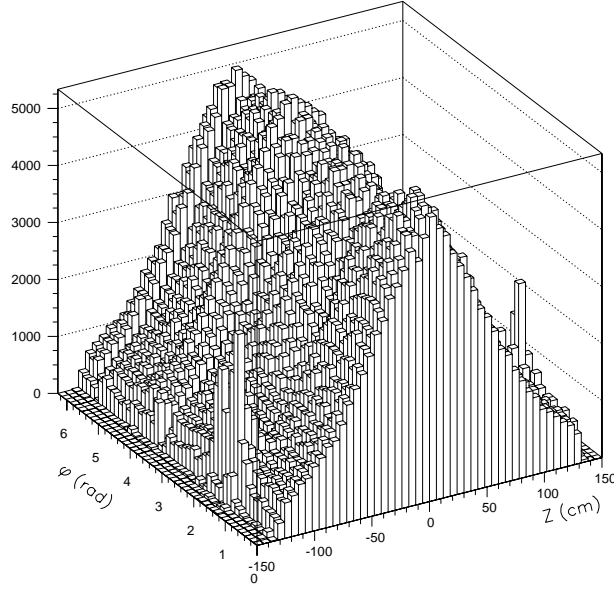


Figure 7.2: Distribution of the photon conversion points in the $\varphi - Z$ plane. φ is the azimuthal angle around the Z -axis which is parallel to the beam.

eight applied constraints are:

$$\begin{aligned}
 f_1 &= 2m_p - (E_K + E_\pi + \sum_{i=1}^6 E_i) \\
 f_{2-4} &= \vec{p}_K + \vec{p}_\pi + \sum_{i=1}^6 \vec{p}_i \\
 f_5 &= m_{K^0}^2 - (2m_p - E_K - E_\pi)^2 + (\vec{p}_K + \vec{p}_\pi)^2 \\
 f_6 &= \frac{1}{2}m_{\pi^0}^2 - (E_1 E_2 - \vec{p}_1 \cdot \vec{p}_2) \\
 f_7 &= \frac{1}{2}m_{\pi^0}^2 - (E_3 E_4 - \vec{p}_3 \cdot \vec{p}_4) \\
 f_8 &= \frac{1}{2}m_{\pi^0}^2 - (E_5 E_6 - \vec{p}_5 \cdot \vec{p}_6)
 \end{aligned} \tag{7.1}$$

Here $\vec{p}_K(\vec{p}_\pi)$ and $E_K(E_\pi)$ denote the charged kaon (pion) momentum and energy, respectively. The E_i and \vec{p}_i are the energies and momenta of the six photons. The masses of the proton, K^0 and π^0 are denoted by m_p , m_{K^0} and m_{π^0} , respectively.

The constraint equations (eq. 7.1) require energy and momentum conservation ($f_1 - f_4$), equality of the $K^\pm \pi^\mp$ missing mass with the K^0 mass (f_5) and that the invariant

masses of three $\gamma\gamma$ pairs are equal to the π^0 mass ($f_6 - f_8$). The fit with eight constraints and one unknown is called a 7C-fit.

The photon pairs originating from π^0 decays are identified by repeating the 7C-fit for each of the 15 possible photon pairings. The pairing with the lowest value of χ_{7C}^2 is chosen.

We note a special property of the 7C-fit when applied to events from the CPLEAR detector. The χ_{7C}^2 of the fit can be written as:

$$\chi_{7C}^2 = \chi_{primary}^2 + \chi_{secondary}^2 \quad (7.2)$$

where $\chi_{primary}^2$ is a function of the measured track parameters and $\chi_{secondary}^2$ a function of the measured photon parameters. They both are in general functions of all the fitted parameters and therefore expected to be strongly correlated. However, if the reconstructed K^0 momentum depends only on the primary tracks and is not affected by the photons, then $\chi_{primary}^2$ decouples from $\chi_{secondary}^2$ and $\chi_{primary}^2 = \chi_{1C}^2$, where χ_{1C}^2 is the χ^2 of the 1C-fit described in section 6.1.2. Using the primary track information the 1C-fit requires the $K^\pm \pi^\mp$ missing mass to be in agreement with K^0 mass.

The property $\chi_{7C}^2 = \chi_{1C}^2 + \chi_{secondary}^2$ is indeed fulfilled by the 7C-fit. This is demonstrated by figure 7.3 in which the $K^\pm \pi^\mp$ missing mass spectrum after a cut on $\chi_{secondary}^2$ is compared with a spectrum obtained by a cut on χ_{7C}^2 . In both cases 10% probability cuts are applied. By applying a χ_{7C}^2 cut we reject very few of the events with a $K^\pm \pi^\mp$ missing mass close to the K^0 mass.

We make use of this property of the 7C-fit, since the missing mass spectrum of the primary particles $K^\pm \pi^\mp$ is later used for background estimation. Any cut on χ_{1C}^2 or χ_{7C}^2 changes the shape of the missing mass distribution. Therefore none of these cuts is applied. Instead we apply a cut $Prob(\chi_{secondary}^2) > 10\%$ and require M_{miss}^2 to be within $[150\,000, 350\,000] \text{ MeV}^2/c^4$. The latter cut suppresses golden+ π^0 events and also the pionic background.

7.1.3 Reduction of Fake Showers

The fake showers described in chapter 5 are a significant background source. Due to them the golden events with $K^0 \rightarrow \pi^0 \pi^0 \rightarrow 4\gamma$ can be misidentified as $K^0 \rightarrow \pi^0 \pi^0 \pi^0$ events. The elimination of fake photons is more complicated and less efficient compared to the analysis using converted photons and π^0 Dalitz decays (sec. 6.4.3), since the calorimeter does not provide very precise information about the photon flight direction. Therefore this information cannot be used to recognize, whether a photon originates from a secondary interaction of one of the two charged tracks in the calorimeter. The following is a description of three methods used for suppressing events with fake photons:

1. The first step of the fake shower suppression is a rejection of all the showers with impact points closer than 50 cm to the charged kaon track. This criterion has been already discussed in section 5.1.3.

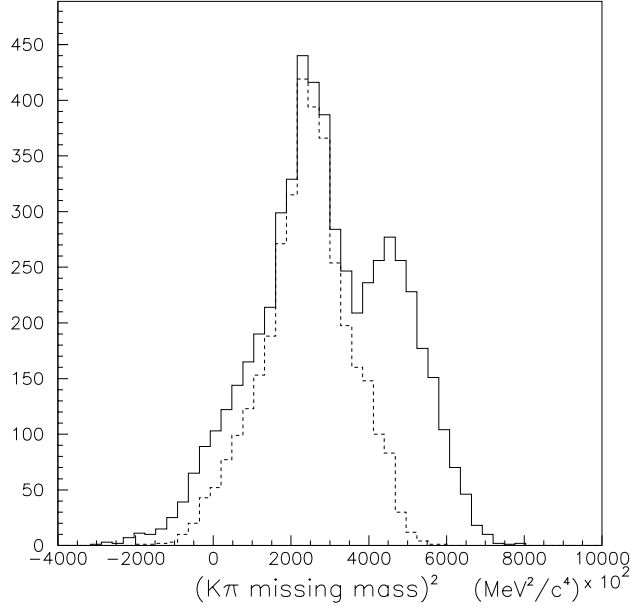


Figure 7.3: $K^\pm\pi^\mp$ missing mass distribution after applying a cut on $\chi^2_{secondary}$ (solid line) and after a cut on χ^2_{7C} (dashed line). (Events from the lifetime interval $[0, 10] \tau_S$).

2. A photon can convert before entering the calorimeter in the massive parts of detector like the Čerenkov counters located directly in front of the calorimeter. While converting into an e^+e^- pair it can produce two showers close to each other (fig. 7.4). Such a background is suppressed by a cut on the minimal $\gamma\gamma$ invariant mass $m_{\gamma\gamma}^{min} = \min_{i,j=1,6, i < j} (m_{\gamma_i\gamma_j})$ out of all possible invariant masses calculated using the photon energies and the neutral kaon decay vertex obtained from the 7C-fit. In figure 7.5 the $m_{\gamma\gamma}^{min}$ distribution of two photons is shown for simulated signal events and simulated $K^0 \rightarrow \pi^0\pi^0$ background decays. In the second channel we expect two fake showers. A significant difference between the distributions can be observed. In the second plot the distribution of the two photon invariant mass is shown for the data events. A distinct peak can be observed at the invariant mass, where the signal from the background showers is expected. In order to reduce the background we require $m_{\gamma\gamma}^{min} > 25 \text{ MeV}/c^2$.
3. For the decays $K^0 \rightarrow \pi^0\pi^0\pi^0 \rightarrow 6\gamma$ and $K^0 \rightarrow \pi^0\pi^0 \rightarrow 4\gamma$ the invariant mass of the final state photons is equal to the neutral kaon mass. However if in the second channel two additional fake photons are detected, then the invariant mass of all six photons is increased compared to m_{K^0} . In figure 7.6 we compare the invariant mass distributions calculated from all six photons for the simulated signal events and for the background $K^0 \rightarrow \pi^0\pi^0$ events. The invariant mass is calculated at

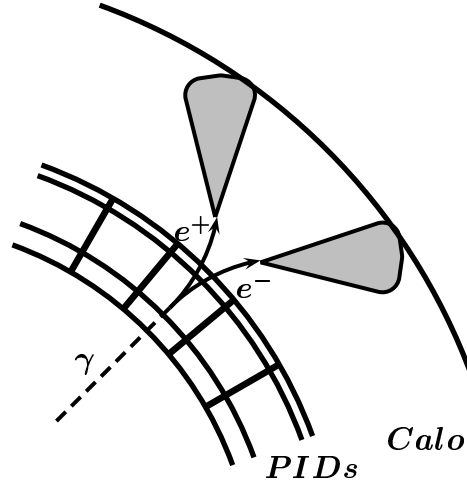


Figure 7.4: A photon conversion in the Čerenkov counter resulting in two neutral showers close to each other.

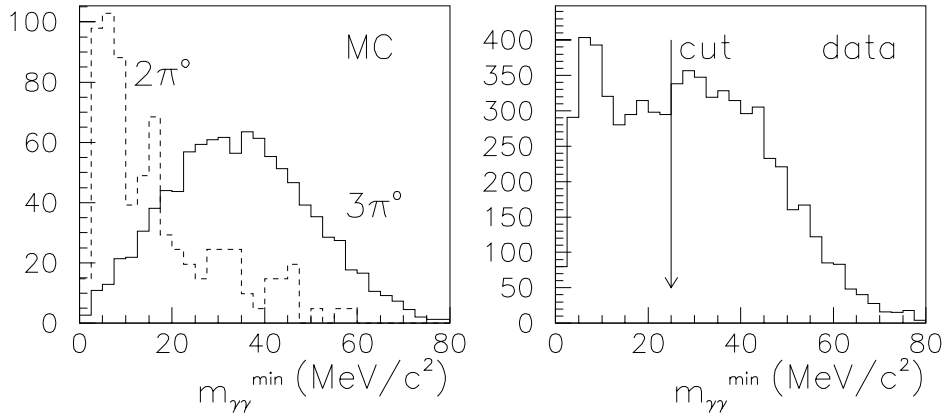


Figure 7.5: The minimal invariant mass of all two photon pairs. The left plot shows the invariant mass for simulated $K^0 \rightarrow \pi^0 \pi^0 \pi^0 \rightarrow 6\gamma$ events (solid line) and simulated $K^0 \rightarrow \pi^0 \pi^0 \rightarrow 4\gamma + 2\gamma_{fake}$ events (dashed line). In the right plot the respective distribution for data events is shown. (Events from the lifetime interval $[0, 10] \tau_S$).

the vertex obtained from the 7C-fit using the photon energies as measured in the calorimeter, with no corrections from the constrained fit. Both distributions can be compared with the invariant mass spectrum obtained in data events. In order to reduce the background, events with an invariant mass of six photons over $700 \text{ MeV}/c^2$ are rejected.

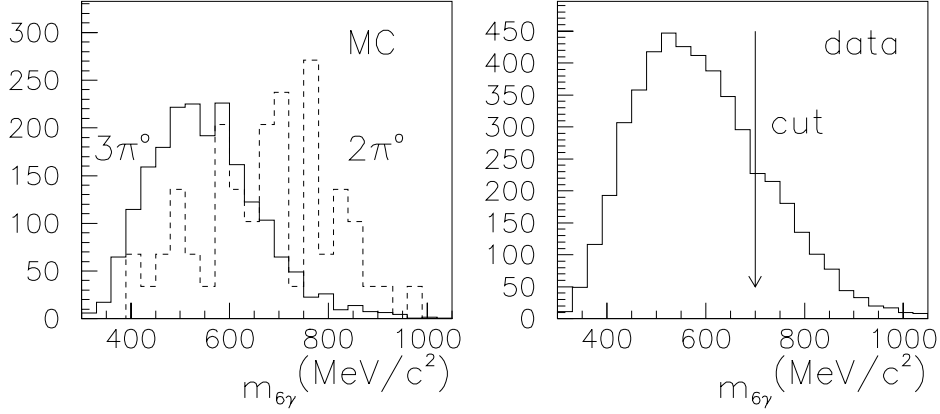


Figure 7.6: Invariant mass of all six photons for the simulated signal events (solid line) compared with the simulated $K^0 \rightarrow \pi^0\pi^0$ background events (dashed line). The right plot shows the invariant mass for data events. (Events from the lifetime interval $[0, 10] \tau_S$).

The neutral kaon lifetime for the background decays $K^0 \rightarrow \pi^0\pi^0$ with additional two fake photons can be properly reconstructed using only four neutral showers and applying the lifetime reconstruction method developed for the analysis of $K^0 \rightarrow \pi^0\pi^0 \rightarrow 4\gamma$ channel [4]. The lifetime distribution obtained should be exponential with K_S lifetime, since $K_S \rightarrow \pi^0\pi^0$ decays are dominant [49]. This is used for monitoring the suppression of the fake showers by the selection criteria presented above.

The lifetime reconstruction of $K^0 \rightarrow \pi^0\pi^0 \rightarrow 4\gamma$ events is performed by applying the 6C-fit. It is applied to all possible combinations of four photons picked out of the six detected photons. The combination leading to the highest probability is chosen. The 6C-fit is equivalent to the 7C-fit for the neutral kaon decays into two π^0 s. It has one constraint (f_8) less. It must be stressed out, that by applying this method we do not reconstruct properly the K^0 lifetime for the signal events, only for the $K^0 \rightarrow \pi^0\pi^0$ background.

Figure 7.7 shows the lifetime reconstructed by the 6C-fit for simulated $K^0 \rightarrow \pi^0\pi^0$ and $K^0 \rightarrow \pi^0\pi^0\pi^0$ events. At short lifetimes we can observe the exponential lifetime distribution from $K_S \rightarrow \pi^0\pi^0$ decays. The right plot shows the 6C-fit lifetime distri-

bution for data events before and after applying the cuts reducing the number of fake showers. The K_S lifetime contribution is significantly reduced.

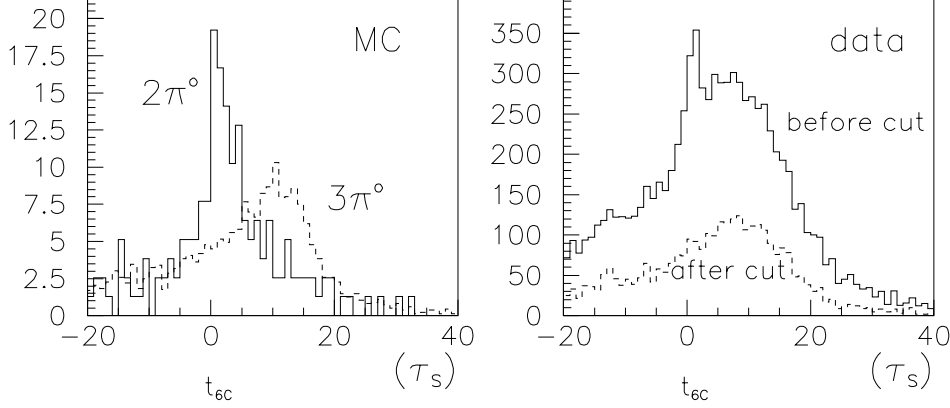


Figure 7.7: The left plot shows the distribution of the lifetime reconstructed by the 6C-fit for the simulated $K^0 \rightarrow \pi^0 \pi^0$ background events (solid line) and for the simulated $K^0 \rightarrow \pi^0 \pi^0 \pi^0$ signal events (dashed line). The right plot shows the respective distribution for the data events before (solid line) and after (dashed line) applying the cuts which suppress the fake photons. (Events from the 7C-fit lifetime interval $[0, 10] \tau_S$).

7.1.4 Lifetime and Missing Mass Distributions

The lifetime distribution as obtained from the 7C-fit is shown in figure 7.8. Most of the reconstructed data events have a negative lifetime, which could be due to a high background level. On the other hand a small peak at $t_{7C} \approx 0$ could be interpreted as a sign of signal events.

This interpretation is confirmed by the distribution of the squared $K^\pm \pi^\mp$ missing mass shown in figure 7.9 in bins of the reconstructed lifetime. The cut on the missing mass is not applied in order to visualize the background contribution. The peak at $M_{mis}^2 \approx 250\,000 \text{ MeV}^2/c^4$ corresponds to the neutral kaon production at the annihilation vertex, while the higher values of the missing mass originate from events with an additional π^0 (golden+ π^0). The additional particle produced increases the $K^\pm \pi^\mp$ missing mass. The pionic annihilation background gives a broad missing mass distribution.

The missing mass spectrum shows, that at negative lifetimes we observe mostly backgrounds. At positive lifetimes we can also find golden events ($p\bar{p} \rightarrow K^\mp \pi^\pm K^0(\bar{K}^0)$). However it must be verified, whether these are the signal events or a golden $K^0 \rightarrow \pi^0 \pi^0$

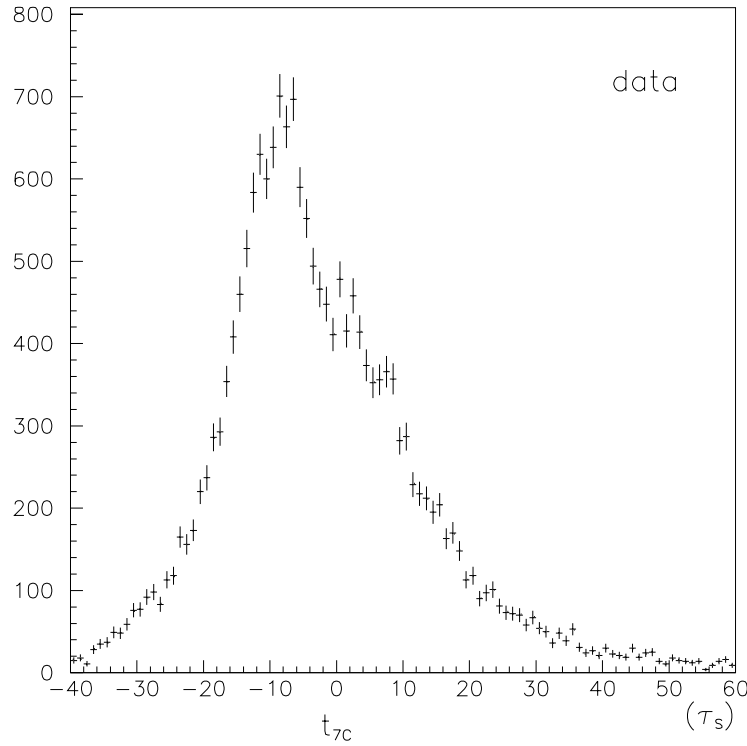


Figure 7.8: Lifetime distribution for selected data events.

background. Because of a high background contamination a reliable method of background estimation is crucial for the analysis.

7.2 Signal and Background Estimation

In the analysis of $K^0 \rightarrow \pi^0 \pi^0 \pi^0$ decays the background contribution is estimated using the reconstructed lifetime distribution of neutral kaons and the $K^\pm \pi^\mp$ missing mass spectra. They are fitted with reference distributions for signal and background obtained from the Monte Carlo simulation. The amount of pionic annihilation background as a function of physical variables (the K^0 lifetime and the $K^\pm \pi^\mp$ missing mass) is found from the fits of the energy deposited by a charged kaon candidate in the inner scintillator (the dE/dx fits are described in sec. 6.4.1).

7.2.1 Fit to the Lifetime Distribution

The amount of $K^0 \rightarrow \pi^0 \pi^0 \pi^0$ events and the background contributions can be estimated from a fit of the observed lifetime distribution. Figure 7.10 shows the lifetime shapes

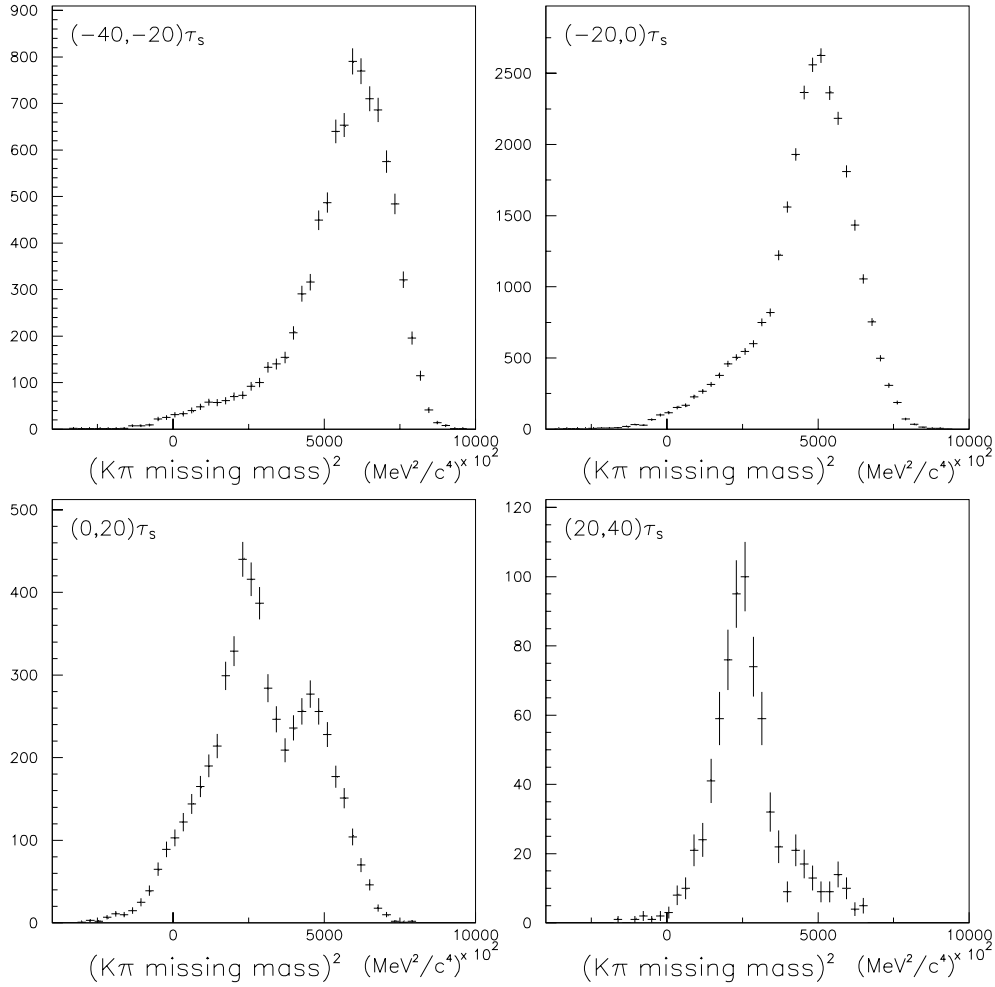


Figure 7.9: The distribution of the squared $K^\pm \pi^\mp$ missing mass for the reconstructed data events. The missing mass is shown in the bins of the reconstructed neutral kaon lifetime. The cut on the missing mass is not applied in order to visualize the whole missing mass spectrum.

for the signal and the background channels considered.

While performing the fit of the observed lifetime distribution the signal and the background contributions can vary freely (except the pionic background contribution which is fixed at the level obtained from the dE/dx fits). From the fit (see fig. 7.11) we get the background and signal contributions in the lifetime interval $[0 - 20] \tau_S$. The fit results are summarized in the second column of table 7.1.

We see that at positive lifetimes $\approx 70\%$ of all the events are signal events while the rest originates from the background channels. The proportion becomes worse at

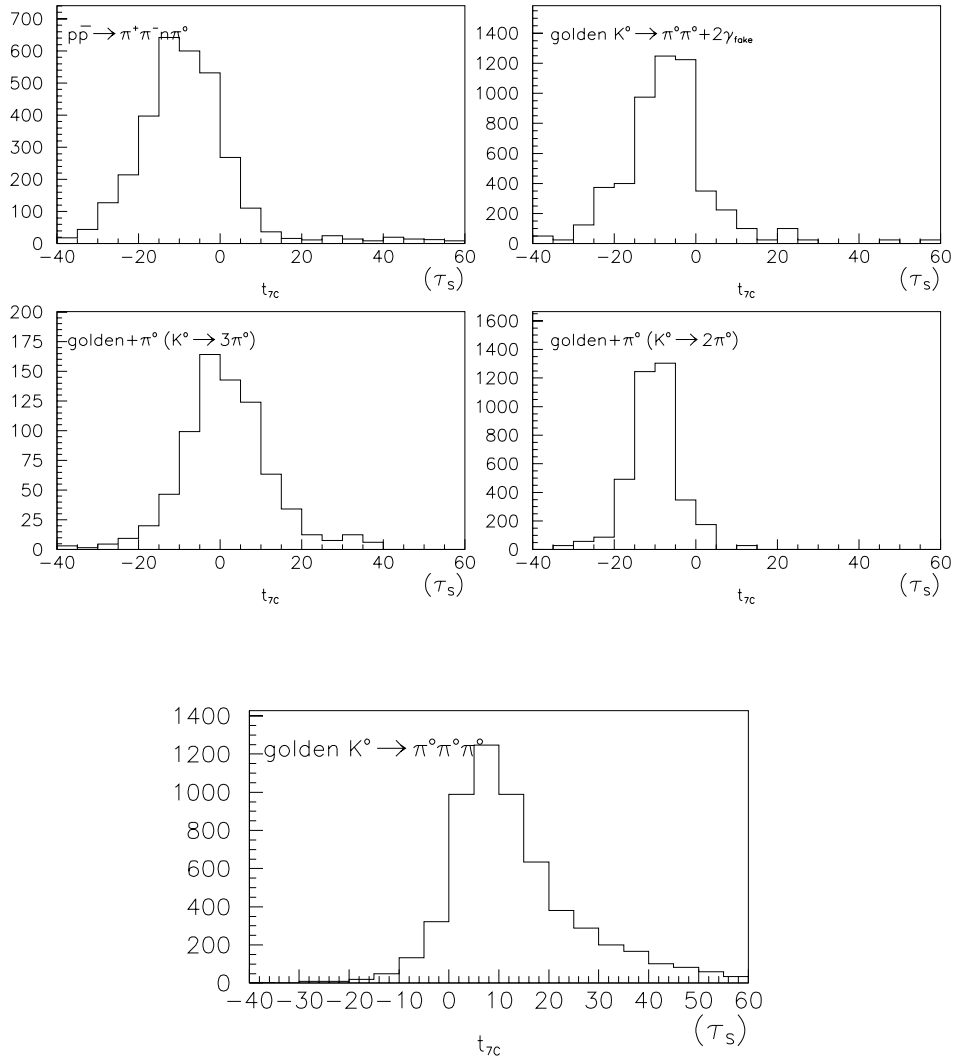


Figure 7.10: Lifetime distributions for the background channels (pionic background, golden $K^0 \rightarrow \pi^0\pi^0$ with two fake photons, golden+ π^0 with K^0 decaying into $3\pi^0$ and into $2\pi^0$) and for the signal events obtained from Monte Carlo simulation and dE/dx fits (pionic background).

short lifetimes, where CP violation effects are expected (fig. 3.5 shows the theoretical asymmetry).

Since the lifetime distribution obtained as a result of the fit does not agree perfectly with the observed distribution the statistical errors of the fit results are not given in table 7.1. Instead we compare the results of the lifetime fit with the signal and background contributions obtained from a fit of the $K^\pm\pi^\mp$ missing mass spectrum. The

Channel	Lifetime	Missing mass	Combined	Mean
$K^o \rightarrow \pi^o \pi^o \pi^o \rightarrow 6\gamma$	69.5%	72.3%	71.9%	71.2%
$K^o \rightarrow \pi^o \pi^o \rightarrow 4\gamma + 2\gamma_{fake}$	12.6%	12.1%	12.4%	12.4%
$p\bar{p} \rightarrow \pi^o + K^\mp \pi^\pm K^o(\bar{K}^o), \quad K^o \rightarrow 3\pi^o$	6.5%	4.3%	4.7%	5.2%
$p\bar{p} \rightarrow \pi^o + K^\mp \pi^\pm K^o(\bar{K}^o), \quad K^o \rightarrow 2\pi^o$	3.6%	3.3%	3.6%	3.5%
$p\bar{p} \rightarrow \pi^+ \pi^- n\pi^o, \quad n > 0$	7.8%	8.0%	7.4%	7.7%

Table 7.1: Signal and background contributions in the $[0 - 20] \tau_S$ lifetime interval obtained from lifetime and $K^\pm \pi^\mp$ missing mass fits. In the third columns the results of the combined lifetime and missing mass fit are shown. The average of results of these three fits is given in the last column.

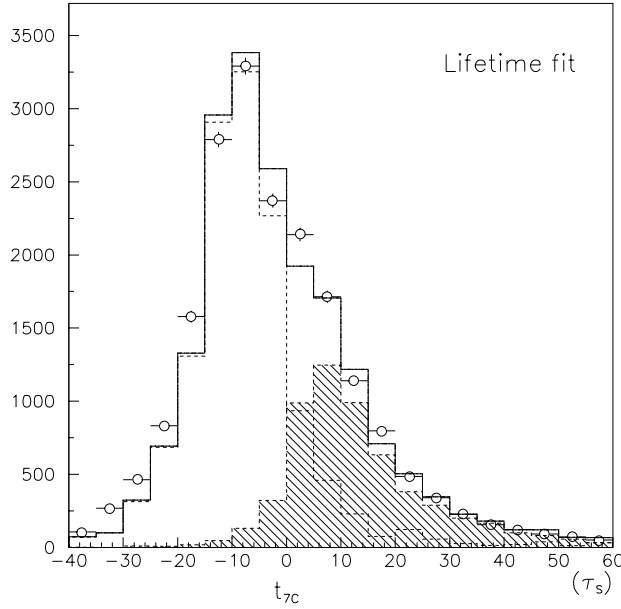


Figure 7.11: Reconstructed lifetime distribution (points) together with signal (shaded area) and background (dashed line) contaminations obtained from the lifetime fit. The solid line represents the sum of the fitted signal and background.

deviations between the two methods are used as systematic errors in the subsequent analysis.

7.2.2 Fit to the Missing Mass Distribution

The $K^\pm\pi^\mp$ missing mass spectrum shows, whether in the $p\bar{p}$ annihilation the golden events are produced. For the golden events the missing mass should be in agreement with neutral kaon mass. Therefore a fit to the missing mass spectrum allows an estimation of the amount of golden events and contribution of background events. The fit is performed before applying the cut on the $K^\pm\pi^\mp$ missing mass.

However, using only the $K^\pm\pi^\mp$ missing mass we cannot distinguish all the channels, because of lack of information about the K^o decay. For example the $K^o \rightarrow \pi^o\pi^o\pi^o$ signal events give the same missing mass distribution as the background events $K^o \rightarrow \pi^o\pi^o$. Therefore in addition some lifetime information must be used to separate the channels giving the same missing mass spectrum.

In the three lifetime intervals $([-20, -10]\tau_S, [-10, 0]\tau_S$ and $[0, 20]\tau_S)$ the $K^\pm\pi^\mp$ missing mass spectra are fitted using the reference distributions corresponding to:

- $p\bar{p} \rightarrow K^\mp\pi^\pm K^o(\bar{K}^o), \quad K^o \rightarrow 3\pi^o/2\pi^o$ obtained from Monte Carlo simulation
- $p\bar{p} \rightarrow \pi^o + K^\mp\pi^\pm K^o(\bar{K}^o), \quad K^o \rightarrow 3\pi^o/2\pi^o$ obtained from Monte Carlo simulation
- $p\bar{p} \rightarrow \pi^+\pi^-\pi^0$ obtained from fits of the energy deposited in the inner scintillator.

Hence, in each lifetime interval we obtain the amount of golden and golden+ π^o events. The amount of pionic annihilation background is fixed in the fit. The relative proportion of events from the same channel in the three lifetime intervals is taken from the Monte Carlo simulation. This allows one to separate the channels giving the same missing mass spectra. The results of the missing mass fits are shown in figure 7.12 and summarized in the second column of table 7.1. They agree well with the results of the lifetime fit.

The lifetime spectra obtained from the Monte Carlo simulation are normalized using the signal and the background contributions obtained from the missing mass fit. Then the sum of the spectra is compared to the measured lifetime distribution (fig. 7.13). The lifetime distribution obtained from the fit agrees well with the measured spectrum.

The two methods of fitting the background levels using the lifetime and missing mass distributions are not completely independent, since both methods rely on the description of the lifetime distribution by the Monte Carlo simulation.

The two methods can be combined into one simultaneous fit of the missing mass and the lifetime distributions. The results of the combined fit, listed in the third column of table 7.1, lies in between the results of the two previous fits. In the analysis of CP violation effects we use the mean signal and background contributions calculated as an average of the three methods presented (the fourth column of table 7.1).

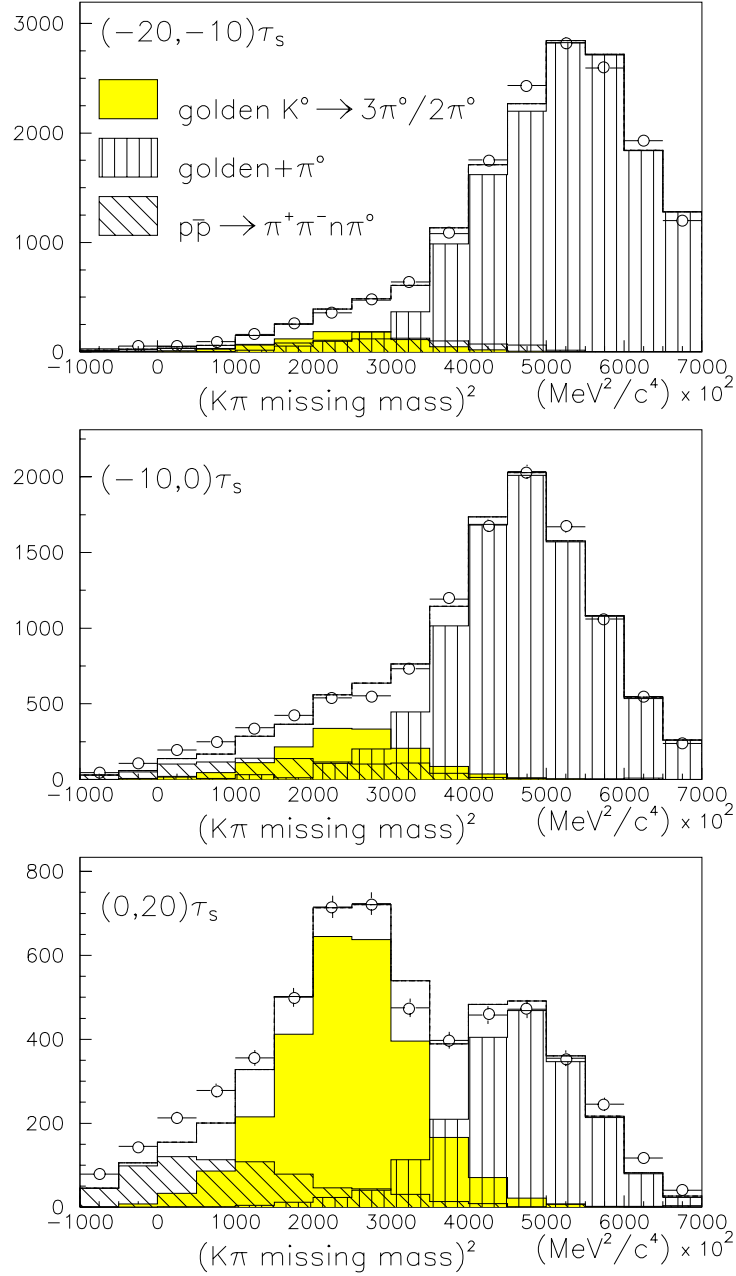


Figure 7.12: Fits to the $K^\pm \pi^\mp$ missing mass spectra in three lifetime intervals. The measured spectrum (points) is compared with the fit result (solid line). The contribution of golden events, the pionic background and the golden + π^0 background are shown.

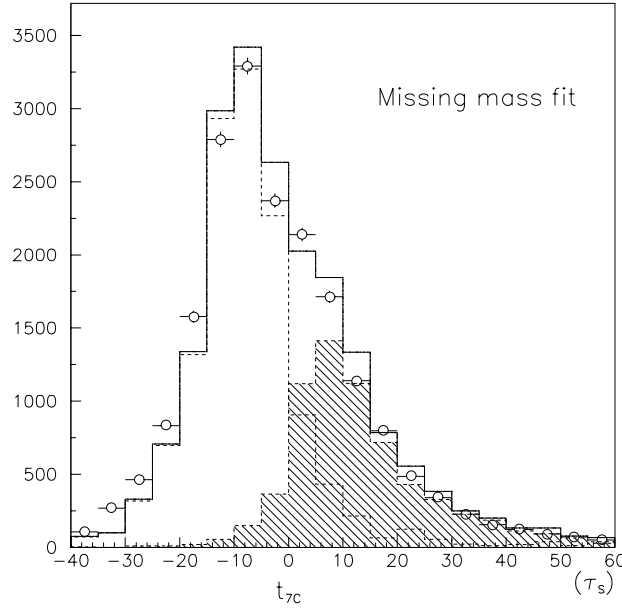


Figure 7.13: Lifetime distributions for signal (shaded area) and background (dashed line) obtained from the missing mass fits. Points indicates the measured lifetime spectrum and the solid line the sum of signal and background contributions.

From the background analysis we find, that in the lifetime region $[0 - 20] \tau_S$ there are ≈ 4300 signal events. A higher number of signal events, ≈ 8150 , was found in an independent analysis using different selection criteria [50].

7.3 Asymmetry

A limit on the CP violation parameter η_{ooo} in $K^o \rightarrow \pi^o \pi^o \pi^o$ decays is obtained from a fit of the lifetime dependent asymmetry. The asymmetry is obtained from the measured decay rates of initially pure K^o and \bar{K}^o states, ($R_{meas}^{ooo}(t)$ and $\bar{R}_{meas}^{ooo}(t)$), which are shown in figure 7.14:

$$A_{meas}^{ooo}(t) = \frac{\bar{R}_{meas}^{ooo}(t) - R_{meas}^{ooo}(t)}{\bar{R}_{meas}^{ooo}(t) + R_{meas}^{ooo}(t)} \quad (7.3)$$

The measured asymmetry $A_{meas}^{ooo}(t)$ is shown in figure 7.15. It does not show any lifetime dependence and the CP violation effects cannot be observed.

In the asymmetry fit the theoretical rates of initially pure K^o and \bar{K}^o states (sec. 3.3, eq. 3.43) are used as an input. The rates are corrected for acceptance and resolution effects (see eq. 6.4). The lifetime resolution and the shape of the lifetime dependent

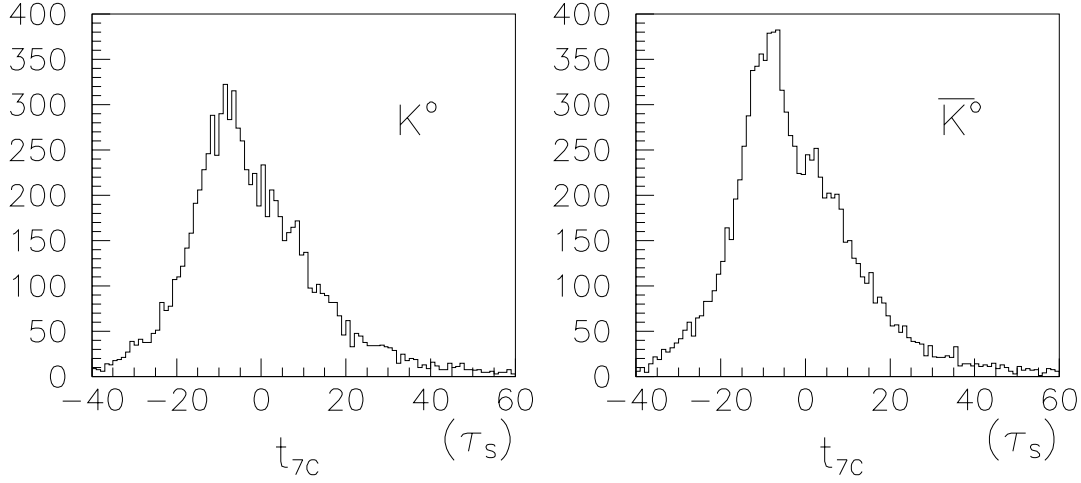


Figure 7.14: Measured decay rates of initially pure K^0 and \bar{K}^0 states.

acceptance are taken from the Monte Carlo simulation (fig. 7.16). The central lifetime resolution is of the order of $\approx 4 \tau_S$ (FWHM), however large tails can be seen. The acceptance is getting worse with increasing lifetime, because only the events with the K^0 decay vertex inside the calorimeter can be detected.

To the corrected K^0 and \bar{K}^0 lifetime distributions the background is added. We use the background contributions from table 7.1. The lifetime shapes of the background channels are parametrized by the different functions listed in table 7.2 and displayed in figure 7.17.

Channel	Parametrization
$p\bar{p} \rightarrow \pi^+ \pi^- n \pi^0$	exponential+constant
$K^0 \rightarrow \pi^0 \pi^0 \rightarrow 4\gamma + 2\gamma_{fake}$	exponential+exponential
$p\bar{p} \rightarrow \pi^0 + K^\mp \pi^\pm K^0(\bar{K}^0), \quad K^0 \rightarrow 3\pi^0$	gaussian+gaussian
$p\bar{p} \rightarrow \pi^0 + K^\mp \pi^\pm K^0(\bar{K}^0), \quad K^0 \rightarrow 2\pi^0$	exponential

Table 7.2: Parametrization of the lifetime dependence of the background channels.

The \bar{K}^0/K^0 normalization α is defined as the ratio of the events with a reconstructed \bar{K}^0 to the events with a reconstructed K^0 (sec. 6.7.1). The normalization is assumed to be the same for signal and background events, $\alpha_{bck} = \alpha$, except for the pionic annihilation background. For this particular background source, the normalization

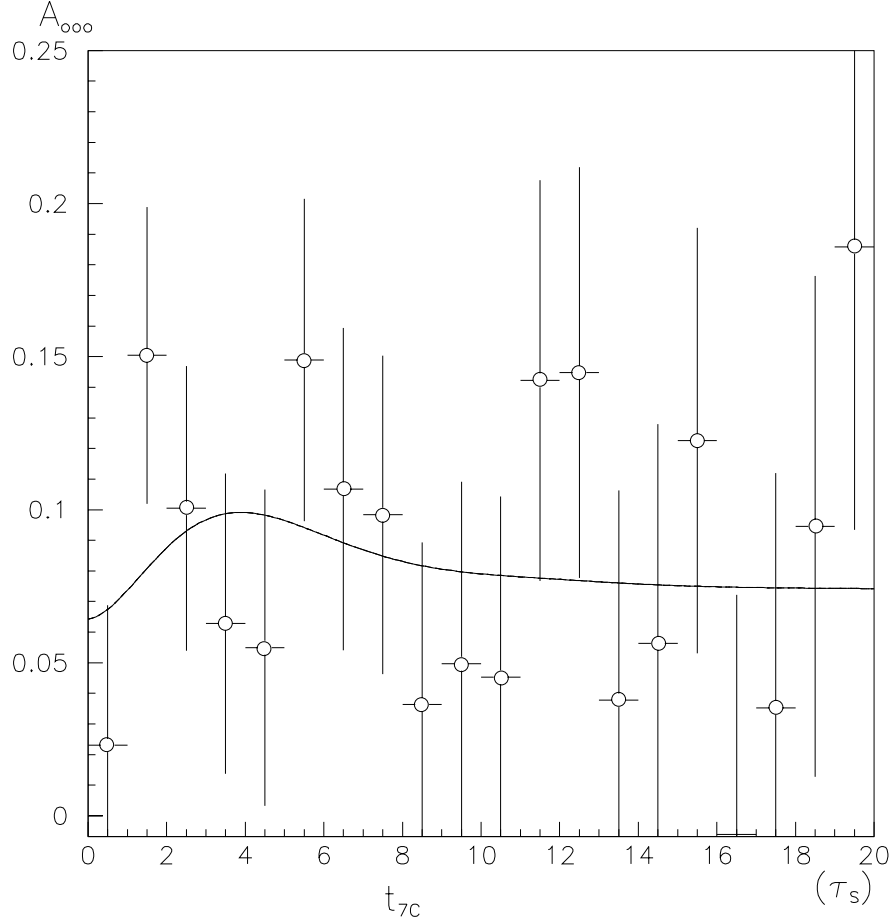


Figure 7.15: Measured lifetime dependent asymmetry $A_{meas}^{ooo}(t)$ together with the fitted function with free $\mathcal{R}e(\eta_{ooo})$ and $\mathcal{I}m(\eta_{ooo})$.

is defined by the dE/dx fits, namely the amount of pionic background is estimated separately for \overline{K}^0 and K^0 events. We find $\alpha_{\pi\pi} = 1.085 \pm 0.041$.

7.3.1 Fit Procedure

Due to the low number of collected events we use the maximum likelihood method for fitting the asymmetry. A method of fitting the ratio of two distributions using this method is described in [51, 37]. The likelihood of the fit to the binned K^0 and \overline{K}^0 rates is given by:

$$-\ln L = \sum_i N_i \ln R_i + \sum_i \overline{N}_i \ln \overline{R}_i \quad (7.4)$$

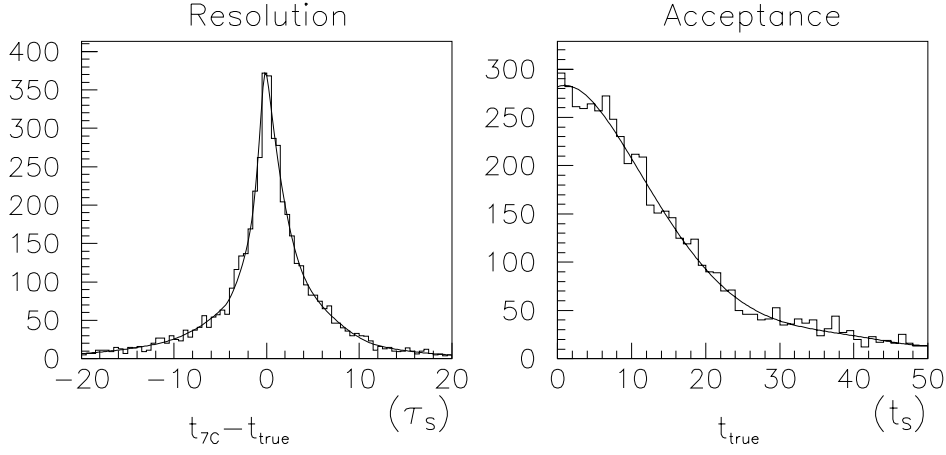


Figure 7.16: Distribution of the lifetime resolution ($\tau_{reconstructed} - \tau_{true}$) and its parametrization (left plot). The right plot shows the shape of the lifetime dependent acceptance. Both distributions are obtained from the Monte Carlo simulation.

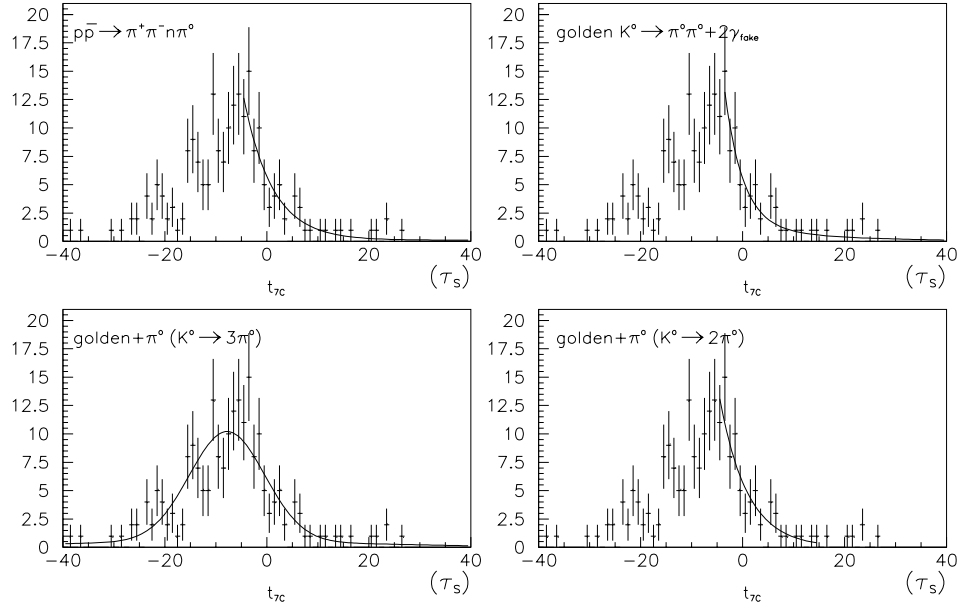


Figure 7.17: Parametrization of the background lifetime distributions.

where N_i and \bar{N}_i denote the number of entries in the i -th lifetime bin of the initially pure K^0 and \bar{K}^0 measured rates and R_i and \bar{R}_i are the theoretical functions describing the rates. The rates can be expressed by the asymmetry function $A_i = (\bar{R}_i - R_i)/(\bar{R}_i + R_i)$:

$$\begin{aligned} -\ln L &= \sum_i N_i \ln(1 - A_i) + \sum_i \bar{N}_i \ln(1 + A_i) \\ &+ \sum_i (N_i + \bar{N}_i) \ln\left(\frac{R_i + \bar{R}_i}{2}\right) \end{aligned} \quad (7.5)$$

The last term of the likelihood function $(\sum_i (N_i + \bar{N}_i) \ln(R_i + \bar{R}_i)/2)$ does not contain much information about CP violation parameters, but is sensitive to the acceptance effects which can introduce systematic uncertainties. Therefore it is omitted in the likelihood function.

7.3.2 Results of the Asymmetry Fit

The value of the CP violation parameter η_{ooo} obtained from the asymmetry fit (fig. 7.15) is:

$$\begin{aligned} \mathcal{R}e(\eta_{ooo}) &= 0.15 \pm 0.30 \\ \mathcal{I}m(\eta_{ooo}) &= 0.29 \pm 0.40 \end{aligned} \quad (7.6)$$

The normalization α is measured to be $\alpha = 1.16 \pm 0.06$. The correlation coefficient of $\mathcal{R}e(\eta_{ooo})$ and $\mathcal{I}m(\eta_{ooo})$ is $\varrho = 0.85$. Such a strong correlation is a result of the moderate lifetime resolution leading to a coupling of cosine and sine terms in the asymmetry formula (eq. 3.44).

Because of this strong correlation we can improve the statistical precision of the $\mathcal{I}m(\eta_{ooo})$ measurement by setting $\mathcal{R}e(\eta_{ooo}) = \mathcal{R}e(\varepsilon)$. We get:

$$\mathcal{I}m(\eta_{ooo}) = 0.12 \pm 0.20 \quad (7.7)$$

7.4 Systematic Errors

The following sources of systematic errors are considered:

1. Uncertainties in the amount of signal and background. The signal and background level variation is taken from the difference of the background levels obtained using the different fit methods (tab. 7.1). The variation of the signal and background contributions mentioned in the table means the absolute variation, i.e. 2% signal variation should be understood as a variation $(71.2 \pm 2.0)\%$.
2. Uncertainties in the parametrization of the background. Different functions are used to parametrize the lifetime shape of the background. The difference in the obtained values of η_{ooo} gives the systematic error arising from the parametrization procedure.

3. Normalization α of backgrounds. The normalization of the pionic background $\alpha_{\pi\pi}$ is varied by one standard deviation around the value obtained from the dE/dx fits. The normalization of events with fake showers (chapter 5) can also differ from the normalization of the signal events, therefore we vary the value of α_{fake} by 10% around the value of α obtained from the asymmetry fit.
4. The lifetime resolution obtained from Monte Carlo is used in the asymmetry fit. For the study of systematic errors we use the shape of the Monte Carlo resolution, but we scale the width of the distribution by 10%.

The systematic errors on $\mathcal{R}e(\eta_{ooo})$ and $\mathcal{I}m(\eta_{ooo})$ are summarized in table 7.3. The estimated systematic errors are much smaller than the statistical errors. Therefore the precision of the CPLEAR measurement of η_{ooo} is limited at present by the available number of reconstructed events.

Source	Variation	$\Delta(\mathcal{R}e \eta_{ooo})$	$\Delta(\mathcal{I}m \eta_{ooo})$
Signal/background contributions			
$K^0 \rightarrow \pi^0 \pi^0 \pi^0 \rightarrow 6\gamma$	$\pm 2.0\%$		
$K^0 \rightarrow \pi^0 \pi^0 \rightarrow 4\gamma + 2\gamma_{fake}$	$\pm 1.0\%$		
$p\bar{p} \rightarrow \pi^0 + K^\mp \pi^\pm K^0(\bar{K}^0), \quad K^0 \rightarrow 3\pi^0$	$\pm 1.0\%$		
$p\bar{p} \rightarrow \pi^0 + K^\mp \pi^\pm K^0(\bar{K}^0), \quad K^0 \rightarrow 2\pi^0$	$\pm 0.5\%$		
$p\bar{p} \rightarrow \pi^+ \pi^- n \pi^0$	$\pm 1.0\%$		
		± 0.005	± 0.012
Background shape	see text	$+0.011$	$+0.010$
		-0.000	-0.004
$K^0 \rightarrow \pi^0 \pi^0$ normalization α_{fake}	$\pm 10\%$	± 0.038	± 0.001
$p\bar{p} \rightarrow \pi^+ \pi^- n \pi^0$ normalization	± 0.041	± 0.008	± 0.006
Lifetime resolution	$\pm 10\%$	± 0.014	± 0.024

Table 7.3: Systematic errors on $\mathcal{R}e(\eta_{ooo})$ and $\mathcal{I}m(\eta_{ooo})$.

7.5 Conclusions

The analysis of $K^0 \rightarrow \pi^0 \pi^0 \pi^0$ decays demonstrates, that the CPLEAR experiment is able to fully reconstruct the events and to describe the observed data in terms of signal and background. The signal and background contributions estimated by various methods give a consistent picture. The final data sample contains ≈ 4300 signal events. In the lifetime region $[0, 20] \tau_S$ they constitute 70% of all the collected events and the

remaining 30% of events originate from the background channels. The following results are obtained:

$$\begin{aligned}\mathcal{R}e(\eta_{ooo}) &= 0.15 \pm 0.30 \text{ (stat)} \\ \mathcal{I}m(\eta_{ooo}) &= 0.29 \pm 0.40 \text{ (stat)}\end{aligned}\tag{7.8}$$

which are compatible with $\eta_{ooo} = 0$, i.e. no CP violation effects are observed. While fixing $\mathcal{R}e(\eta_{ooo}) = \mathcal{R}e(\varepsilon)$ we improve the statistical precision on the $\mathcal{I}m(\eta_{ooo})$ measurement:

$$\mathcal{I}m(\eta_{ooo}) = 0.12 \pm 0.20 \text{ (stat)}\tag{7.9}$$

Systematic errors are much smaller than statistical errors (tab. 7.3), therefore the measurement precision is at the present stage limited by the statistical errors and not by the systematic errors.

Already with the test sample of 1/4 of all events collected by the CPLEAR experiment we have reached the precision of the best other measurement of $\mathcal{I}m(\eta_{ooo})$ to date [5]. With all the collected data we expect to reduce the statistical error to:

$$\Delta\mathcal{I}m(\eta_{ooo}) \approx 0.1\tag{7.10}$$

with a fixed value of $\mathcal{R}e(\eta_{ooo})$. Further improvements in the analysis, especially more efficient background suppression, will be possible and improve the final results. The CPLEAR experiment will be able to provide a new upper limit on the CP violation effects in $K^0 \rightarrow \pi^0\pi^0\pi^0$ decays.

Chapter 8

Conclusions

CPLEAR is the first experiment in which CP violation has been observed as a time dependent rate asymmetry between the decays of initially pure \overline{K}^0 and K^0 into the $\pi^0\pi^0$ state. Two independent analyses observed the asymmetry using different methods of vertex reconstruction. The analysis of $K^0 \rightarrow \pi^0\pi^0$ decays using e^+e^- pairs from π^0 Dalitz decays and from photon conversions provides a better K^0 lifetime resolution than the standard method of vertex reconstruction with four photons detected in the calorimeter [4] ($0.2 \tau_S$ FWHM comparing to $0.7 \tau_S$ FWHM). A total of 88 000 events were reconstructed in the neutral kaon lifetime interval $[1 - 15] \tau_S$ using e^+e^- pairs and allowing the measurement of the phase φ_{00} of the CP violation parameter η_{00} :

$$\varphi_{00} = 62^\circ \pm 11^\circ(stat) \pm 2^\circ(syst) \quad (8.1)$$

The main technical difficulty of the method is the high background level which reduces the amplitude of the asymmetry. The background rejection is difficult due to the inclusive event reconstruction (remaining three photons are ignored). Various tools are developed and applied for the background suppression. The efficient rejection of background events allowed to reduce the amount of background down to a level of only 6% in the lifetime region $[1 - 15] \tau_S$.

The CPLEAR detector is designed with as little material as possible to minimize the effects of neutral kaon regeneration and multiple scattering. This design reduces the probability of photon conversion and explains the limited number of collected events and thus the size of the statistical uncertainty of φ_{00} .

Other analysis channels can also profit from the method of selecting the e^+e^- pairs and reconstructing their production vertices. In the measurement of the neutral kaon regeneration amplitudes the converted photons are used to obtain the position of the regenerator. The selected sample of e^+e^- pairs is also used to optimize the Neural Network performing the e/π separation. The separation is based on the Particle Identification Detector (PID) response and is used to select the $K^0 \rightarrow \pi e \nu$ events.

In the study of $K^0 \rightarrow \pi^0\pi^0\pi^0 \rightarrow 6\gamma$ decays we perform a complete event reconstruction using six photons detected in the calorimeter. We have presented methods of signal

and background estimation using the K^0 lifetime and the $K\pi$ missing mass distributions. These methods allowed us with just a test sample of 1/4 of all collected events to reach a precision equivalent to the best current measurement [5] by obtaining:

$$\mathcal{I}m(\eta_{ooo}) = 0.12 \pm 0.20 \text{ (stat)} \quad (8.2)$$

The systematic uncertainty is small compared to the statistical error, therefore the precision of the CPLEAR measurement is limited at present by the available number of events. After processing all the remaining collected events, the CPLEAR experiment will reach a precision of $\Delta\mathcal{I}m(\eta_{ooo}) \approx 0.1$ and improve the present upper limit on $\mathcal{I}m(\eta_{ooo})$. This result will give a better limit on the direct CP violation in the $K^0 \rightarrow \pi^0\pi^0\pi^0$ decays, since direct CP violation affects only $\mathcal{I}m(\eta_{ooo})$.

Our result is important for the present and future CPT tests comparing φ_{+-} with the superweak phase φ_{SW} , where the present limit of $\mathcal{I}m(\eta_{ooo})$ is a source of large uncertainty.

Appendix A

Dalitz Decays of the Neutral Pions

The neutral pion decays into two photons with a probability of nearly 99%. However, with a probability of approximately 1.2% an e^+e^- pair and one photon are produced. The second decay mode, called a Dalitz decay, is also a pure electromagnetic process. In this decay one real and one virtual photon are produced. The latter undergoes an internal conversion and decays into electron and positron [52] (fig. A.1). Compared to the π^0 decay into two photons the process is suppressed by the electromagnetic coupling constant. Since the mass of the virtual photon γ^* is small, a small opening angle between the e^+ and e^- is expected.

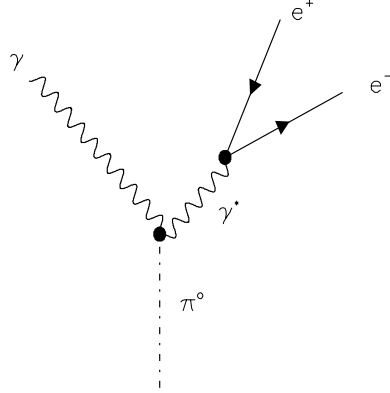


Figure A.1: Dalitz decay $\pi^0 \rightarrow e^+e^-\gamma$ in the QED lowest order.

In describing the differential decay rate, it is common to introduce two kinematical variables:

$$\begin{aligned} x &= \frac{1}{m_{\pi^0}^2}(q_1 + q_2)^2 \\ y &= \frac{2p \cdot (q_1 - q_2)}{m_{\pi^0}^2(1 - x)} \end{aligned} \tag{A.1}$$

where q_1 , q_2 and p are the four momenta of the electron, the positron and the neutral pion respectively. The variable x corresponds to the ratio of the virtual photon mass to the neutral pion mass, while y measures the energy distribution between the electron and the positron. The latter can be easily seen by expressing y in the π^0 rest frame:

$$y = \frac{E_1^{cm} - E_2^{cm}}{|\vec{q}_1^{cm} + \vec{q}_2^{cm}|} \quad (\text{A.2})$$

The differential decay rate of the Dalitz decays expressed by the variables x and y is given in QED lowest order by [53]:

$$\frac{1}{\Gamma(\pi^0 \rightarrow \gamma\gamma)} \frac{d\Gamma(\pi^0 \rightarrow \gamma e^+ e^-)}{dx dy} = \frac{\alpha}{\pi} |f(x)|^2 \frac{(1-x)^3}{4x} \left(1 + y^2 + \frac{r^2}{x}\right) \quad (\text{A.3})$$

where $r = 2m_e/m_\pi^0$ and $f(x)$ is the electromagnetic form factor of the neutral pion, which is independent of y . The form factor can be parametrized as:

$$f(x) = 1 + ax \quad (\text{A.4})$$

The slope a is measured to be $a = 0.032 \pm 0.004$ [19].

The function obtained after integration of equation A.3 over y reflects the mass distribution of the virtual photon. It is given by:

$$\frac{1}{\Gamma(\pi^0 \rightarrow \gamma\gamma)} \frac{d\Gamma(\pi^0 \rightarrow \gamma e^+ e^-)}{dx} = \frac{\alpha}{\pi} |f(x)|^2 \frac{2(1-x)^3}{3x} \beta \left(1 - \frac{r^2}{2x}\right) \quad (\text{A.5})$$

with $\beta = \sqrt{1 - r^2/x}$. The distribution is shown in figure A.2. The mass of the virtual photon is typically small, the photon is nearly real. From equation A.5 follows that about half of the e^+e^- pairs have an opening angle below 18° in the π^0 rest frame.

In the CPLEAR experiment neutral pions originating from K^0 decays have typically a momentum of approximately $300 \text{ MeV}/c$. Due to the Lorentz boost in the laboratory frame, the e^+e^- opening angle becomes smaller than in the π^0 rest frame (fig. A.3). Therefore in the reconstruction procedure of the e^+e^- vertex the opening angle is assumed to be zero.

Due to the smallness of x , the real photon takes an energy approximately equal to half of the neutral pion mass, namely:

$$E_\gamma = \frac{1}{2}m_{\pi^0}(1-x) \simeq \frac{1}{2}m_{\pi^0} \quad (\text{A.6})$$

The $d\Gamma/dy$ distribution is relatively flat (fig. A.2). Therefore, in general, positron and electron have different energies and no constraint concerning the e^+ and e^- energies can be applied while reconstructing the e^+e^- vertex.

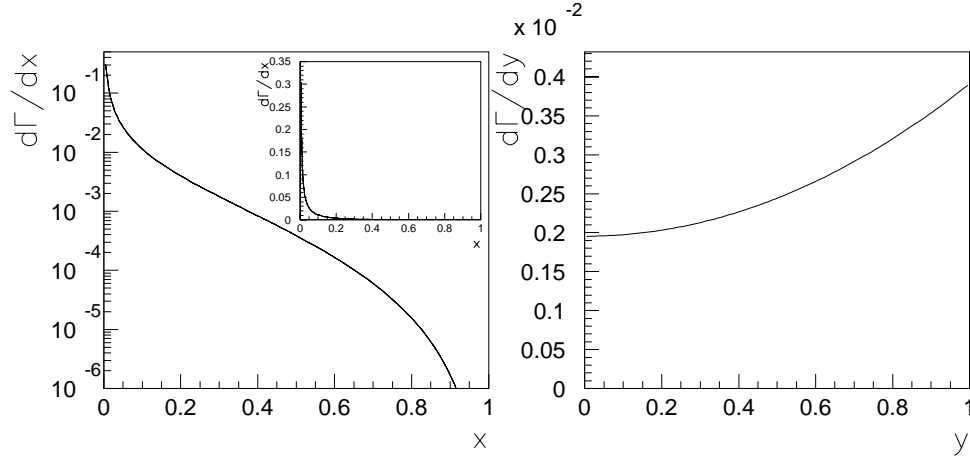


Figure A.2: The differential decay rates $d\Gamma/dx$ and $d\Gamma/dy$ of the Dalitz decays $\pi^0 \rightarrow e^+e^-\gamma$. The small plot shows $d\Gamma/dx$ in the linear scale.

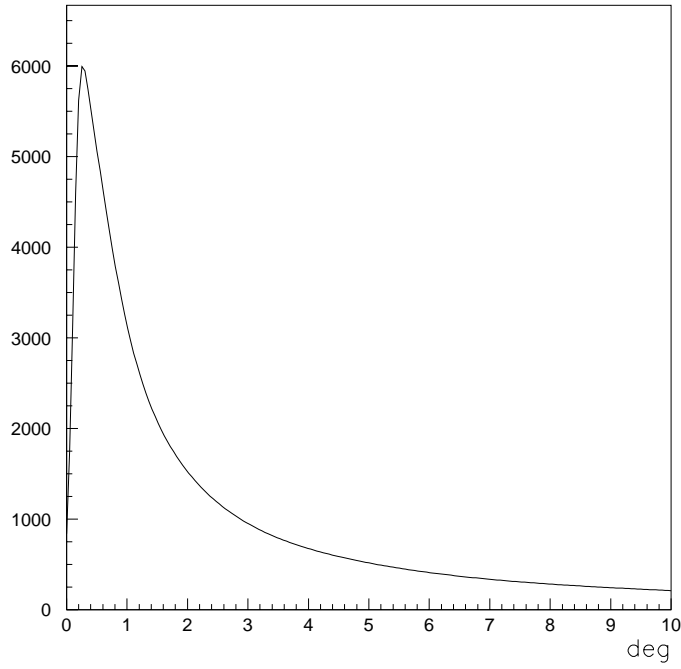


Figure A.3: The theoretical electron-positron opening angle distribution in the lab-system for Dalitz decays of neutral pions, which are produced in the reaction $p\bar{p} \rightarrow K^\mp \pi^\pm K^0(\bar{K}^0)$, $K^0 \rightarrow \pi^0 \pi^0$ at CPLEAR.

Appendix B

Photon Conversion

Pair production is the most important electromagnetic process at high energies by which photons interact with matter [54]. The intense electric field near the nucleus can cause a photon to convert into an electron and a positron. The nucleus must be there to satisfy conservation of momentum, but the energy transfer to the nucleus is typically small. Therefore the e^+e^- opening angle is also small.

Let the incident photon has an energy k and the created electron (positron) an energy $E_-(E_+)$, so that $k \approx E_+ + E_-$. We define also the energy ratios $w_{\pm} = E_{\pm}/k$. The differential cross section for the production of a positron with energy between E_+ and $E_+ + dE_+$ is given by [55]:

$$\frac{d\sigma}{dE_+} = \frac{4\sigma_o}{k} \left[\left(w_+^2 + w_-^2 + \frac{2}{3}w_+w_- \right) \ln \left(\frac{183}{Z^{1/3}} \right) - \frac{1}{9}w_+w_- \right] \quad (\text{B.1})$$

where Z is the atomic number of the nucleus, σ_o is defined as $\sigma_o = \alpha Z^2 r_e^2$ and r_e denotes the classical electron radius. The cross section is fairly uniform (fig. B.1) as a function of positron energy. The positrons are likely to be produced at any allowed energy. In general, the electron and the positron do not have the same energy.

At high photon energies, positron and electron tend to be produced at small opening angles. The mean production angle of an electron or positron with respect to the incident photon direction is [55]:

$$\Theta = \frac{m_e c^2}{E} \quad (\text{B.2})$$

where E is the electron or positron energy. In the energy range of a typical electron or positron in CPLEAR ($\approx 100 \text{ MeV}$) the mean production angle is $\Theta \approx 0.3^\circ$. The electron and the positron are nearly collinear.

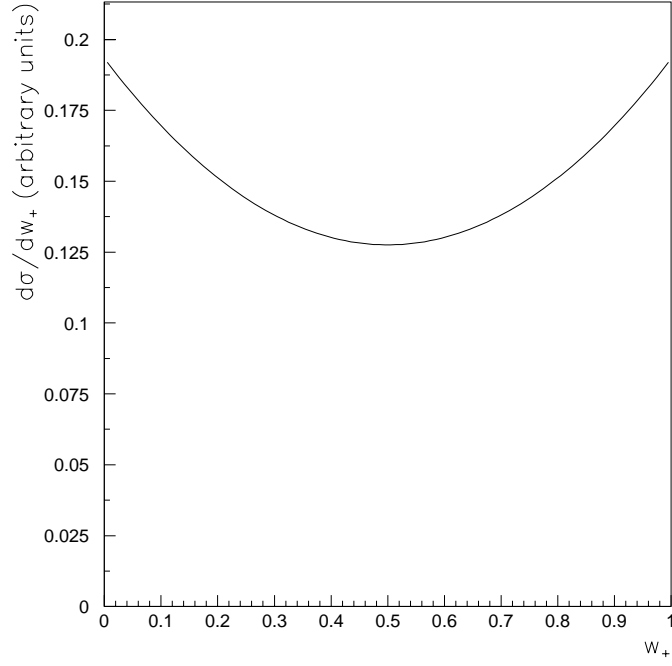


Figure B.1: The differential cross section for photon conversion $d\sigma/dw_+$.

The total cross section for the e^+e^- pair production is obtained by integrating eq. B.1 over all possible positron energies. For photon energies $k \gg 137mc^2 Z^{-1/3}$ it approaches the asymptotic value:

$$\sigma_{e^+e^-} = 4\sigma_o \left[\frac{7}{9} \ln(183 Z^{-1/3}) - \frac{1}{54} \right] \quad (\text{B.3})$$

In the asymptotic limit the cross section is approximately proportional to Z^2 and independent of the incident photon energy.

Appendix C

Theory of Fits with Constraints

The aim of a constrained fit is to deduce unknown quantities, their errors and correlations from a given set of measured variables and their measurement errors by the use of constraints, which are functions of the measured and unknown variables [56]. An example is a 1C-fit (sec. 6.1.2) in which from the measured momenta of the charged kaon and pion the unknown neutral kaon momentum is deduced. It is required, that the sum of the momenta of all three particles adds up to zero and their energies to two proton masses.

Let η be a vector of N observables for which we have the first approximation values, namely measurements y , with errors contained in the covariance matrix $V(y)$. In addition we have a set of J not measured variables ξ which we want to reconstruct. The true values of the observables η , which are not falsified by the measurement errors, and unmeasurable variables ξ are related by a set of K constraint equations:

$$f_k(\eta, \xi) = 0 \quad k = 1, \dots, K \quad (\text{C.1})$$

The number of degrees of freedom:

$$I_{ndf} = K - J \quad (\text{C.2})$$

must be greater or equal zero in order to allow a calculation of the unknown variables ξ out of the measurements y with the precision given by the measurement errors.

The constrained fit procedure requires the minimization of a χ^2 function which is delivered as:

$$\chi^2(\eta) = (y - \eta)^T \cdot V^{-1}(y) \cdot (y - \eta) \quad (\text{C.3})$$

while all the constraints (eq. C.1) are fulfilled. This requires the overconstrained set of equations, i.e. $I_{ndf} > 0$. The minimization gives the unknown variables ξ and also derives improved estimates of the measured values y .

In general the problem presented here can be solved by eliminating K unknowns from the equation C.1, substituting them in the χ^2 equation (eq. C.3) and minimizing this function. However, we have no prescription which variables should be eliminated

from the constraint equations. In addition the actual minimization of the χ^2 function can develop differently depending on the elimination made. To avoid these problems the method of Lagrange multipliers is usually applied, namely the minimization of the χ^2 function defined as:

$$\chi^2(\eta, \xi, \lambda) = (y - \eta)^T \cdot V^{-1}(y) \cdot (y - \eta) + 2 \sum_k \lambda_k f_k(\eta, \xi) \quad (\text{C.4})$$

where λ_k represents K additional unknowns called Lagrange multipliers.

Now we have in total $N + J + K$ unknowns. The minimization explicitly requires, that all the derivatives of $\chi^2(\eta, \xi, \lambda)$ with respect to all unknowns are equal to zero:

$$\begin{aligned} \frac{\partial \chi^2(\eta, \xi, \lambda)}{\partial \eta} &= -2V^{-1}(y - \eta) + 2F_\eta^T \lambda = 0 \\ \frac{\partial \chi^2(\eta, \xi, \lambda)}{\partial \xi} &= 2F_\xi^T \lambda = 0 \\ \frac{\partial \chi^2(\eta, \xi, \lambda)}{\partial \lambda} &= 2f(\eta, \xi) = 0 \end{aligned} \quad (\text{C.5})$$

where the F_η and F_ξ are defined as:

$$(F_\eta)_{ki} = \frac{\partial f_k(\eta, \xi)}{\partial \eta_i} \quad , \quad (F_\xi)_{kj} = \frac{\partial f_k(\eta, \xi)}{\partial \xi_j} \quad (\text{C.6})$$

The constraint equation $f(\eta, \xi) = 0$ is here explicitly recovered by the $\partial/\partial\lambda$ differentiation in equation C.5. The function $\chi^2(\eta, \xi, \lambda)$ is minimized in an iterative way, producing successively better approximations.

In the minimum the χ^2 function follows the χ^2 distribution if the fit hypothesis is fulfilled:

$$P_\chi(\chi^2, I_{ndf}) = \frac{(\chi^2)^{\frac{I_{ndf}}{2}-1} \exp^{-\frac{\chi^2}{2}}}{2^{\frac{I_{ndf}}{2}} \Gamma(\frac{I_{ndf}}{2})} \quad (\text{C.7})$$

The expected value of the χ^2 -distribution is:

$$\langle P_\chi(\chi^2, I_{ndf}) \rangle = I_{ndf} \quad (\text{C.8})$$

For each event a probability can be calculated from the χ^2 value in the minimum:

$$Prob(\chi_{min}^2, I_{ndf}) = \int_{\chi_{min}^2}^{\infty} P_\chi(z, I_{ndf}) dz \quad (\text{C.9})$$

The probability obtained for a given event shows how well it fulfills the criteria given by the constraints. This makes the constrained fits a useful tool for background suppression.

Appendix D

Reconstruction of the e^+e^- Vertex

We describe in detail the method of e^+e^- vertex reconstruction. Before we should get familiar with the parametrization of the charged particle tracks in a magnetic field using helix parameters.

Track Parametrization - Helix Parameters

The track of a charged particle in a uniform magnetic field follows a helical trajectory with an axis parallel to the magnetic field. Such a curve can be described using five independent parameters. The parameters chosen are the following (fig. D.1):

- ϵ : distance in the $X - Y$ plane between the origin of the coordinate system and the point $P_o(X_o, Y_o, Z_o)$ of the closest approach of the track. The sign of the parameter ϵ is chosen in such a way that for a magnetic field \vec{B} parallel to the Z-axis and a positively charged particle ϵ is positive if the origin of the coordinate system lays inside the circle obtained by projecting the track on the $X - Y$ plane.
- θ_T : angle between the X-axis and the track direction at the point of the closest approach to the origin of the coordinate system.
- C : curvature of the track ($1/R$). The sign is given by the charge of the particle.
- $\tan(\lambda)$: tangent of the angle between the total momentum \vec{P} of the particle and its transversal projection.
- Z_o : the Z component of the point $P_o(X_o, Y_o, Z_o)$ of the closest approach of the track to the origin of the coordinate system.

Let b be the distance on the X-Y plane between the charged track and the origin of the coordinate system, R the radius of the helix on the X-Y plane and θ_o the angle between the line connecting the origin of the coordinate system with the center of the

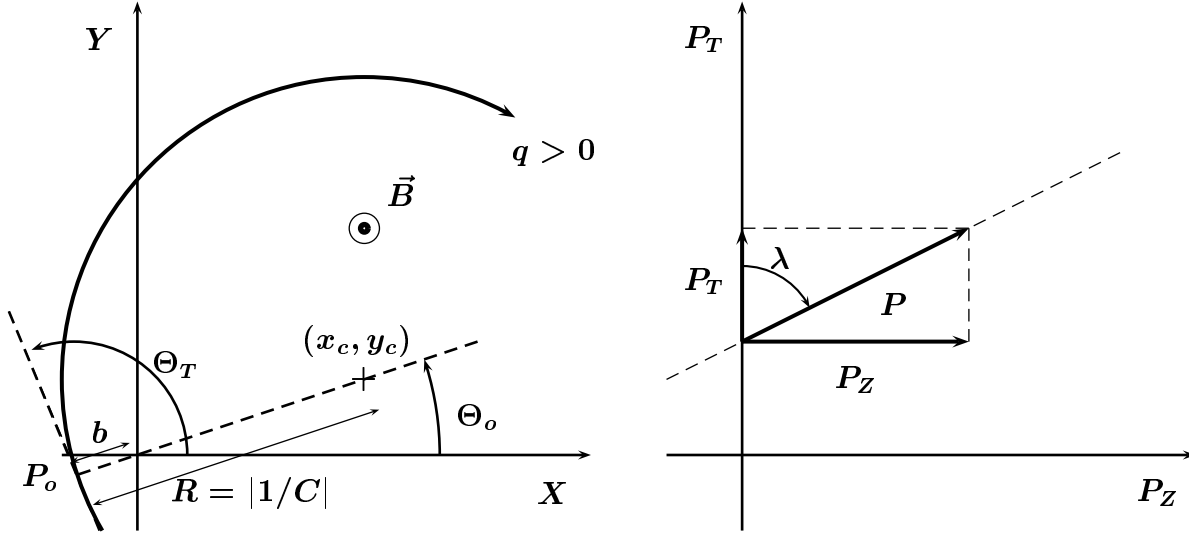


Figure D.1: Representation of the parameters describing a helix. x_c and y_c denote the coordinates of the center of the circle.

circle and the X-axis (see fig. D.1). The first three parameters of the helix can be expressed by the above parameters using the following formulas:

$$\begin{aligned}
 \epsilon &= q \cdot \text{sign}(B) \cdot b \\
 C &= \frac{q}{R} \\
 \theta_T &= \theta_o + \frac{\pi}{2}q
 \end{aligned}
 \tag{D.1}$$

where q is the sign of the charge of the particle and B the magnetic field.

Some kinematical variables can be easily obtained out of the helix parameters. The transversal and longitudinal momentum components of a particle are given by:

$$\begin{aligned}
 P_T &= \frac{B}{qC} \\
 P_z &= \frac{B}{qC} \tan \lambda \\
 P &= \sqrt{P_T^2 + P_z^2} = \frac{B}{qC |\cos \lambda|}
 \end{aligned}
 \tag{D.2}$$

e^+e^- Vertex

In the vertex reconstruction procedure, the e^+e^- vertex on the X-Y plane is found first. The center of the circle, obtained by projecting the helix on the X-Y plane, can

be derived using the formulas (fig. D.1):

$$\begin{aligned} x_c &= (R + b) \cos \theta_o = (1/C + \epsilon) \sin \theta_T \\ y_c &= (R + b) \sin \theta_o = -(1/C + \epsilon) \cos \theta_T \end{aligned} \quad (D.3)$$

The reconstructed vertex lies on the line connecting the centers of the circles formed by the tracks (fig. 6.6). The distance of a vertex point to the center of each circle is proportional to the radius of the respective circle. So, the reconstructed X and Y coordinates of the conversion vertex are given by the formulas:

$$\begin{aligned} x_{vertex} &= \frac{|C_1|}{|C_1| + |C_2|} x_{c1} + \frac{|C_2|}{|C_1| + |C_2|} x_{c2} \\ y_{vertex} &= \frac{|C_1|}{|C_1| + |C_2|} y_{c1} + \frac{|C_2|}{|C_1| + |C_2|} y_{c2} \end{aligned} \quad (D.4)$$

where indices 1 and 2 point to the first and the second track.

The Z coordinate of the vertex point is the average of the Z components of both tracks at the point of the closest approach to the vertex. Let β be the angle between the line connecting the centers of both helices and the X-axis:

$$\tan \beta = \frac{y_{c2} - y_{c1}}{x_{c2} - x_{c1}} \quad (D.5)$$

The angle θ_V is the angle the particle has to traverse from the point $P_o(X_o, Y_o, Z_o)$ (where the Z component is given by the Z_o parameter) to the point closest to the reconstructed vertex. This angle is given for each track by the formulas:

$$\begin{aligned} \theta_{V1} &= \theta_{T1} - \beta + \pi/2 \cdot \text{sign}(C_1) \pm 2n_1\pi \\ \theta_{V2} &= \theta_{T2} - (\beta - \pi) + \pi/2 \cdot \text{sign}(C_2) \pm 2n_2\pi \end{aligned} \quad (D.6)$$

where the indices denote the first and the second track and n is an integer number. The Z components of the points of the closest approach to the vertex are given by:

$$\begin{aligned} Z_1 &= Z_{o1} + \frac{\tan \lambda_1}{C_1} \theta_{V1} \\ Z_2 &= Z_{o2} + \frac{\tan \lambda_2}{C_2} \theta_{V2} \end{aligned} \quad (D.7)$$

The ambiguity in finding these parameters is solved by choosing such an n (eq. D.6) that the difference between Z_1 and Z_2 is the smallest possible. Then the Z coordinate of a e^+e^- vertex is found as an average of the two Z_1 and Z_2 coordinates given in the previous equation:

$$Z_{vertex} = \frac{Z_1 + Z_2}{2} \quad (D.8)$$

Acknowledgments

Completion of this thesis is a consequence of the help and advice of many people. I can only name few of them.

I would like to thank to my supervisor Professor Hans-Jürg Gerber for giving me the opportunity to carry out this research, for his constant support and guidance.

I would also like to express my thanks to all the members of the CPLEAR collaboration who helped me to get in touch with the neutral kaon physics.

Special thanks to Dr. Thomas Ruf with whom I worked together at the analysis of $K^0 \rightarrow \pi^0\pi^0$ decays. Many thanks to Dr. Bernd Pagels for his help and fruitful collaboration at the CP violation search in the $K^0 \rightarrow \pi^0\pi^0\pi^0$ decays and for his valuable criticism and helpful comments on my thesis. I would also like to thank Dr. Peter Weber for reading my thesis and giving me many valuable remarks and comments, which helped to improve the thesis.

Grateful thanks to Olaf Behnke for the valuable discussions which helped me to understand better the physics at CPLEAR.

Special thanks to Andrew Cody for correcting my written English throughout this thesis.

I gratefully acknowledge the support from the CPLEAR collaboration during my stay at CERN, for which I thank to its spokesman Professor Panagiot Pavlopoulos.

Bibliography

- [1] J.H.Christenson, J.W.Cronin, V.L.Fitch, R.Turlay, Phys.Rev.Lett 13, 138 (1964)
- [2] For a description of the B -meson system see for example:
I.I.Bigi et al., *CP violation*, ed. C.Jarlskog, World Scientific, Singapore 1989;
D.Wyler, *Proc. of the Second International Workshop on B-Physics at Hadron Machines*, Le Mont-Saint-Michel, 1994, ed. P.Schlein, Nucl. Inst. Meth. A 351 (1994) 8
- [3] E.Gabathuler, P.Pavlopoulos in *Proc. Workshop on Physics at LEAR*, Erice (1982); ed. U.Gastaldi, R.Klapisch, New York, Plenum (1982);
L.Adiels et al., CERN/PSCC/85-6 P82 (1985);
L.Adiels et al., CERN/PSCC/86-34 M263 (1986)
- [4] R.Adler et al., Z. Phys. C70, 211 (1996)
- [5] V.V.Barmin et al., Phys. Lett. B128 129 (1983)
- [6] E.Noether, Nachr. Ges. Wiss. Göttingen, 171 (1918)
- [7] T.D.Lee, C.N.Yang, Phys. Rev. 104, 254 (1956)
- [8] C.S.Wu et al., Phys. Rev. 105, 1413 (1957)
- [9] R.L.Garwin, L.M.Lederman, M.Weinrich, Phys. Rev. 105, 1415 (1957)
- [10] J.I.Friedman, V.L.Telegdi, Phys. Rev. 105, 1681 (1957)
- [11] L.Landau, Nucl. Phys. 3, 127 (1957)
- [12] M.Gell-Mann, A.Pais, Phys. Rev. 97, 1387 (1955)
- [13] M.Bardon et al., Ann. Phys. NY 5, 156 (1958)
- [14] D.Neagu et al., Phys. Rev. Lett. 6, 552 (1961)
- [15] G.Lüders, Ann. Phys. 2, 1 (1957);
W.Pauli, *Niels Bohr and the Development of Physics*, ed. W.Pauli, p.30, Oxford, Pergamon (1955);
R.Jost, Helv. Phys. Acta 31, 263 (1958)

- [16] See for example:
S.Hawking, Comm. Math. Phys. 87, 395 (1982);
R.Wald, Phys. Rev. D21, 2742 (1980);
J.Ellis, N.E.Mavromatos, D.V.Nanopoulos, Phys. Lett. B293, 37 (1992);
J.Ellis, N.E.Mavromatos, D.V.Nanopoulos, Phys. Lett. B293, 142 (1992)
- [17] R.Adler et al., Phys. Lett. B364, 239 (1995)
- [18] L.Leprince-Ringuet, M.L'héritier, J.Phys. Radium 7, 66 (1946);
G.D.Rochester, C.C.Butler, Nature 160, 855 (1947)
- [19] Particle Data Group, Phys. Rev. D50 (1994)
- [20] V.Weisskopf, E.Wigner, Z. Phys. 63, 54 (1930)
- [21] T.D.Lee, K.Oehme, C.N.Yang, Phys. Rev. 106, 340 (1957)
- [22] T.Nakada, *Review on CP Violation*, AIP Conf. Proc. no 302 (1993)
- [23] C.P.Enz, R.R.Lewis, Helv. Phys. Acta 38, 860 (1965)
- [24] T.J.Dewlin, J.O.Dickey, Rev. Mod. Phys. 51, 237 (1979)
- [25] H.T.Cheng, Phys. Lett. B315, 170 (1993)
- [26] L.Lavoura, Mod. Phys. Lett. A15, 1367 (1992)
- [27] For a review of K^0 regeneration see:
K.Kleinknecht, Fortschritte der Physik 21, 57 (1973)
- [28] M.L.Good, Phys. Rev. 106, 591 (1957)
- [29] M.Kobayashi, K.Maskawa, Prog. Theor. Phys. 49, 652 (1973)
- [30] C.Jarlskog, Phys. Rev. Lett. 55, 1039 (1985);
C.Jarlskog, Z. Phys. C29, 491 (1985)
- [31] L.Wolfenstein, Phys. Rev. Lett. 13, 562 (1964)
L.Wolfenstein, Ann. Rev. Nucl. Part. Sci. 36, 137 (1986)
- [32] R.Adler et al., CERN-PPE/96-27 (1996), submitted to Nucl. Instrum. Methods A.
- [33] P.Bloch, J.Derre, A.Angelopoulos, C.Guyot, *CPREAD Guide*, CPLEAR Internal Note (1991)
- [34] CP Offline Group, *CPGEANT User Manual*, CPLEAR note (1993)
- [35] R.Adler et al., Phys. Lett. B363, 243 (1995)

- [36] C.Felder, *Erste Resultate zum Zerfall $K_S, K_L \rightarrow \pi^+\pi^-\pi^0$ des CPLEAR-Experiments*, Ph.D. Thesis, Basel Univ. (1993)
- [37] O.Behnke, *Erste Messung einer Teilchen-Antiteilchen Asymmetrie in den Zerfällen neutraler Kaonen nach $\pi^0\pi^0$* , Ph.D. Thesis, ETH Zürich, (in preparation)
- [38] G.Polivka, *Energy Calibration of the Calorimeter*, CPLEAR Internal Note (1993)
- [39] T.Ruf, *Analysis of the $\pi^0\pi^0$ channel using Dalitz decays and converted photons*, CPLEAR Internal Note (1993)
- [40] S.Brandt, *Statistical and computational methods in data analysis*, second edition, North-Holland (1976)
- [41] S. Wolfram, *Mathematica, A System for Doing Mathematics by Computer* second edition (1991)
- [42] B.Pagels, *Private communication*
- [43] W.Fetscher, P.Kokkas, P.Pavlopoulos, Th.Ruf, Th.Schietinger, *Regeneration of arbitrary coherent neutral kaon states: a new method for measuring the $K^0 - \bar{K}^0$ forward scattering amplitude*, (in preparation)
- [44] R.Adler et al., Phys. Lett. B363, 237 (1995)
- [45] R.Adler et al., Phys. Lett. B369, 367 (1995)
- [46] C.Begon, *Localisation of Material Structures in the CPLEAR Detector through the Study of Photon Conversion Events*, CPLEAR Internal Note (1995)
- [47] M.Dejardin, *Electron-Pion Separation using Neural Network technique with PID informations*, CPLEAR Internal Note (1993)
- [48] B.Pagels, O.Behnke, H.-J.Gerber, ETHZ-IPP Internal Report 95-4 (1995); B.Pagels, *Messung und Rekonstruktion des Zerfalls $K_S^0(K_L^0) \rightarrow \pi^0\pi^0$ durch das CP-LEAR Experiment*, Ph.D. Thesis, Basel Univ. (1992); B.Pagels, *Neutral Vertex Reconstruction Package VXFIT - User Manual*, CPLEAR Internal Note (1993)
- [49] M.Schäfer, *Private communication*
- [50] M.Schäfer, *Status Report: Reconstruction of the Decay $K_L^0 \rightarrow \pi^0\pi^0\pi^0$* , CPLEAR Internal Note (1994)
- [51] R.Barlow, P.Hinde, Comput. Phys. Commun. 56, 328 (1990)
- [52] R.H. Dalitz, Proc. Phys. Soc. London, Sect. A 64, 667 (1951)
- [53] N.M.Kroll, W.Wada, Phys. Rev. 98, 1355 (1955)

- [54] For a description of the photon interactions with matter see for example:
R.C.Fernov, *Introduction to Experimental Particle Physics*, Cambridge University Press (1986)
- [55] H.Bethe, J.Ashkin, *Passage of Radiation through Matter*, in *Nuclear Physics*, ed. E.Segrè, Vol. 1, New York, John Willey and Sons (1953)
- [56] V.Blobel in *Formulae and Methods in Experimental Data Evaluation*, ed. R.K.Bock et al., European Physical Society (1984)

List of Figures

2.1	C , P and CP transformation applied to a left-handed neutrino.	7
3.1	Wu-Yang diagram showing the dependencies between the CP violation parameters.	17
3.2	Decay rates of the initially pure K^o ($R_{\pi\pi}(t)$) and \overline{K}^o ($\overline{R}_{\pi\pi}(t)$) states into two pions.	19
3.3	Lifetime dependent asymmetry $A_{\pi\pi}(t)$	19
3.4	Decay rates of the initially pure K^o and \overline{K}^o states into three neutral pions.	22
3.5	Lifetime dependent asymmetry $A_{ooo}(t)$ for the decays $K^o \rightarrow \pi^o\pi^o\pi^o$	22
3.6	Box diagrams describing the $K^o - \overline{K}^o$ oscillations.	23
3.7	Diagrams contributing to the $K^o \rightarrow 2\pi$ decays.	23
4.1	General layout of the CPLEAR detector.	27
4.2	The beam pipe, beam monitor and target layouts.	28
4.3	Section through part of a proportional chamber.	29
4.4	Schematic view of a drift chamber and details of the drift chamber geometry: a) drift cell, b) sense-wire doublet.	30
4.5	Layout of a streamer tube sector.	31
4.6	Relative resolution of the transverse momentum for charged tracks.	32
4.7	Cross-section of one of the particle identification detector segments.	32
4.8	Kaon identification efficiency as a function of momentum.	33
4.9	Probability of pion misidentification as a kaon presented as a function of pion momentum.	34
4.10	Energy loss in the inner scintillator by charged kaons and pions.	34
4.11	Time-of-flight difference between K and π for the whole accepted phase space of $p\overline{p} \rightarrow K^\mp\pi^\pm K^o(\overline{K}^o)$ events.	35
4.12	a) Transverse cross-section of the calorimeter. b) Geometrical setup of the layer of tubes sandwiched between two layers of pick-up strips.	36
4.13	Photon detection efficiency in the electromagnetic calorimeter as a function of the photon energy.	37
4.14	Logic and data flow diagram of the trigger system.	38
5.1	Multiplicity of neutral showers in $K^o \rightarrow \pi^+\pi^-$ data.	44

5.2	Squared distance between the track of a charged particle and the closest neutral shower.	45
5.3	Squared distance between the K^\pm track and the closest neutral shower.	46
5.4	Squared distance between a π^\pm track and the closest neutral shower.	46
5.5	Squared distance between a neutral shower and the closest charged track.	47
5.6	Comparison of the fake shower structure with the shower originating from a photon from $K^0 \rightarrow \pi^0\pi^0$ decay.	47
5.7	The difference of the measured and the expected shower direction.	48
5.8	Number of neutral showers per event in $K^0 \rightarrow \pi^+\pi^-$ data as a function of the cut-off distance around the charged kaon track.	49
5.9	Comparison of the squared distance between a charged track and the closest fake shower for data and MC.	50
5.10	Comparison of the fake shower structure between data and MC.	51
6.1	A $K^0 \rightarrow \pi^0\pi^0$ event.	54
6.2	Probability distribution of the 1C-fit.	56
6.3	Cosine of the reconstructed e^+e^- opening angle.	56
6.4	e^+e^- invariant mass for the simulated events with a π^0 Dalitz decay and photon conversion.	57
6.5	Neutral shower multiplicity in the data events.	58
6.6	Reconstruction of the e^+e^- vertex. It is found as a point laying on the line connecting the centers of two circles formed by the track projections to the $X - Y$ plane. The distance between the vertex and the center of each circle is proportional to the circle radius.	59
6.7	The difference between the reconstructed and true e^+e^- vertex for the simulated events.	60
6.8	K^0 decay vertex reconstruction as an intersection point of K^0 and γ^* flight paths.	60
6.9	The pull-plots showing the quality of the estimated lifetime error.	62
6.10	Lifetime resolution distribution ($\tau_{measured} - \tau_{true}$) for simulated events with Dalitz decays.	63
6.11	Lifetime resolution distribution ($\tau_{measured} - \tau_{true}$) for simulated events with photon conversion.	64
6.12	Scatter plot of the e^+e^- vertices in the $R - Z$ plane and its projection on R . We see at radius of 7 cm a signal originating from target wall. The target is followed by two walls of proportional chambers. Four first walls of the drift chambers also can be seen.	65
6.13	Distance between the reconstructed K^0 decay vertex and the e^+e^- vertex.	66
6.14	Lifetime distribution of the selected events (all the cuts described up to now are applied).	66
6.15	Example of a fit to the measured dE/dx spectrum of the kaon candidates with momentum between 680 and 720 MeV/c.	67

6.16	Reconstructed neutral kaon lifetime distribution with signal and background contaminations. The final analysis cuts are applied.	68
6.17	The measured distribution of the squared $K^\pm\pi^\mp$ missing mass.	70
6.18	$Z_K - Z_\gamma$ distribution before and after applying the cut reducing the fake showers.	70
6.19	The distance between a fake photon and a charged particle s compared with the respective distribution obtained for a photon originating from K^0 decay.	71
6.20	$K^0 \rightarrow \pi^+\pi^-$ background.	73
6.21	$\pi^+\pi^-$ invariant mass of "secondary particles". A peak at the K^0 mass is a sign of the golden $K^0 \rightarrow \pi^+\pi^-$ background.	73
6.22	Energy distribution of the reconstructed converted photon in the K^0 rest frame for the simulated K^0 decays into two and three neutral pions and for the data.	74
6.23	The 7C-fit probability distribution for the simulated $K^0 \rightarrow \pi^0\pi^0$ events and $K^0 \rightarrow \pi^0\pi^0\pi^0$	75
6.24	Lifetime distributions obtained from the Monte Carlo simulation for the golden background channels.	76
6.25	Lifetime dependent acceptance for Dalitz decays and photon conversion.	78
6.26	Fit to the reconstructed neutral kaon lifetime distribution.	79
6.27	Reconstructed \overline{K}^0 and K^0 decay rates.	80
6.28	The measured decay asymmetry $A_{oo}(\tau)$	80
6.29	Normalization α as a function of the K^0 momentum and the dip angle.	81
6.30	Asymmetry $A_{oo}(\tau)$ expected with an ideal lifetime resolution, with the resolution achieved in this analysis and after adding the backgrounds.	82
6.31	The reduced K^0 and \overline{K}^0 decay asymmetry emphasizes the CP violation effect at short lifetimes.	84
6.32	The lifetime distribution for the selected $p\bar{p} \rightarrow K^+K^-n\pi^0$, $n \geq 1$ events compared with the Monte Carlo simulation.	85
7.1	A $K^0 \rightarrow \pi^0\pi^0\pi^0 \rightarrow 6\gamma$ event. The neutral kaon decays into $3\pi^0$ which give six photons detected as neutral showers in the calorimeter.	89
7.2	Distribution of the photon conversion points in the $\varphi - Z$ plane.	91
7.3	$K^\pm\pi^\mp$ missing mass distribution after applying a 10% probability cut on $\chi^2_{secondary}$ and after a cut on χ^2_{7C}	93
7.4	A photon conversion in the Čerenkov counter resulting in two neutral showers close to each other.	94
7.5	The minimal invariant mass of all two photon pairs.	94
7.6	Invariant mass of all six photons for the simulated signal and background events compared with the respective distribution for the data events.	95
7.7	Suppression of the events with fake showers showed using the distribution of K^0 lifetime reconstructed using 6C-fit.	96
7.8	Lifetime distribution for selected data events.	97

7.9	The distribution of the squared $K^\pm\pi^\mp$ missing mass for the reconstructed data events. The missing mass is shown in the bins of the reconstructed neutral kaon lifetime.	98
7.10	Lifetime distributions for the background channels and for the signal events obtained from the Monte Carlo simulation and dE/dx fits (pionic background).	99
7.11	Reconstructed lifetime distribution together with signal and background contaminations obtained from the lifetime fit.	100
7.12	Fits to the $K^\pm\pi^\mp$ missing mass spectra in three lifetime intervals. . . .	102
7.13	Lifetime distributions for signal and background obtained from the missing mass fits.	103
7.14	Measured decay rates of initially pure K^o and \overline{K}^o states.	104
7.15	Measured lifetime dependent asymmetry $A_{meas}^{ooo}(t)$ together with the fitted function with free $\mathcal{R}e(\eta_{ooo})$ and $\mathcal{I}m(\eta_{ooo})$	105
7.16	Distribution of the lifetime resolution ($\tau_{reconstructed} - \tau_{true}$) and the lifetime dependent acceptance.	106
7.17	Parametrization of the background lifetime distributions.	106
A.1	Dalitz decay $\pi^o \rightarrow e^+e^-\gamma$ in the QED lowest order.	112
A.2	The differential decay rates $d\Gamma/dx$ and $d\Gamma/dy$ of the Dalitz decays $\pi^o \rightarrow e^+e^-\gamma$. The small plot shows $d\Gamma/dx$ in the linear scale.	114
A.3	The theoretical electron-positron opening angle distribution in the lab-system for Dalitz decays of neutral pions, which are produced in the reaction $p\overline{p} \rightarrow K^\mp\pi^\pm K^o(\overline{K}^o)$, $K^o \rightarrow \pi^o\pi^o$ at CPLEAR.	114
B.1	The differential cross section for photon conversion $d\sigma/dw_+$	116
D.1	Representation of the parameters describing a helix. x_c and y_c denote the coordinates of the center of the circle.	120

List of Tables

3.1	Basic parameters describing the neutral kaon system [19].	9
4.1	Properties of materials used to construct detectors.	39
4.2	Material distribution in target and proportional chambers.	40
4.3	Material distribution in drift chambers, streamer tubes, PIDs and calorimeter.	41
5.1	Number of fake showers per event in golden $K^0 \rightarrow \pi^+\pi^-$ events in real and simulated data as a function of the applied cut.	51
6.1	Summary of cuts applied in the $K^0 \rightarrow \pi^0\pi^0$ analysis. Number of simulated events after prefiltering and general quality cuts is normalized to 1000.	77
6.2	Background contaminations.	79
6.3	Systematic errors.	87
7.1	Signal and background contributions in the $[0 - 20] \tau_S$ lifetime interval obtained from lifetime and $K^\pm\pi^\mp$ missing mass fits. In the third columns the results of the combined lifetime and missing mass fit are shown. The average of results of these three fits is given in the last column.	100
7.2	Parametrization of the lifetime dependence of the background channels.	104
7.3	Systematic errors on $\mathcal{R}e(\eta_{ooo})$ and $\mathcal{I}m(\eta_{ooo})$	108

Curriculum Vitae

Born 11th Aug. 1966 in Krakow, Poland

School education:

- 1973-1981 primary school in Krakow
- 1981-1985 Nowodworski High School in Krakow

University education:

- 1985-1990 Studies of physics at the Jagellonian University in Krakow
- 1990 M.Sc. degree at the Jagellonian University in Krakow.
Thesis: "Drift Chamber Telescope for Detection of Trajectories of Cosmic Ray Particles" Advisor: Dr. G. Polok, Institute of Nuclear Physics, Krakow.
- 1990 Teaching Assistant at the University of Mining and Metallurgy in Krakow
- 1990 Summer Student at DESY, Hamburg - working in the Crystal Ball Collaboration (spokesman Prof. J.K. Bienlein).
- 1991 Research Assistant at the Institute of Nuclear Physics, Krakow
- 1992-1996 Ph.D. student at the Swiss Federal Institute of Technology (ETH) Zurich involved in the CPLEAR experiment at CERN.